



Calhoun: The NPS Institutional Archive
DSpace Repository

Theses and Dissertations

1. Thesis and Dissertation Collection, all items

1949

Experimental investigation of a stationary cascade of aerodynamic profiles

Sawyer, William Thomas

Zurich: Swiss Federal Institute of Technology

<http://hdl.handle.net/10945/31649>

Downloaded from NPS Archive: Calhoun



Calhoun is the Naval Postgraduate School's public access digital repository for research materials and institutional publications created by the NPS community. Calhoun is named for Professor of Mathematics Guy K. Calhoun, NPS's first appointed -- and published -- scholarly author.

Dudley Knox Library / Naval Postgraduate School
411 Dyer Road / 1 University Circle
Monterey, California USA 93943

<http://www.nps.edu/library>

Experimental Investigation of a Stationary Cascade of Aerodynamic Profiles

Library
U. S. Naval ~~Postgraduate~~ School
Annapolis, Md.

AT THE

SWISS FEDERAL INSTITUTE OF
TECHNOLOGY, ZUERICH

TOWARD ATTAINMENT OF THE DEGREE OF
DOCTOR OF TECHNICAL SCIENCE

APPROVED DISSERTATION

SUBMITTED BY

James
William T. Sawyer

of Nantucket, Massachusetts, U.S.A.

thos
St. Ch. vs N
P.G. student.

Referent: Prof. Dr. J. Ackeret

Co-Referent: Prof. H. Quiby



ZÜRICH 1949

Dissertationsdruckerei Leemann AG.

End 14

Experimental Investigation of a Stationary Cascade of Aerodynamic Profiles

AT THE

**SWISS FEDERAL INSTITUTE OF
TECHNOLOGY, ZUERICH**

TOWARD ATTAINMENT OF THE DEGREE OF
DOCTOR OF TECHNICAL SCIENCE

APPROVED DISSERTATION

SUBMITTED BY

William T. Sawyer

of Nantucket, Massachusetts, U.S. A.

Referent: Prof. Dr. J. Ackeret

Co-Referent: Prof. H. Quiby



ZÜRICH 1949

Dissertationsdruckerei Leemann AG.

Erscheint als Nr. 17 der Mitteilungen aus dem Institut für Aerodynamik
an der Eidgenössischen Technischen Hochschule in Zürich
Herausgegeben von Prof. Dr. J. Ackeret

Tu 1811

1811

TO MY WIFE,
MARY GROVE SAWYER

12382

Index

	Page
I. Introduction	7
II. Preliminary Computations	8
A. Determination of the Cascade Blade Profile	8
1. General Problems and Available Theories	8
2. The Continuum Cascade Theory and its Application	9
B. Cascade Blade Static Pressure Distribution From Continuum Cascade Theory	25
C. Streamlines Directly Ahead of and Behind a Cascade Blade	27
III. Test Equipment	28
A. Wind Tunnel (up to Test Section)	28
B. Test Section of Tunnel	30
C. Cascade Force-Measuring Balance	32
D. Instrumentation	34
IV. Preliminary Experimental Work	35
A. Test of the Amsler Principle for Application to the Construction of a Balance	35
B. Static Calibration of Balance	37
C. Determination of Turbulence for Free Tunnel Flow and Behind Wire Screens	38
D. Flow Uniformity in the Tunnel Test Section	41
E. Force on Sealing Plate and Blade Base Exterior to Tunnel	47
V. Experimental Data	48
A. General Plan	48
B. Two-dimensional Phenomena	49
1. Static Pressure Distribution on Blade at Mid-height	49
2. Change in Reference Cascade Pressure Drop and Turning Angle with Reynolds Number and Turbulence	49
3. Total Pressure Wake Traverses at Blade Mid-height	50
4. Flow at Blade Surface	50
C. Three-dimensional Phenomena	50
1. Wall Static Pressure Field	50
2. Balance Measurements	50
3. Momentum Traverses Over Blade Height	52
VI. Discussion of Data: Comparison with Theory	53
A. Two-Dimensional	53
1. Static Pressure Distribution About Blade at Mid-height	53
2. Blade Losses from Wake Traverses	56
3. Flow at Blade Surface	61
4. Relative Variation of Cascade Pressure Drop and Turning Angle	64
B. Three-Dimensional	66
1. Distribution of Losses Over Blade Height; Tip Clearance Effect	66
2. Blade Efficiency from Force Measurements	69
a) Definition and Derivation of Blade Efficiency Using Blade Forces	69
b) Evaluation of the Blade Efficiency from Current Tests	72
VII. Summary and Conclusions	76
A. Cascade Testing in General	76
B. Turbulence and Reynolds Number Effects Upon Blade Performance	76
C. Continuum Theory of Cascades	76

Foreword

The experimental investigation of cascade phenomena presented herein was carried out at the Institute for Aerodynamics, Swiss Federal Institute of Technology, Zürich, under the guidance of Prof. Dr. J. Ackeret. The work owes much to the keen insight of Prof. Ackeret, and I wish to acknowledge here my appreciation of his suggestions and farsighted advice. To Mr. Bernard Chaix I am indebted for his most generous assistance and encouragement. Not only for their excellent workmanship but also for their willingness and cooperation, my thanks are due to the Institute technicians. Finally, and in full measure, I wish to express my gratitude to Vice Admiral E. L. Cochrane, USN, whose broad perspective made possible my undertaking of this work.

List of Symbols

<i>A</i>	Area; m^2
<i>C</i>	Absolute Velocity; m/sec
<i>F</i>	Component of Force; kg
<i>H</i>	Perpendicular Distance Between Geometrical Inlet and Outlet Planes of Cascade; m
<i>L</i>	Scale of Turbulence (See Chap. IV, Sect. C); mm
<i>M</i>	Mass Rate of Flow; kg (mass)/sec
<i>N</i>	Subscript: In Direction Normal to Cascade Axis
<i>P</i>	Pressure; Without Subscript, Static Pressure; kg/m^2
<i>Q</i>	Volume Rate of Flow; m^3/sec
<i>R</i>	Resultant or Total Force; kg
<i>T</i>	Subscript: In Direction Parallel to Cascade Axis
<i>U</i>	Mean Velocity of Fluid Flow Outside Boundary Layer: Velocity of Cascade in Direction of Its Axis; m/sec
<i>V</i>	General Expression for Velocity; m/sec
<i>W</i>	Relative Velocity of Fluid Flow; m/sec
<i>Z</i>	Axial Length of Cascade Blade: Tunnel Height; m
<i>a</i>	Area per unit length; m^2/m
<i>b</i>	Subscript: Blade
<i>c_a</i>	Lift Coefficient; dimensionless
<i>d</i>	Blade Thickness; m
<i>g</i>	Total Pressure (also subscript) = $P_{static} + \rho V^2/2$; kg/m^2
<i>l</i>	Blade Chord; m
<i>q</i>	Dynamic Pressure = $\rho V^2/2$; kg/m^2
<i>s</i>	Subscript: Static
<i>t</i>	Blade Spacing; m
<i>u</i>	Velocity in x-Direction; Fluctuation Velocity Relative to Mean Velocity; m/sec
<i>v</i>	Velocity in y-Direction; m/sec
<i>x, y, z</i>	Coordinate Axes, Defined Where Used
0	Subscript: Mean Value; First-approximation Value
1	Subscript: Upstream Reference Plane
2	Subscript: Downstream Reference Plane
∞	Subscript: Indicates Mean of Two Vectors
Γ	Total Circulation; m^2/sec
β	Angle of Flow Relative to Axis of Approach Section of Tunnel
γ	Local Circulation Strength; 1/sec
δ	Boundary Layer Thickness; m
η	Dimensionless Coordinate; $\eta_H = y/H$; $\eta_t = y/t$; $\eta_l = y/l$
θ	Angle Between <i>R</i> and Cascade Axis
ν	Kinematic Viscosity = $\frac{\eta}{\rho} m^2/sec$
ξ	Dimensionless Coordinate: $\xi_H = x/H$; $\xi_t = x/t$; $\xi_l = x/l$
ρ	Density; $kg\text{-}sec^2/m^4$
σ	Local Source Strength; 1/sec
—	Superscript: Mean Value Outside Boundary Layers

I. Introduction

The ready, although ultimately limited, applicability of the results of two-dimensional cascade testing to the practical three-dimensional problems of rotating fluid-flow machines such as turbines and compressors (both axial-, and in certain cases, radial-flow), propellers, fans, etc., has led to the development of powerful and comprehensive theories based upon an "ideal" fluid, and to the presentation of considerable data resulting from experimental investigations of the flow of a real fluid through both straight and circular cascades. The objective of the present experimental investigation is not primarily to extend further the available data regarding the effects of changes in cascade geometry (i. e., profile form, angle of attack, stagger, spacing, aspect ratio), but rather to seek a more exact basis for evaluation of the performance of a *single* cascade arrangement and a fuller appreciation of the effects of certain properties of the fluid associated therewith.

Both for greater facility and for greater exactitude in the determination of general cascade performance, the evaluation of this performance by means of direct balance measurements of the dynamic forces exerted by fluid upon the blades is undertaken. A special balance suitable for cascade work is developed. Overall blade efficiency is rationally defined in terms of accurate force measurements. By means of exact and extensive measurements of all parts of the fluid which are affected by the cascade, confirmation of the validity of the force measurements, as well as information regarding the practical aspects of accurate cascade testing in general, is sought.

The investigation embraces the study of Reynolds number and turbulence effects upon typical turbine blading, and includes an experimental verification of the *Ackeret* continuum-cascade method [1]¹⁾ of blade design. The practical importance of Reynolds number in relation to turbo-machinery performance is apparent under two general conditions: (1) Part-load (low-speed) operation of certain gas turbine plants; and (2) Full-load operation of these plants under conditions of large kinematic viscosities (e. g., aircraft at high altitudes). Systematic variations of both the scale and intensity of turbulence of the incident flow are undertaken.

All tests are carried out with air flowing at very low velocities relative to the speed of sound. Under these conditions, and with the very small pressure differentials involved, the fluid is treated as incompressible. Mach numbers are one-tenth or less.

¹⁾ Figures in brackets [] refer to references listed on pages 77—78.

II. Preliminary Computations

A. Determination of the Cascade Blade Profile

1. General Problems and Available Theories

The application of results gained from usual stationary cascade testing to the practical three-dimensional case of flow through a stage of a turbo-machine is based upon the assumption that flow in the latter case takes place along coaxial cylindrical surfaces. The development of a cylindrical section taken through a turbo-machine stage produces the picture of a two-dimensional straight-line cascade.

The theories available for the solution of the two-dimensional cascade problem may be most generally classified as follows:

I. Those theories which yield the performance characteristics of a *pre-determined* physical cascade arrangement.

II. Those which *define* the cascade geometry required to produce certain cascade characteristics.

Since the actual problem of the design engineer is the choice of a blade (cascade) arrangement which will efficiently produce a predetermined change in direction of the working fluid (vector velocity diagram), an interpolation on his part of the results of theories under I., above, will in general be required, while theories under II. will yield the desired result directly.

Each of the foregoing classifications may be further subdivided as follows:

A. Those methods in which the streamlines through the cascade are all considered to be parallel to one another (the stream filament theories of *Euler* and *Lorenz* [2], applicable only to very closely spaced, very thin blades).

B. Those methods in which variations between adjacent streamlines associated with a practical cascade are recognized, and whose success is dependent, directly or indirectly, upon the accurate determination of the configuration of the streamlines. This group makes effective use of the powerful resources of potential theory.

It is perhaps well to observe at this point that an alternative to all the foregoing theoretical methods is the experimental testing of systematically varied blade shapes and arrangements in cascade which, although time-consuming and costly, yields results which are applicable to construction of practical machines handling actual fluids rather than the "ideal" frictionless fluid assumed in potential flow computations. (See, for example, ref. [3]).

Under B. above may be classified all of the following:

1. Those methods which assume all or part of the actual cascade blades replaced by either "point" or continuously-distributed aerodynamic singularities (i. e., bound vortices, sources, sinks). (Under I. — *Betz* [4], *Schil-hansl* [5], and others; under II. — *Ackeret* [1]).

2. Those methods which assume the blades wholly or partially replaced by simple geometrical shapes considered to produce the same circulation as the actual blades. (Under I. — *Weinel* [6], *Weinig* [7], and others).

3. Those methods employing the device of conformal transformation of the entire cascade into a simple geometrical area containing singularities, the resultant field being solvable by potential theory. (Under 1. — *König* [8], *Busemann* [9], *Howell* [10], *Traupel* [11], *Vazsonyi* [12], *Legendre* [13], and others).

The *Ackeret* continuum cascade theory, which is the only theory presented for determination of a blade form to satisfy required cascade characteristics²⁾ (foregoing classification II) was used in defining the cascade tested in this investigation. It was desired to obtain experimental confirmation of a two-dimensional application of this theory, which has recently been extended in the manner indicated by *Ackeret* to the three-dimensional case of a complete circular cascade as well [19]. Since it forms the basis for the physical definition of the cascade tested, the salient features of the theory are outlined in the following section.

2. The Continuum Cascade Theory and Its Application

The theory may be most readily understood by tracing the steps in the solution of an hypothetical two-dimensional problem. This will require the mention of some incidental elementary theory and practical considerations, but should not obscure the salient points of the theory itself. For proofs, which are omitted, the reader is referred to the original paper of Prof. *Ackeret* [1].

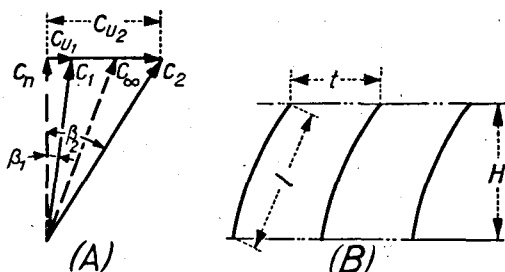


Figure 1: Basic Data Required for Continuum Cascade Theory
(A) Velocity Diagram. (B) Cascade Dimensions

Assume that it is desired to construct a cascade which, when entered by a stream of fluid with velocity and direction given by C_1 , will produce an outlet velocity vector C_2 , Figure 1 (A). Let t be the blade spacing, Z the blade height (perpendicular to plane of paper), H the perpendicular distance between inlet and outlet planes of the cascade, c_a the blade lift coefficient in cascade, Γ the total circulation for each blade, and l the blade chord, Figure 1 (B). We then may write the following general relationships (see, for example, references [20] and [21]):

²⁾ *Weinig* [14], *Schmieden* [15], and *Betz* [16] have obtained solutions of limited applicability for the case of a single airfoil (as distinguished from a series of airfoils in cascade). Also for the single airfoil, *Peebles* [17] has recently presented a generally applicable solution, based upon the work of *Mangler* [18].

$$C_{u2} - C_{u1} = \frac{\Gamma}{t} \quad (1)$$

$$c_a \cdot (\varrho C_\infty^2 / 2) \cdot l = \varrho \cdot C_\infty \cdot \Gamma;$$

$$\Gamma = \frac{c_a \cdot C_\infty \cdot l}{2};$$

$$C_{u2} - C_{u1} = \frac{c_a \cdot C_\infty \cdot l}{2t} \quad (2)$$

$$\text{Aspect ratio} = \frac{Z}{l} \quad (3)$$

$$Re_{blade} \equiv \frac{l \cdot C_\infty}{\nu} \quad (4)$$

$$\frac{l}{H} \approx \frac{C_\infty}{C_n} \quad (5)$$

The choice of the value for c_a involves considerations of blade efficiency (minimum glide angle) and avoidance of cavitation or separation. For a full discussion of the factors involved, the reader is referred to references [20] and [21]. With c_a chosen, and C_∞ fixed by the given velocity triangle, equation (2) establishes the ratio (l/t). Since it is theoretically immaterial whether we choose to have relatively many, lightly-loaded blades or relatively few, highly-loaded ones, we refer to equations (3) and (4) to establish a value of l . The chord chosen must represent a compromise between the conflicting requirements of large aspect ratio (*small* l , equation 3) and high Reynolds number (*large* l , equation 4). Experimental data available assists us in making this choice. The spacing t then follows from (2), Γ from (1), and the cascade dimension H from (5). With these quantities, we are ready to proceed with the application of the theory.

We first utilize the *Eulerian* theory to determine the shape of a first-approximation blade camber line, which is to be that of a flow streamline. Referring to Figure 2(e), we consider the circulation γ_0 (dimension sec^{-1}), to be constant in the x -direction (infinite number of blades), while in the y -direction we cause it to vary continuously in prescribed manner. The *scale* of the curve $\gamma_0 = f(y)$ is given by the requirement,

$$\Gamma = t \cdot \int_0^H \gamma_0 \cdot dy.$$

If, for example, we take an *elliptical*³⁾ circulation distribution in the y -direction, as was done in the determination of the blade profile for the present investigation,

$$\gamma_0 = \frac{8 \Gamma}{\pi \cdot H \cdot t} \sqrt{\frac{y}{H} - \left(\frac{y}{H}\right)^2}.$$

³⁾ Not to be confused with the *spanwise* elliptical distribution of circulation for an aircraft wing.

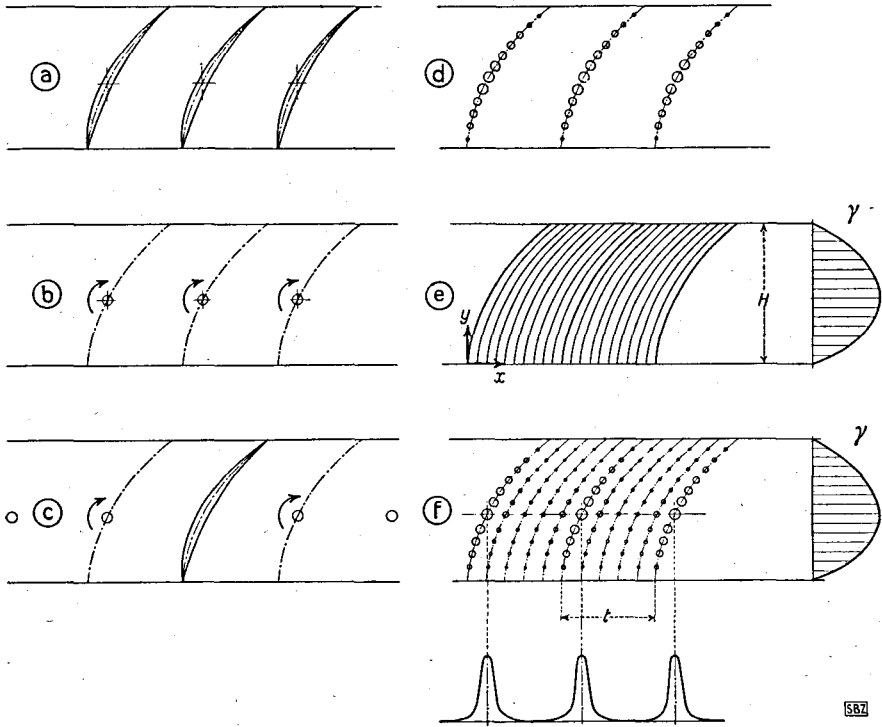


Figure 2: *Some Steps in the Development of Cascade Theory*

a) Accelerating cascade of closely-spaced blades. b) Single bound vortices substituted for blades. c) Single bound vortices substituted for all but one blade. d) Linear distribution of vortices substituted for blades. e) Infinite number of blades; continuously distributed circulation as function of y only. f) Periodic continuous distribution of circulation

Considering the effect of circulation only, the velocity at any point having the ordinate y is obtained by adding to the approach velocity C_1 [Figure 1 (A)] the component u_{γ_0} [Figure 7 (A)] given, according to *Stokes' Theorem*, by the equation,

$$u_{\gamma_0} = \int_0^y \gamma_0 \cdot dy. \quad (6)$$

The blades of a real cascade are of finite thickness, and the fluid velocities are affected by that thickness. We take account of this effect by a continuous distribution of sources and sinks in the cascade area in a manner analogous to the circulation distribution. The source-sink distribution σ_0 , (dimension sec^{-1}), is constant in the direction of x , but varies along y in a manner also to be prescribed (see, for example, Figure 3) ⁴⁾. If a rounded

⁴⁾ It is to be noted from Figure 3 that the curve of $\left(\int_0^y \sigma_0 \cdot dy\right)$ is roughly proportional to the curve of final blade thickness distribution, a fact which may serve as a guide in choosing the curve $\sigma_0 = f(y)$.

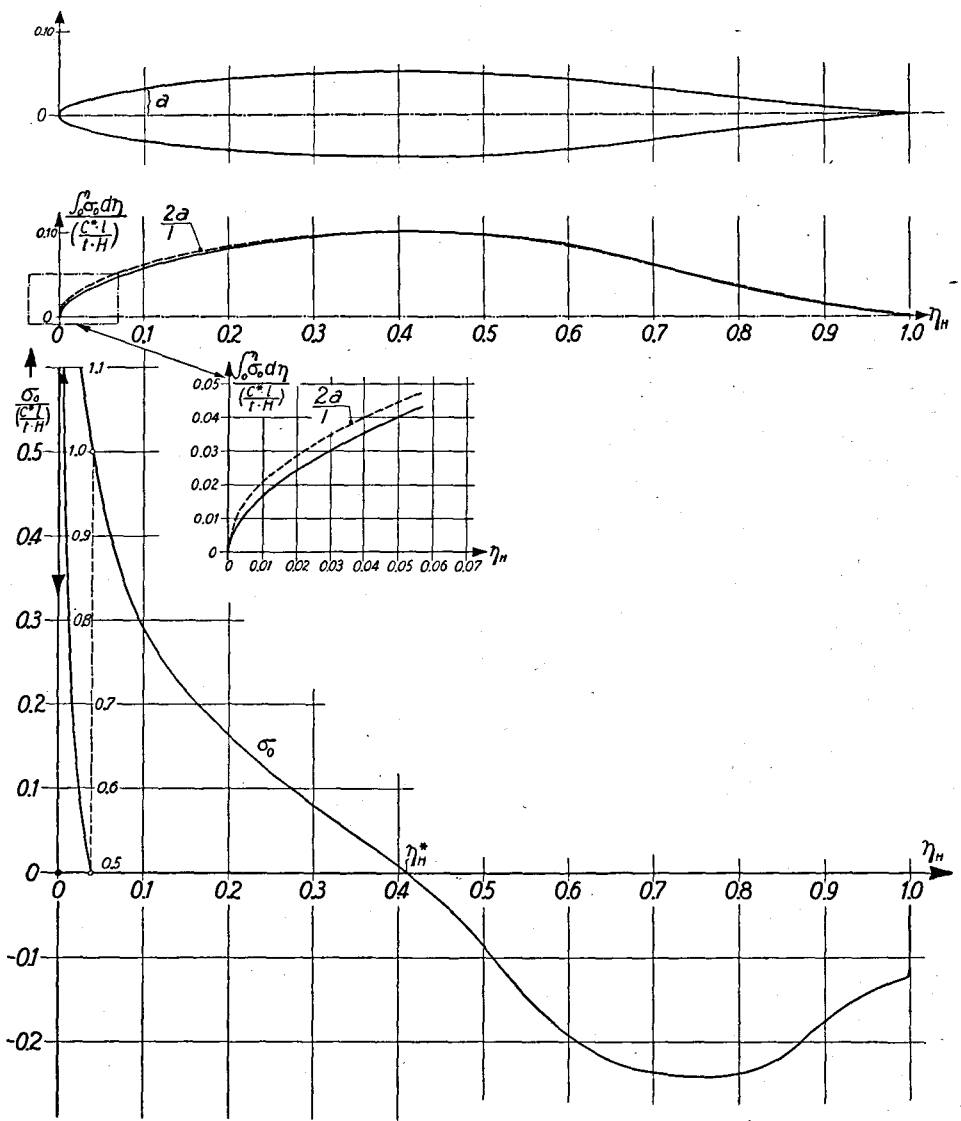


Figure 3: Assumed Source Distribution

Bottom — σ_0 as Function of η_H ; ($\eta_H = \frac{y}{H}$; Fig. 1). Center — $\int_0^{\eta_H} \sigma_0 \cdot d\eta_H$ as Function of η_H .
 Top — Resultant Blade Thickness Distribution

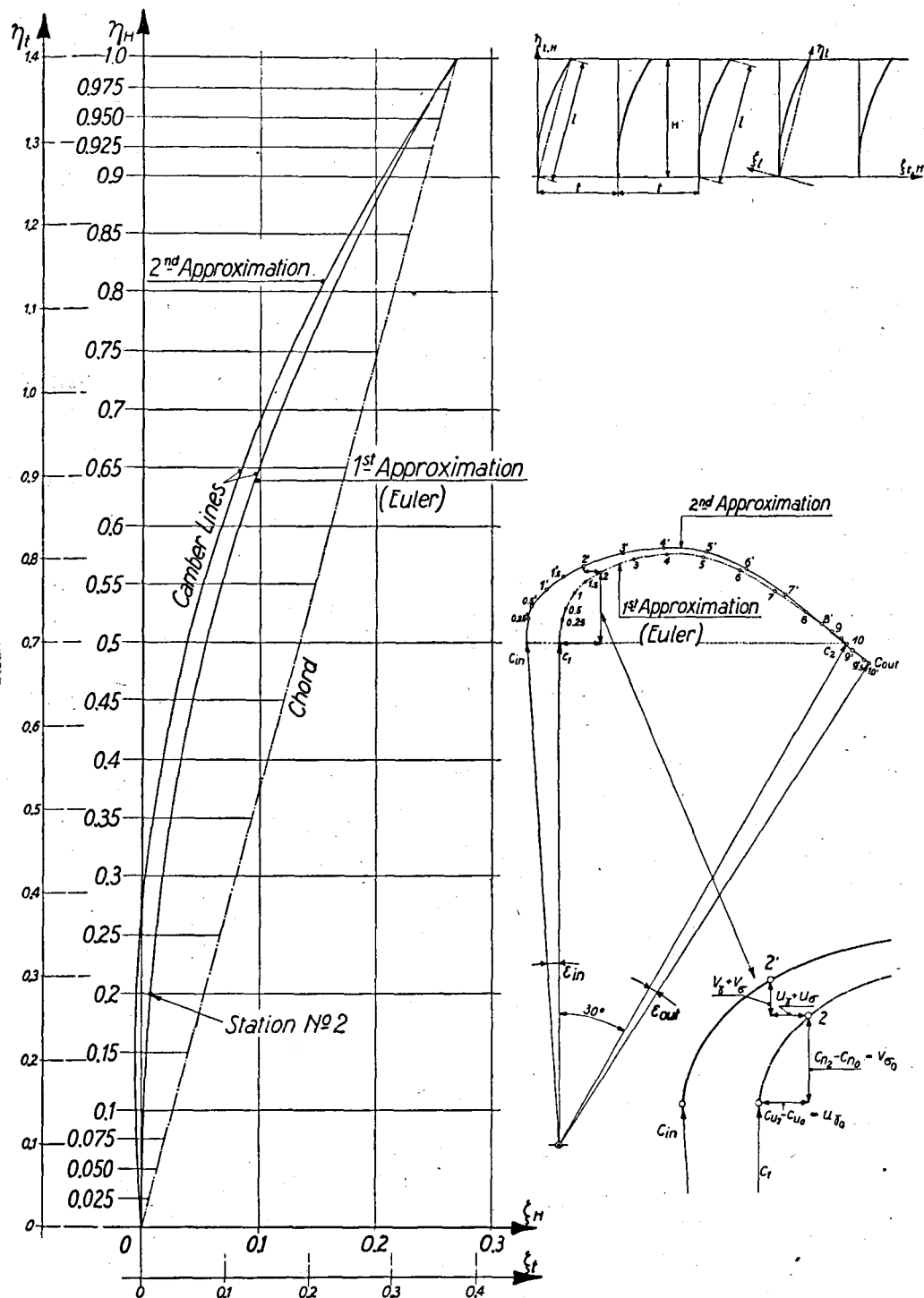


Figure 4: Determination of Velocity Hodographs by Continuum Theory, and Resultant Blade Camber Lines

Velocity vectors C_1 and C_2 as given by the specific velocity triangle assumed for this investigation. Angular exaggeration at inlet (ϵ_{in}) = $3^\circ 44'$; at outlet (ϵ_{out}) = $2^\circ 41'$

blade nose is desired, a high concentration of sources near $y = 0$ will be required (Figure 3). As in all cases where sources are employed to represent a cylindrical body, a further requirement is,

$$\int_0^H \sigma_0 \cdot dy = 0.$$

It may also be seen that the blade, as finally established, will have its maximum thickness, d^* , at a point y^* where the curve of $\sigma_0 = f(y)$ passes from positive to negative (Figure 3). For practical reasons, the designer will require that the blade as finally established shall at least approximate a pre-determined maximum thickness. Knowledge of this maximum thickness allows us to establish the *scale* of the $\sigma_0 = f(y)$ curve, since, as we shall see later,

$$d_{(y)} = \frac{t \int_0^y \sigma_0 \cdot dy}{C_{(y)}}; \quad \text{whence} \quad d^* = \frac{t \int_0^{y^*} \sigma_0 \cdot dy}{C^*}. \quad (7)$$

(C^* = fluid velocity corresponding to ordinate y^* .)

Considering the source-sink distribution only, the velocity at any point having the ordinate y is obtained by adding to the approach velocity C_1 [Figure 1 (A)] the component v_{σ_0} [Figure 8 (A)] given by the equation,

$$v_{\sigma_0} = t \int_0^y \sigma_0 \cdot dy. \quad (8)$$

In order to fix the scale for $\sigma_0 = f(y)$, C^* may be approximated in equation (7) by adding to C_1 the component $u_{\gamma_0(y=y^*)}$ from equation (6). Then, with the $\sigma_0 = f(y)$ scale so estimated, $v_{\sigma_0(y=y^*)}$ may be determined from (8), and a nearly exact value for C_0^* obtained. The change in scale due to the correction in C_0^* will yield a new $v_{\sigma_0(y=y^*)}$ and thus a still more exact C_0^* . The process converges so rapidly that two or three scale determinations suffice, and may be further shortened by multiplying the first value of $(\vec{C}_1 + \vec{u}_{\gamma_0})$ by the factor $(1 + \frac{d^*}{l})$ to allow for v_{σ_0} .

We now divide the cascade dimension H into a convenient number of parts and compute for each "station" the components u_{γ_0} and v_{σ_0} . The resultant velocities are then conveniently shown by a hodograph as in Figure 4. Using the tangent method, the first approximation streamline (camber line) is plotted for the cascade.

So far, we have considered circulation and source strength to be constant in the x -direction. Our second (and final) approximation consists of producing a strong *concentration* of both circulation and source strength periodic with the blade spacing in the x -direction, with the maxima of the $\gamma = f(x)$ and $\sigma = f(x)$ curves coinciding with the first-approximation camber lines already established. See Figures 2, 5 and 6. This step is the essence of the continuum theory, and the manner of its accomplishment will be discussed in some detail.

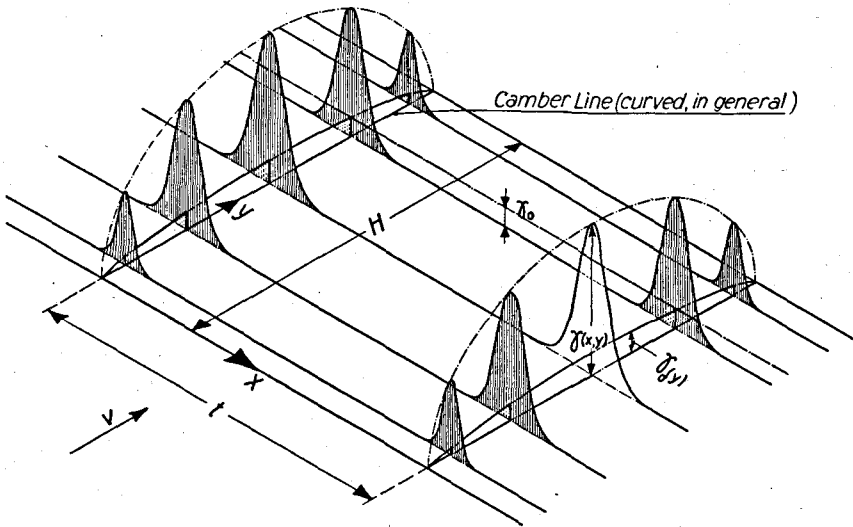


Figure 5: Schematic Diagram of Continuous Distribution of Circulation, γ , in Directions of Both x and y
Camber Line Shown Straight for Clarity

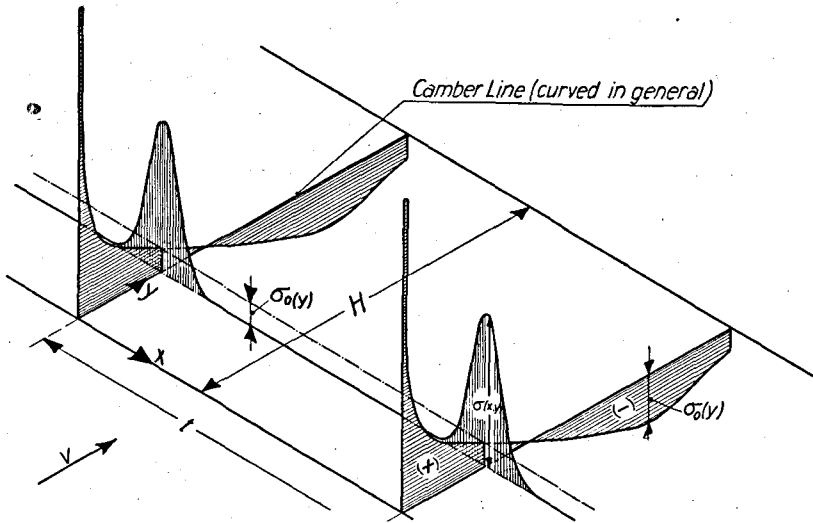


Figure 6: Schematic Diagram of Continuous Distribution of Sources and Sinks, σ , in Directions of Both x and y
Camber Line Shown Straight for Clarity

One of the simplest types of continuous periodic distributions is a cosine curve: $\gamma = \gamma_m \cdot \cos(2\pi x/t)$; or, $\sigma = \sigma_m \cdot \cos(2\pi x/t)$. Figures 7 and 8 show the flow fields of such distributions in a thin layer of infinite length. The disturbance velocities in the upper halves of the figures are given by the equations:

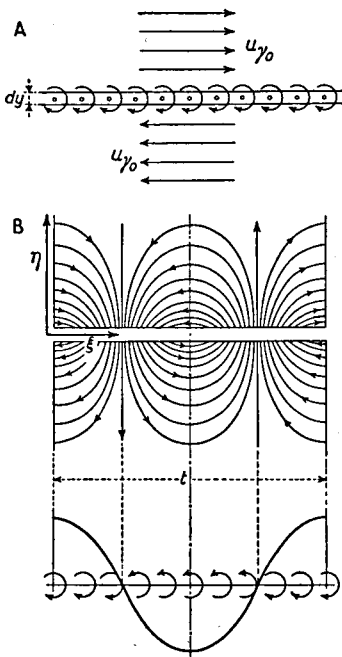


Figure 7: *Field of Vortex Sheet*

- A) Constant circulation distribution.
B) Periodically-varying circulation distribution

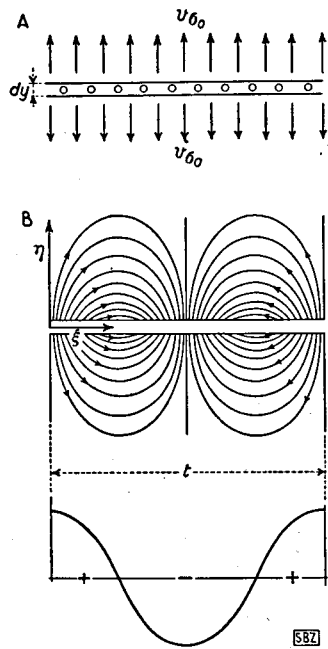


Figure 8: *Field of a Source Sheet*

- A) Constant source distribution
B) Periodically-varying source distribution

For the vortices (Figure 7):

$$du_y = \frac{\gamma_m}{2} \cdot \cos(2\pi x/t) \cdot e^{-2\pi y/t} \cdot dy$$

$$dv_y = -\frac{\gamma_m}{2} \cdot \sin(2\pi x/t) \cdot e^{-2\pi y/t} \cdot dy$$

In the layer itself, there is a discontinuity in the horizontal velocity component, while the vertical component is continuous.

For the sources (Figure 8):

$$du_\sigma = \frac{\sigma_m}{2} \cdot \sin(2\pi x/t) \cdot e^{-2\pi y/t} \cdot dy$$

$$dv_\sigma = \frac{\sigma_m}{2} \cdot \cos(2\pi x/t) \cdot e^{-2\pi y/t} \cdot dy$$

In the layer itself, there is a discontinuity in the vertical velocity component, while the horizontal component is continuous.

Similarly, for the *lower* halves of the figures ($y = \text{negative}$):

For the vortices:

$$du_y = -\frac{\gamma_m}{2} \cdot \cos(2\pi x/t) \cdot e^{2\pi y/t} \cdot dy$$

$$dv_y = -\frac{\gamma_m}{2} \cdot \sin(2\pi x/t) \cdot e^{2\pi y/t} \cdot dy$$

For the sources:

$$du_\sigma = \frac{\sigma_m}{2} \cdot \sin(2\pi x/t) \cdot e^{2\pi y/t} \cdot dy$$

$$dv_\sigma = -\frac{\sigma_m}{2} \cdot \cos(2\pi x/t) \cdot e^{2\pi y/t} \cdot dy$$

These simple cosine-curve distributions are not in themselves adequate for our purpose. However, we may choose a suitable curve, resolve that curve into a *Fourier* cosine series, and use the foregoing to determine the resultant velocity field.

Departing from the trapezoidal and rectangular distributions of the original *Ackeret* paper, a convenient distribution curve is the bell-shaped one (see Figure 9) whose equation is:

$$\gamma = \gamma_{max} \cdot e^{-\xi_t^2/\alpha^2}; \quad \text{or} \quad \sigma = \sigma_{max} \cdot e^{-\xi_t^2/\alpha^2},$$

$$\text{where: } \xi_t = \frac{x}{t}.$$

We also define, for subsequent use:

$$\eta_t = \frac{y}{t}$$

$$\gamma(x, y) = \sec^{-1} - \sigma(x, y)$$

$$\gamma_0(y) = \sec^{-1} - \sigma_0(y)$$

$$\Gamma = m^2/\sec - Q$$

$$\gamma_0 = \frac{1}{t} \int_0^t \gamma \, dx$$

$$\sigma_0 = \frac{1}{t} \int_0^t \sigma \, dx$$

$$\Gamma = \int_0^H \gamma_0 \, dy$$

$$Q = \int_0^H \sigma_0 \, dy$$

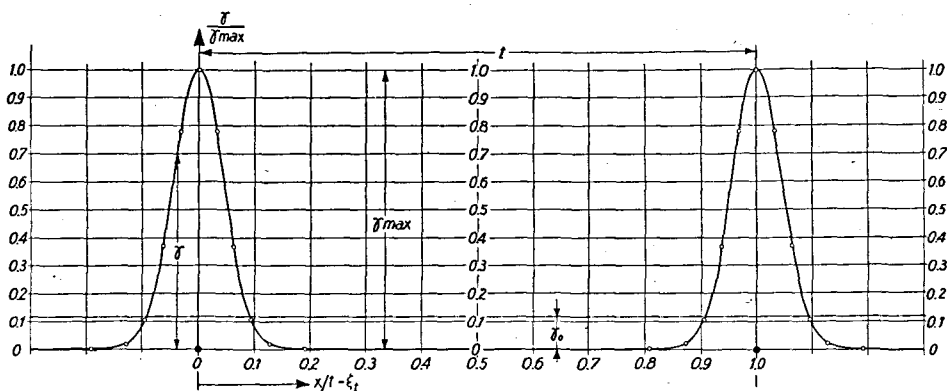


Figure 9: Periodic Distribution of Circulation in Direction of Cascade Axis

$$\gamma = \gamma_{\max} \cdot e^{-\xi_t^2 / \alpha^2}, \text{ where } \alpha = \frac{1}{5\pi}.$$

Choice of the constant α is guided by the fact that for

$$\begin{aligned} \xi_t &= \alpha; & \gamma &= \gamma_{\max} / e = 0.3680 \gamma_{\max} \\ &= 2\alpha; & \gamma &= \gamma_{\max} / e^4 = 0.0183 \gamma_{\max} \\ &= 3\alpha; & \gamma &= \gamma_{\max} / e^9 = 0.0001 \gamma_{\max}. \end{aligned}$$

We note that the total circulation under the γ -curve (Figure 9) for one blade-spacing t is given by

$$\gamma_0 \cdot t = 2 \int_0^{1/2} \gamma \cdot dx = 2t \int_0^{1/2} \gamma \cdot d\xi_t = 2t \cdot \gamma_{\max} \int_0^{1/2} e^{-\xi_t^2 / \alpha^2} \cdot d\xi_t.$$

It is seen that, due to the negligibly-small values of γ for $\xi_t > 3\alpha$, we may take "infinity" as the upper limit, and

$$\gamma_0 \cdot t = 2t \cdot \gamma_{\max} \int_0^{\infty} e^{-\xi_t^2 / \alpha^2} \cdot d\xi_t = 2t \cdot \gamma_{\max} \cdot \frac{\alpha}{2} \sqrt{\pi}. \quad [22; \text{pg. 63}]$$

$$\therefore \gamma_0 = \gamma_{\max} \cdot \alpha \sqrt{\pi}.$$

The periodic curve may be expressed by the *Fourier* series

$$\gamma = \gamma_0 + \sum_{n=1}^{\infty} a_n \cdot \cos(2\pi n \xi_t).$$

The coefficient a_n is determined by

$$\begin{aligned} a_n &= 2 \int_{-1/2}^{1/2} \gamma \cdot \cos(2\pi n \xi_t) d\xi_t = 4 \int_0^{1/2} \gamma \cdot \cos(2\pi n \xi_t) \cdot d\xi_t \\ &= 4 \gamma_{\max} \int_0^{1/2} e^{-\xi_t^2 / \alpha^2} \cdot \cos(2\pi n \xi_t) \cdot d\xi_t. \end{aligned}$$

As before, since $\gamma \cong 0$ for $\xi_t > 3\alpha$, we may write;

$$\begin{aligned} a_n &= 4 \gamma_{\max} \int_0^{\infty} e^{-\xi_t^2/\alpha^2} \cdot \cos(2\pi n \xi_t) \cdot d\xi_t \\ &= 4 \gamma_{\max} \frac{\sqrt{\pi}}{2} \cdot \alpha \cdot e^{-\pi^2 n^2 \alpha^2} \quad [22; \text{pg. 64}] \\ &= 2 \gamma_0 \cdot e^{-\pi^2 n^2 \alpha^2} \end{aligned}$$

$$\text{whence: } \gamma = \gamma_0 + \sum_{n=1}^{\infty} 2 \gamma_0 \cdot e^{-\pi^2 n^2 \alpha^2} \cdot \cos(2\pi n \xi_t).$$

It is seen that the *Fourier* expression is made up of a constant term, γ_0 , plus the sum of the periodic terms. The constant term is the mean value of γ . For η_t positive, the velocity due to the constant term is a uniform,

$$\frac{du_\gamma}{dy} = \frac{\gamma_0}{2}; \quad dv_\gamma = 0.$$

The velocity due to the periodic terms is given by,

$$\begin{aligned} \frac{du_\gamma}{dy} &= \frac{1}{2} \sum_{n=1}^{\infty} a_n \cdot e^{-2\pi n \eta_t} \cdot \cos(2\pi n \xi_t); \\ \frac{dv_\gamma}{dy} &= -\frac{1}{2} \sum_{n=1}^{\infty} a_n \cdot e^{-2\pi n \eta_t} \cdot \sin(2\pi n \xi_t). \end{aligned}$$

For a generally applicable solution, the value $\alpha = \frac{1}{5\pi} = 0.0637$ gives a sufficiently strong, while at the same time not excessive, concentration. The velocity due to the *periodic* terms becomes:

$$\frac{1}{\gamma_0} \frac{du_\gamma}{dy} = \sum_{n=1}^{\infty} e^{-\left(\frac{n}{5}\right)^2} \cdot e^{-2\pi n \eta_t} \cdot \cos(2\pi n \xi_t) \quad (9)$$

$$\frac{1}{\gamma_0} \frac{dv_\gamma}{dy} = - \sum_{n=1}^{\infty} e^{-\left(\frac{n}{5}\right)^2} \cdot e^{-2\pi n \eta_t} \cdot \sin(2\pi n \xi_t). \quad (10)$$

It is also readily seen, by comparison with the foregoing, that

$$\begin{aligned} \frac{1}{\gamma_0} \frac{du_\gamma}{dy} &= - \frac{1}{\sigma_0} \frac{dv_\sigma}{dy}; \quad \text{and} \\ \frac{1}{\gamma_0} \frac{dv_\gamma}{dy} &= - \frac{1}{\sigma_0} \frac{du_\sigma}{dy}. \end{aligned}$$

In the form of equations (9) and (10), the entire velocity field may be mapped in terms of the dimensionless parameters ξ_t and η_t . The evaluation was carried out by *H. Voellmy*, and the results are presented in Figures 10 and 11. If the first-approximation camber line is drawn to the proper scale

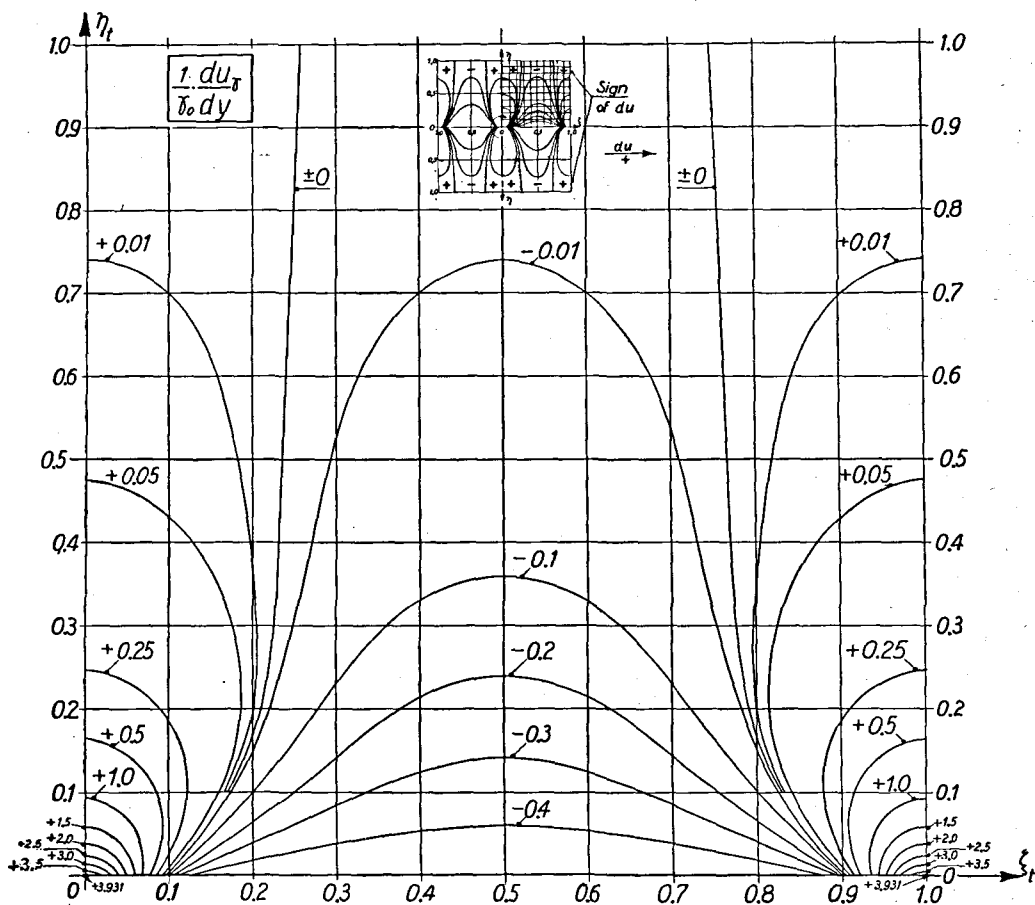


Figure 10: Periodic Velocity Component in X-Direction in the Field of a Thin Infinite Sheet of Circulation Distributed According to Figure 9

Values Associated with Curves Are $\frac{1}{\gamma_0} \frac{du_\gamma}{dy}$; $\frac{1}{\gamma_0} \frac{du_\gamma}{dy} = - \frac{1}{\sigma_0} \frac{dv_\sigma}{dy}$

on transparent paper with reference stations indicated, and placed over the charts, the velocity-component "influence factors"

$$\frac{1}{\gamma_0} \frac{du_\gamma}{dy}; \frac{1}{\gamma_0} \frac{dv_\gamma}{dy}; \frac{1}{\sigma_0} \frac{du_\sigma}{dy}; \text{ and } \frac{1}{\sigma_0} \frac{dv_\sigma}{dy}$$

may be read off readily. As shown for an hypothetical case in Figure 12, by placing station number 3 at the origin and reading the chart value under station number 6, we have ascertained the velocity-component influence factor $\left(\frac{1}{\gamma_0} \frac{du_\gamma}{dy} \right)_{6-3}$ (at 6 due to station number 3). In similar manner, the influence factors of all other stations are determined. Multiplication of the influence factors by the circulation strength of the associated layer, (γ_0) , then gives

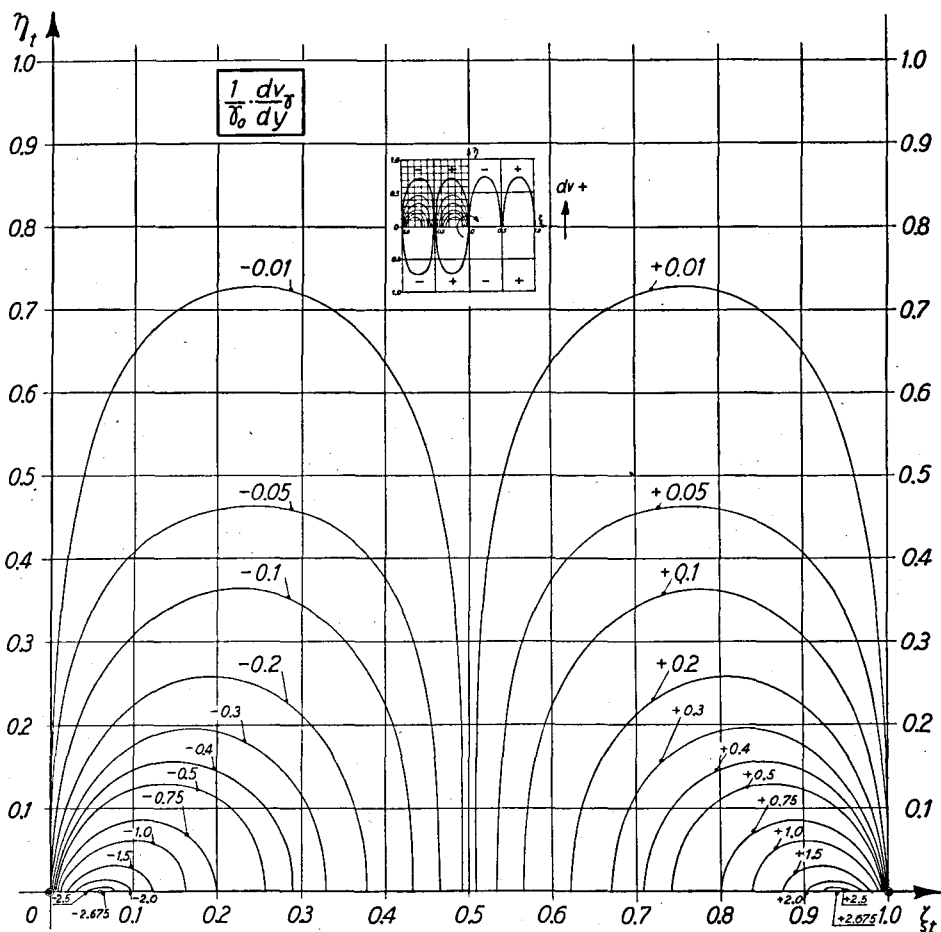


Figure 11: Periodic Velocity Component in Y-Direction in the Field of a Thin Infinite Sheet of Circulation Distributed According to Figure 9

Values Associated with Curves Are $\frac{1}{\gamma_0} \frac{dv_y}{dy}$. $\frac{1}{\gamma_0} \frac{dv_y}{dy} = -\frac{1}{\sigma_0} \frac{du_\sigma}{dy}$

the actual velocity components caused at station number 6 by all other stations. Plotting these velocity-components, as shown for the hypothetical case in Figure 13, and integrating graphically, gives the resulting net component $(u_\gamma)_6$, since

$$u_\gamma = \int_0^H du_\gamma = \int_0^H \frac{du_\gamma}{dy} dy = H \int_0^1 \left(\frac{1}{\gamma_0} \frac{du_\gamma}{dy} \right) \cdot \gamma_0 \cdot d\eta_H;$$

$$\text{where: } \eta_H = \frac{y}{H}. \quad \left(\text{Also, } \xi_H = \frac{x}{H} \right).$$

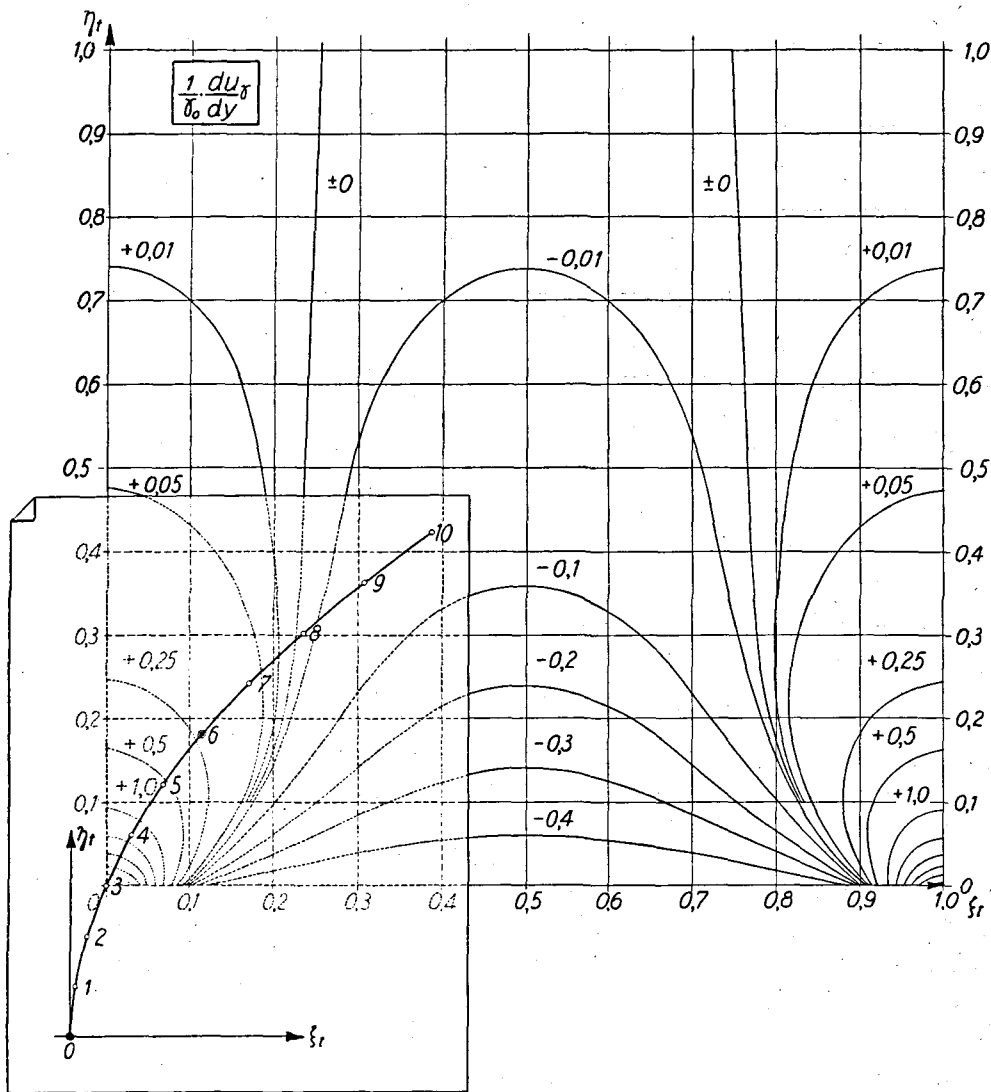


Figure 12: Use of the Periodic "Influence Factor" Diagrams (Figures 10 and 11) With Camber Line Drawn to Proper Scale on Transparent Paper, Velocity "Influence Factors" May be Readily Ascertained for the Computational Stations. In this Example, Station 3 Produces the "Influence Factor" $\frac{1}{\gamma_0} \frac{du_r}{dy} = +0.23$ at Station 6

The second-approximation velocity components v_r , u_σ , and v_σ are determined in similar manner. Figure 14 shows the actual determination of all velocity components for station number 2 (see Figure 4) as computed in this investigation. The components $\left(\frac{du_\sigma}{dy}\right)$ were all substantially zero.

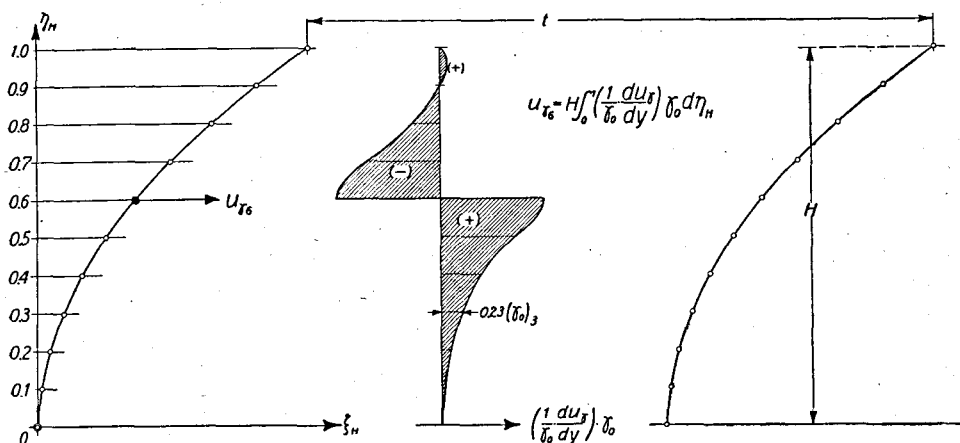


Figure 13: Integration of the Periodic Horizontal Velocity Components Caused by all Computed Stations to Obtain Net Horizontal Velocity Component for Station 6. (Hypothetical Example)

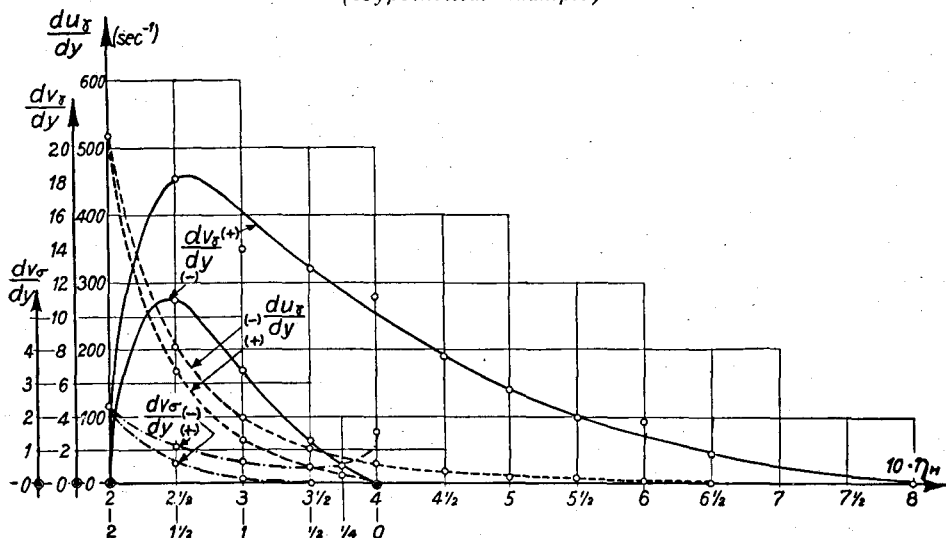


Figure 14: Representative Curves Showing Actual Determination of Periodic Velocity Components at Station 2 for Present Investigation

The η_H -axis Has Been Folded at 2 for Ease in Integrating. The $\frac{du_\sigma}{dy}$ -Values Were Negligibly Small, and Were Omitted

We have already noted that the *Fourier* expression for γ (or σ) consisted of a constant term, γ_0 (σ_0), plus the sum of the periodic terms. Account of the constant term γ_0 (σ_0) has already been taken in arriving at the first-approximation velocities. Returning to Figure 4, we now add to the first-approximation velocities the second-approximation velocity components resulting from strong periodic concentration of the circulation (source) distribution along x , and arrive at our final velocity hodograph.

We conclude the process by drawing the second-(final-)approximation streamline (camber line) by the tangent method (Figure 4)⁵⁾. Since the difference between first- and second-approximation camber lines is small, re-computation of the second-approximation velocity components, which were actually based upon the first-approximation camber line, is unnecessary. The line of Figure 4 marked "second-approximation camber line" is actually a streamline of the flow resulting from the placing of the x -direction circulation-(source-)distribution maxima approximately on that streamline. This line becomes the camber line of the actual cascade blades. The familiar "angular exaggeration", ϵ , associated with cascades is apparent in Figure 4.

It will now be appreciated why we have stated that the bell-shaped curve of Figure 9 gave a sufficient and yet *not excessive* concentration of circulation (sources). A greater degree of concentration would result in: (1) larger finite discontinuities to be integrated in Figures 13 and 14; and (2) the necessity for a recomputation of the second-approximation velocity components due to the falling of the second-approximation streamline *outside* the region of the maxima as located by the first-approximation camber line. To be sure, greater accuracy is attainable by use of stronger x -concentrations, but the additional time required for further approximations then required is not commensurate with the objective of attaining a reasonably accurate result with a reasonable expenditure of time.

It will be noted that the final velocity computed for the camber line point $y = y^*$ has undergone a small percentual change from the value used to determine the scale for the $\sigma_0 = f(y)$ curve. If an exact value of maximum thickness is required, this scale should be recomputed. In general, the *second*-approximation velocity components resulting from the periodic terms of the *source*-distribution equation are very small, and for low-stagger cascades of not more than 12 % maximum thickness they are *negligibly* small. Re-computation of the second-approximation velocity components will in general not be required, even when an exact maximum thickness value is required, as a result of the change in the scale of $\sigma_0 = f(y)$ at this point. It will be necessary only to correct the component v_{σ_0} by application of a constant factor, and to plot the final hodograph and camber line *after* application of this correction. If an *exact* value of maximum thickness is not required, no correction of the final velocity hodograph for change in σ_0 -scale will be needed.

With a camber line and its associated flow velocities known, blade thickness, d (to be measured normal to the camber line) is obtained by assuming *all* the periodically-distributed sources to be brought within the actual blade, whence

$$d = \frac{t \cdot \int_0^y \sigma_0 \cdot dy}{C}.$$

The final blade profile may then be plotted, and the geometrical definition of the cascade is complete. Section VII will indicate the degree of accuracy within which the cascade used in this investigation (derived from Figure 4) produced the turning angle which was desired of it. The cascade

⁵⁾ The fact that the trailing edges of the first- and second-approximation camber lines are the same point in Figure 4 is coincidental, and not a requirement.

profile used was based upon an elliptical distribution of circulation and upon the σ_0 -curve of Figure 3. The resultant blade profile is shown in Figure 15, and its coordinates are given in Table I. A finite thickness of the blade at the trailing edge is chosen because of manufacturing considerations. The similarity between the thickness distribution of this blade and that of N.A.C.A. 65-010 was intentional.

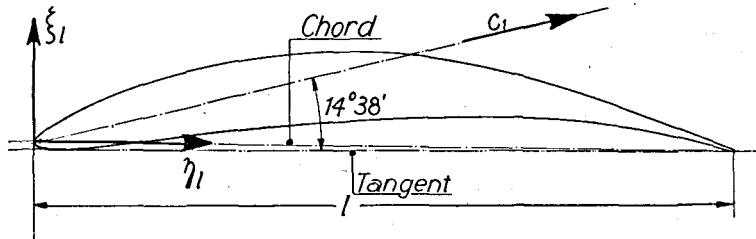


Figure 15: Blade Form as Determined by Continuum Theory for Present Investigation
 C_1 Is Inlet Velocity Far Upstream from Cascade (Fig. 4)

Table I. Coordinates of Cascade Blade

$100 \times \xi_l$			$100 \times \xi_l$		
$100 \cdot \eta_l$	Upper	Lower	$100 \cdot \eta_l$	Upper	Lower
0	0.414	0	45	13.747	3.823
1	1.642	-0.580	50	13.651	4.182
2	2.429	-0.718	55	13.223	4.431
3	3.078	-0.738	60	12.450	4.624
4	3.671	-0.718	65	11.470	4.693
5	4.224	-0.676	70	10.297	4.610
7.5	5.480	-0.400	75	8.916	4.375
10	6.625	-0.110	80	7.315	3.906
15	8.585	0.538	85	5.576	3.340
20	10.186	1.242	90	3.782	2.457
25	11.456	1.960	95	1.918	1.284
30	12.436	2.540	97.5	1.063	0.594
35	13.085	3.036	100	0.166	-0.166
40	13.499	3.464			

Nose radius = 0.666 % of L .

II. B. Cascade Blade Static Pressure Distribution From Continuum Cascade Theory

In the preceding section, the theoretical computation of a cascade blade camber line, and profile thickness to be superimposed thereon, was carried out. The determination of the approximate static pressure distribution on the blade profile so established also follows from the *Ackeret* theory. We recall that vortex strength was continuously distributed in the direction of the cascade axis in accordance with a bell-shaped distribution curve periodic with the blade spacing and showing strong maxima in the vicinity of the blade camber lines. We now assume *all* the vortex strength which was previously

distributed in the x -direction to be brought *within the blade profiles*. Figure 16 shows a blade element of length ds , within which we assume the circulation $\gamma_0 \cdot t \cdot dy$ to be concentrated. This circulation produces velocity component ΔC_γ at the blade-element surface. According to *Stokes' Law*, we may write, for thin blades:

$$\gamma_0 \cdot t \cdot dy = 2 \cdot \Delta C_\gamma \cdot ds,$$

$$\text{whence: } \Delta C_\gamma = \frac{\gamma_0 \cdot t}{2} \cdot \frac{dy}{ds} \approx \frac{\gamma_0 \cdot t}{2} \cdot \frac{C_n}{C},$$

where C is the velocity calculated in the foregoing section for a point on the camber line, and C_n is its component in the direction normal to cascade axis.

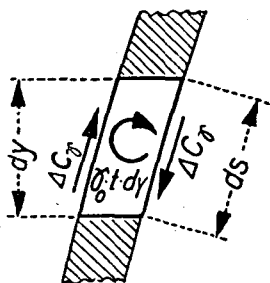


Figure 16: *Approximation of Surface Velocity Components Due to Circulation*

The approximation, rather than the equality, sign was used in the second foregoing equation because $\frac{dy}{ds}$ is equal to $\frac{C_n}{C}$ only where the local blade thickness does not change rapidly. At the nose of a round-nosed blade, the approximation obviously loses its validity. The region in which the approximation is invalid is extremely small, and since the method fails to show a stagnation point at the nose in any case, this added approximation does not weaken its performance.

The value of ΔC_γ computed from the foregoing equation is added to $C_{(camber\ line)}$ on the suction side of the blade and subtracted on the pressure side to obtain the approximate final blade-surface velocity C . The *Bernoulli* equation gives

$$P_1 + \rho C_1^2/2 = P + \rho C^2/2.$$

Setting $P - P_1 = \Delta P$, we have:

$$\frac{\Delta P}{\rho C_1^2/2} = 1 - \left(\frac{C}{C_1}\right)^2.$$

The theoretical pressure distribution determined for the cascade blade used in the present investigation is given in Figure 34 (pg. 54) by the curve marked "Theory". It may be noted that for the general case, where no ex-

perimental pressure-distribution curve is available for comparison, a useful result is obtained by projecting the blade profile upon lines parallel and perpendicular to the cascade axis and then plotting the theoretically-determined pressures relative to these lines. The results are two closed pressure-distribution curves, the areas within which are proportional to pressure-resultant force components perpendicular and parallel to the cascade axis, F_N and F_T , respectively (For example, F_T may be obtained from Figure 34.) These components may be compared with the theoretical forces based upon the pre-determined velocity diagram (Figure 1), which are given by the familiar equations:

$$F_T = \rho \cdot C_n \cdot t \cdot (C_{u2} - C_{u1});$$

$$F_N = \rho/2 \cdot t \cdot (C_{u2}^2 - C_{u1}^2);$$

$$\frac{F_N}{F_T} = \frac{C_{u2} + C_{u1}}{2 C_n}.$$

This comparison is given in Section VI. A. 1, Table IV.

II. C. Streamlines Directly Ahead of and Behind Cascade Blade

The fluid streamlines which terminate at the forward and rear stagnation points (nose and trailing edge) of a dynamically loaded blade deviate materially, in the vicinity of the blade, from the vectors of mean velocity of approach and discharge. This effect of circulation about the blade is often referred to as "angular exaggeration", and is a function of the lift coefficient of the blade.

Since the end (outermost) blades of the cascade are joined at nose and trailing edge by the inlet and outlet side walls of the cascade, the streamlines terminating at nose and trailing edge of these blades are not free to assume the curvature associated with angular exaggeration, but are constrained to follow the wall conformations. In order to estimate the order of magnitude of the disturbance resulting from the use of straight inlet and outlet side walls, the theoretical stagnation-point streamlines for the intended cascade arrangement were calculated by extension of the continuum method (II A) to the area ahead of and behind the cascade. The resultant streamlines are shown in Figure 17. From Figure 17 it may be seen that the streamline curvature is highly localized, these lines becoming parallel to the vectors of mean inlet and outlet velocity at a distance of about $0.3 H$ from the cascade. Lateral deviation between streamline and mean vector at this point of maximum deviation was computed to be $0.0065 H$ (0.75 mm) for inlet and $0.0044 H$ (0.51 mm) for outlet sides.

Since the maximum deviations were of the same order of magnitude as the boundary layer contraction thickness, and in view of the number of blades separating the center blade from this disturbance, the inlet and outlet side walls were designed to be straight. For cascades of much higher lift coefficients (design c_a for this investigation = 0.76) or lesser number of blades, further consideration of this point may be indicated.

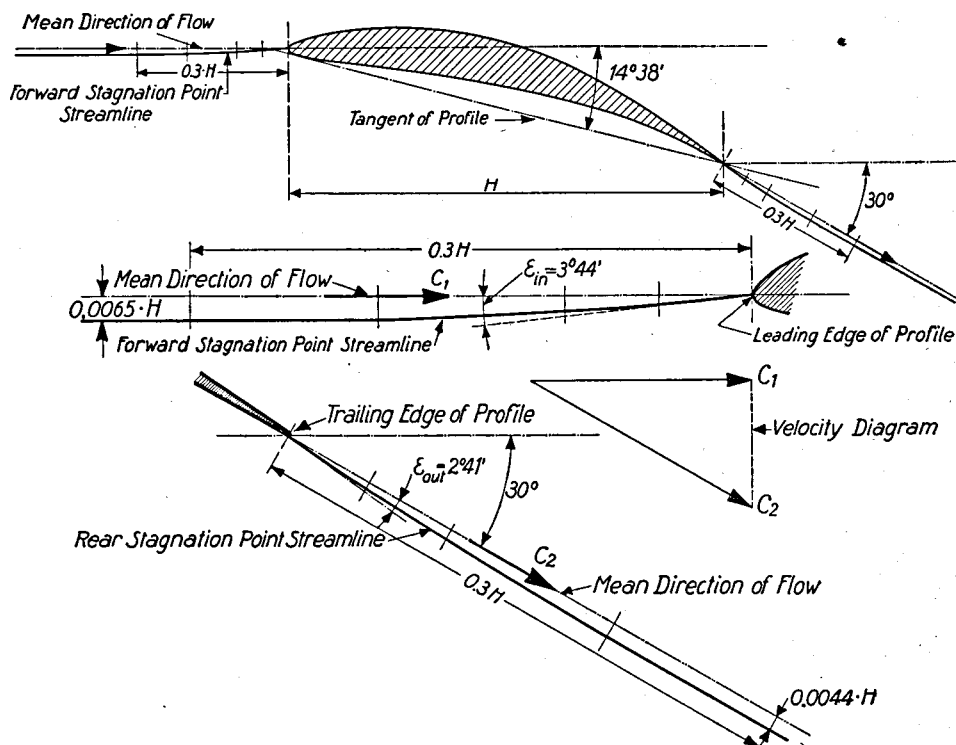


Figure 17: *Computed Streamlines Associated with Cascade Blade Forward and Rear Stagnation Points*
 $c_a = 0.76$; $H = 115.9$ mm

III. Test Equipment

A. Wind Tunnel (up to Test Section)

Figure 18 indicates the permanent tunnel arrangement up to the settling chamber. The single-stage axial fan with adjustable-pitch blades is driven by a 40 H.P.—D.C. motor permitting accurate speed control over a wide range. The honeycomb straightener following the first diffuser is made of 1 mm plates forming 50 mm square passages 300 mm in length, which effectively remove residual rotation. The air then enters the settling chamber through a second diffuser, and immediately passes through three successive screens which tend to even out velocity irregularities over the cross-section. The screens are fabricated from 1 mm sheet metal with 8 mm square holes stamped on 12 mm centers.

Barograph records of settling-chamber static pressure, P_K , showed, for the completed test rig, fluctuations of the order of one percent in two

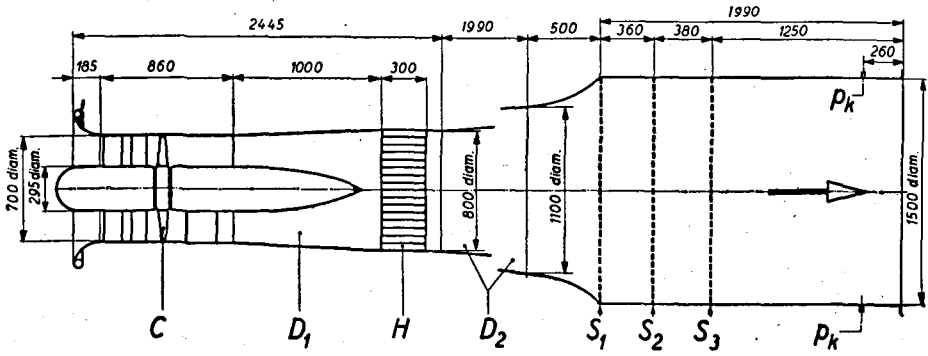


Figure 18: *Permanent Wind Tunnel Equipment Utilized for Cascade Tests.* C = Axial Flow Fan. D_1 ; D_2 = Diffusing Sections. H = Honeycomb Straightener. S_1 ; S_2 ; S_3 = Screens for Turbulence Reduction and Flow Uniformity. P_k = Settling Chamber Static Pressure (All Dimensions Shown Are in Millimeters)

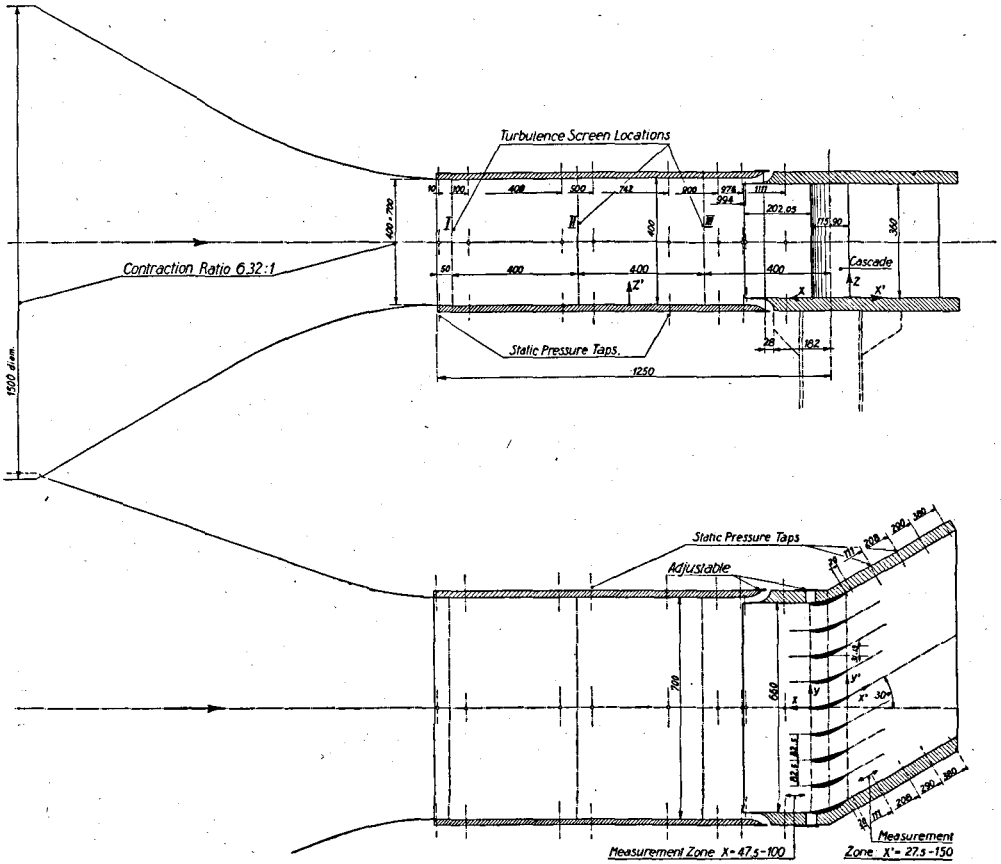


Figure 19: *Approach and Test Sections of Cascade Tunnel.* Balance (Not Shown) Is Mounted Benath Cascade (All Dimensions Shown Are in Millimeters)

minutes time for fixed setting of motor main field rheostat. These fluctuations were traced to variations in the motor supply voltage, and could be reduced to approximately $\frac{1}{2}\%$ by hand control of a supplementary small rheostat, under which conditions the fluctuations were of short (1—2 seconds) duration.

Figure 19 shows the special cascade testing rig following the settling chamber. The circular flow-cross-section of the settling chamber was changed to rectangular in the nozzle, whose contraction ratio was 6.32:1. From the nozzle outlet, the flow passed through a parallel-walled approach section 990 mm long, in which were constructed, at regular intervals ahead of the cascade center line, 3 vertical slots for receiving wire screens for the production of turbulence. The approach section was of 20 mm plywood, well reinforced and supported, but nevertheless subject to the minor local changes in shape which are characteristic of this material.

The approach section terminated in the boundary-layer take-off slots. Tunnel pressure being substantially greater than room pressure at this point, the boundary layer was simply separated from the main air flow by a metal plate forming the inner surface of the test-section channel, and discharged through a diffuser-shaped channel into the room, the area of main-flow cross section being diminished accordingly. Throttling plates were provided at the take-off slot outlets to permit regulation. Proper adjustment of the boundary-layer take-off was indicated by equality of static pressures measured on the inner (main-flow) side of the separating plate at a distance of 4 mm from its leading edge, and that measured on the approach-section parallel wall 14 mm upstream of the separating-plate leading edge, under which conditions the streamlines of the main flow are parallel with the tunnel axis over this zone.

III. B. Test Section of Tunnel

The entire cascade test section assembly was mounted separately on a massive steel foundation in order to eliminate vibration. The test section was mechanically isolated from the compressor and other upstream structure by the boundary layer take-off slots.

Figure 19 indicates the attitude and dimensions of the cascade arrangement tested. The inlet cross-sectional area was fixed by the requirement of attaining a reasonable, although low, inlet velocity within the capabilities of the available tunnel fan. With the area fixed by this consideration and by the theoretical pressure drop, the ratio of cascade breadth (number of blades) to height (length of blades) was necessarily a compromise between the conflicting requirements of maximum attainable number of blades (minimum length) and of favorable aspect ratio (maximum length) of the individual blades. Concurrent considerations affecting aspect ratio were the desire for a reasonably high Reynolds number (large chord) and for a blade lift coefficient of approximately 0.8 (arbitrarily chosen). The mechanical strength and permissible tip deflection of the center (reference) blade of the cascade were also considered, but were not limiting factors of the final arrangement.

All blades of the cascade with the exception of the center blade were fastened at both ends to the horizontal (top and bottom) walls of the test section. The center blade, the forces upon which it was desired to measure directly, was rigidly mounted as a cantilever at its lower end, the upper end remaining free with a clearance of 0.15 mm between it and the upper wall. This blade passed through a labyrinth-type aperture in the lower wall to its point of fixation upon a force-measuring balance (IV. E.).

The center blade was of brass, and was fitted (at mid-height of test section) with static pressure holes about its circumference. The two blades adjacent to the center blade were of aluminum, while the remaining blades were of laminated hardwood⁶⁾. Surfaces were all highly polished and were accurate to within 0.04 mm. The development of the blade profile was discussed in (II. A.).

The exit walls were continuous with the trailing edges of the outermost blades, being pivoted at those points. These walls were 400 mm in length in order to shield the cascade from the pressure disturbances of the jet "mixing zone" where the flow discharged into still air, and were provided with static pressure taps at mid-height at the locations shown in Figure 19.

A plexiglass window 10 mm thick was built into the upper tunnel wall directly over the center blade, and carried 113 0.8 mm holes for static pressure measurement in this region. This window was found to be most useful in positioning pressure-measuring sondes during operation.

With the original purpose of drawing off (or supplying) air at the leading edges of the outermost blades to correct the disturbances discussed in Section II. C., the side walls of the test section were interrupted 12 mm ahead of the blade leading edges. Adjustable plates were provided to permit regulation of flow (in or out) at these points. Subsequent tests showed only adverse effects resulting from withdrawing (or supplying) small quantities of air at these points, and the adjustable openings were accordingly closed at all times.

Measuring instruments were inserted into the flow ahead of and behind the cascade through the upper wall; traverses parallel to the cascade axis were made possible by cutting out strips of the upper wall parallel to the cascade in the positions marked "Measurement Zone" in Figure 19 and dovetailing in their places new sections which could be moved laterally (parallel to cascade axis) while carrying the measuring equipment.

The balance (not shown on Figure 19) was mounted directly beneath the lower test section wall upon the same heavy foundation which carried the test section.

Walls of the test section were of 40 mm highgrade plywood, and remained free of distortion throughout the investigations.

⁶⁾ Calculated maximum blade deflections were:

Center blade	$0.14 \text{ mm} = 0.0017 \cdot t$ at free end)
Blades adjacent to center	$0.02 \text{ mm} = 0.0003 \cdot t$ (at mid-height)
Remaining blades	$0.14 \text{ mm} = 0.0017 \cdot t$ (at mid-height)
$(t = \text{Blade spacing} = 82.5 \text{ mm})$	

III. C. Cascade Force-Measuring Balance

The principle of *Amsler* indicates that a non-rotating cylindrical ("sleeve") bearing mounted upon a rotating shaft is free from the effects of "dry" friction for motion in the direction of the shaft axis. After experimental verification of the practical validity of this principle (see Section IV. A.), it was applied to the construction of a force-measuring balance, in the manner shown in Figure 20. By extending the fundamental unit [Figure 20-(1)] to two rotating parallel shafts carrying cylindrical bearings which are mechanically connected, a platform *A* is obtained which is free to move in the axial direction of the two shafts and in no other, without the impediment of dry friction [Figure 20-(2)]. To give this "floating" platform a point of stable equilibrium, two opposed coil springs may be attached to the platform and to the fixed structure. A known axial force, to balance the axial component of any unknown force applied to the platform, may be applied by a very thin, axial, horizontal steel band affixed to the platform and leading over a frictionless pulley *G* to a weight pan. Adding weights to bring the "floating" platform to its no-load equilibrium position then constitutes a determination of the component, in the direction of the shaft axis, of any force applied to the platform.

To permit measurement of the component of an applied force in *any* desired direction in the horizontal plane, two additional plates *C* and *D* are added to the balance, one on top of the floating carriage *A* and one beneath the plate *B* carrying the rotating shafts [Figure 20-(3)]. To the foundation plate *C* is affixed a rigid (hollow) cylinder *E* which passes vertically upward between the two shafts and through platform *A* to a point just beneath the plate *D*. Insertion of tapered pins *F* through the plate *D* into matching holes in the upper end of the cylinder *E* serves to lock plates *C* and *D* rigidly together, in which condition the basic unit of the balance, constituting plates *A* and *B* with the two shafts, may be rotated freely about the vertical axis without altering the position of the uppermost plate *D*, to which the unknown force may now be thought to be applied. Having positioned the central unit of the balance so that the shafts lie in the direction in which it is desired to measure the force component, the aforementioned taper pins *F* are removed, and the two upper plates *A* and *D* are mechanically clamped together, as are the two lower ones *B* and *C*. The two upper plates together then constitute the floating carriage for the weighing process, and the two lower ones the fixed foundation. Any dynamically-loaded object which may be mounted to the upper plate *D*, such as a blade of a cascade, is thus undisturbed (relative to other fixed structure) during the process of determining force components in as many directions as desired. Should it be desired to change the attitude of a dynamically-loaded object for separate tests (e. g. determination of forces on a blade for various angles of attack), it is merely necessary to add a third plate above *D*, which plate may then be turned and indexed relative to plate *D*.

Axial motion of the present balance is restricted by mechanical limit stops (total motion = ± 0.05 mm) which serve also as electrical contacts and provide indication of "zero-positioning" of the floating carriage. Shaft drive is by a small variable-speed electric motor. Lubrication of the floating bearings is accomplished by gravity flow of oil from reservoirs *R* at one

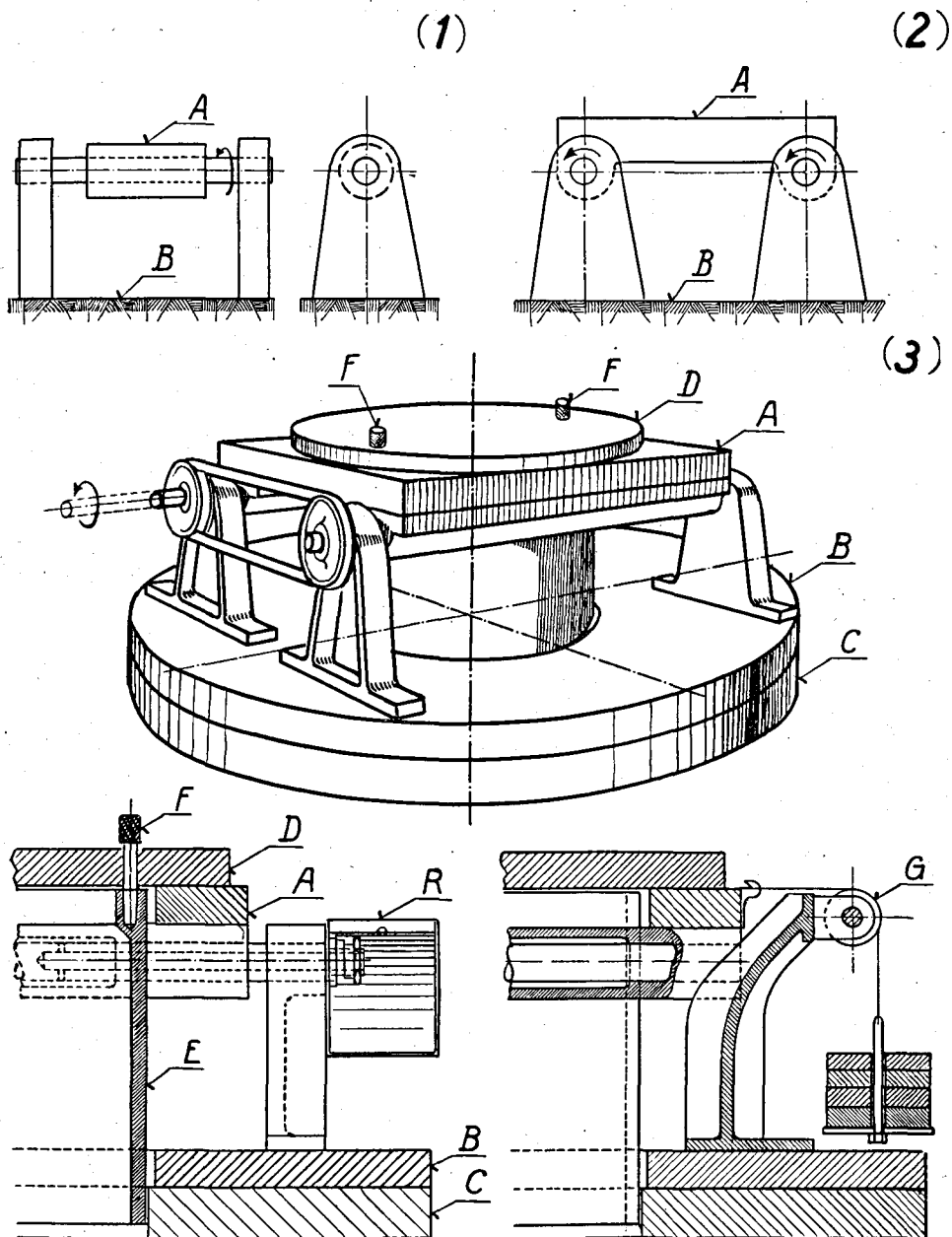


Figure 20: Schematic Drawing of Cascade Balance (Simplified), Showing Steps in Development

A = Axially "Floating" Platform of Basic Unit. *B* = Shaft Carrier Plate. *C* = Foundation Plate. *D* = Auxiliary Plate Upon Which Blade Is Mounted. *E* = Cylinder Rigidly Fixed to Foundation Plate *C*. *F* = Taper Pins Locking *D* to *E*. *G* = Pulley.
R = Oil Reservoirs for Main Bearing Lubrication

end through axial holes in the shafts to a series of radial passages at mid-span, where it discharges into an annular space between bearing shell and shaft. From this space the oil, under slight pressure, flows very slowly outward through the bearings and is recirculated by a small pump which maintains oil level in the reservoirs.

Results of balance calibration are given in Section IV. B., which indicates a high degree of accuracy in the measurement of force components of greatly different relative magnitudes.

III. D. Instrumentation

Air flow direction was determined in a usual manner by two 1.0 mm-diameter (0.7 mm bore) impact tubes at an angle of 90° to one another at their open (upstream) ends, the distance between centers of openings being 1.2 mm. The calibration of this directional device showed a substantially linear variation of the difference in pressures of the two tubes when the angle was varied through fifteen degrees to either side of the zero (i. e., equal-pressure-reading) setting. A deviation of one degree from the zero position corresponded to a difference in pressure of the two tubes equal to 4.5 % of the stream dynamic pressure, so that flow angle was easily ascertainable within 0.05 degree for dynamic pressures in excess of about 5 mm H_2O .

Static and total pressures were measured with tubes of 1.0 and 1.3 mm outside diameter and 0.7 and 0.8 mm bore. The 2 (4) static tube side openings were 0.4 (0.5) mm in diameter and located 5 (6.5) mm from the nose. Directional sensitivity of these tubes was as reported in reference [23]. For a very accurate determination of pressure distributions over the tunnel height, where the insertion of an ordinary tube from the top into the flow would have yielded erroneous results due to varying degrees of obstruction of the flow, a special instrument having the characteristic of constant frontal area at all heights was used. This consisted simply of a hollow guide piece in the form of a symmetrical profile which extended over the entire tunnel height and into which special small static or total pressure tubes might be inserted vertically to the desired height. Overall width of instrument normal to flow was 3 mm.

Pressure indications within 0.01 mm H_2O were read from micro-manometers constructed at the Institute [24].

IV. Preliminary Experimental Work

A. Test of the Amsler Principle for Application to the Construction of a Balance

Included in the present investigation is the measurement of the actual forces exerted upon a cascade blade by the streaming fluid. Since the moment of these forces in the plane of flow was not required (lacking significance), the problem of construction of a suitable force-measuring balance

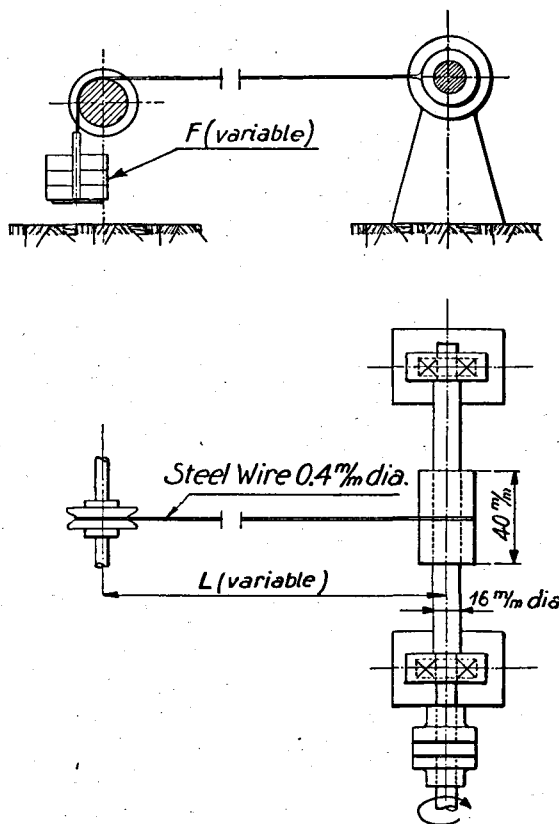


Figure 21: Arrangement for Test of Friction Properties of Cylindrical Bearing with Axial Freedom on a Rotating Shaft

was simplified. The requirements of rather high accuracy and minimum permissible motion during the weighing process were, however, to be met. The well-known *Amsler* principle of the freedom of a sleeve bearing upon a rotating shaft from axial dry friction afforded a possible solution. Preliminary investigations upon a small model (Figure 21) substantiated the meagre literature [25, 26] upon the rather obvious and certainly commonly-used principle, and proved its suitability for balance applications (see III. C.).

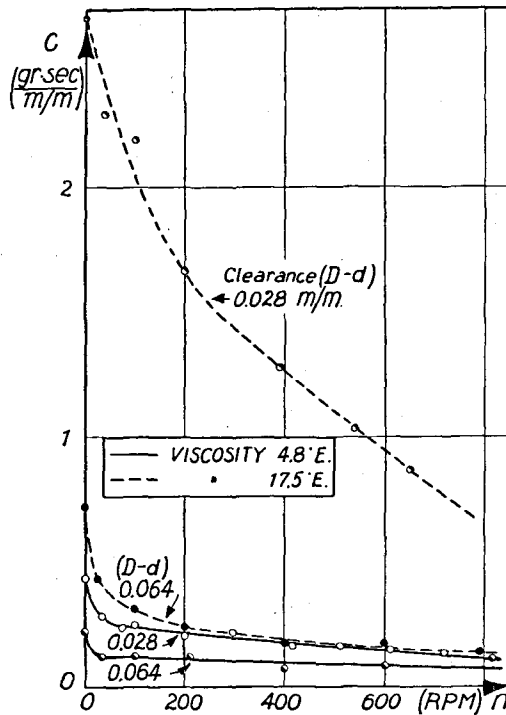


Figure 22: Measured Damping Constant of a Cylindrical Bearing with Axial Freedom on a Rotating Shaft
Developed Area of Bearing = 20.1 cm²

Figure 21 shows a rotating steel shaft of 16 mm diameter carrying at mid-span a bronze cylindrical bearing 40 mm in length. Clearance between the bronze bearing and shaft was 0.028 mm (on the diameter), later increased to 0.064 mm. Lubrication was by oil cup gravity feed through a small radial hole at the top of the bearing. A fine steel wire was affixed to the floating bearing and led horizontally over a suitable pulley to a weight pan. Variation of: (1) wire length to pulley; and (2) tension in the wire; permitted attainment of an accurately variable restoring force when the bearing was axially displaced from its equilibrium position (i. e., wire perpendicular to shaft). The combination of wire tension, F , and wire length, l , gave an equivalent restoring "spring constant", F/l . As differentiated from normal viscous damping, the undesirable effect of "dry" friction (i. e., absence of axial motion in the presence of a small axial force) would be indicated by a difference between the points at which the bearing came to rest after axial displacement first to one and then to the other side of the geometrical equilibrium position. A qualitative measure of this undesirable dry friction effect resulted from measurement of the distance between the two points of rest and multiplication by the "equivalent spring constant", F/l . Axial position of the bearing was ascertainable to within 0.003 mm by optical projection.

Up to the maximum load which the model was capable of sustaining,

namely 20 kilograms or 3.1 kg/cm^2 of projected bearing area, no axial dry friction whatever was detectable within the limits of experimental accuracy. With a minimum "equivalent spring constant" of 50 milligrams per millimeter, this limit of experimental accuracy was 0.15 milligram.

Oils of viscosity 17.5° and 4.8° Engler (at 20°C), were tested with bearing clearances (diametral) of 0.028 and 0.064 millimeters. In all cases, no axial dry friction effect was ascertainable within the experimental accuracy of 0.15 milligram through a speed range of 50 to 800 R.P.M. Decreasing bearing clearance and increasing viscosity of oil served merely to increase the damping constant as predicted by theory (see Figure 22).

Tests were also made without lubrication. For the brief period during which the rubbing surfaces remained uncontaminated by the products of mechanical abrasion, the model showed the same frictionless characteristics as in the lubricated condition.

IV. B. Static Calibration of Balance

The balance constructed for accurate measurement of blade forces (see III. C.) was subjected to a static-force calibration test. This consisted of applying a known static force and determining its magnitude and direction by balance measurements of its components in two arbitrary directions differing by 90° . The force range was from zero to the computed maximum total force on a single cascade blade, or two kilograms. Figure 23 shows

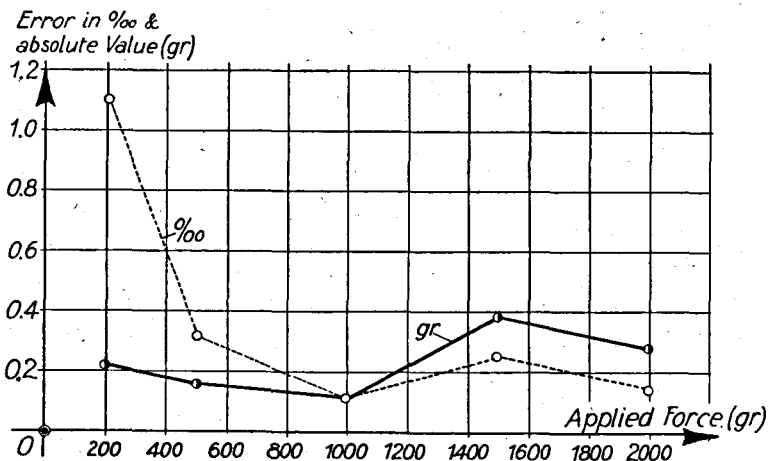


Figure 23: Static Calibration of the Cascade Balance
(‰ = Per Mil, or Parts Per Thousand)

the results of one of the first such calibrations carried out. The direction of the applied force was the same for all loadings, while the measured angles indicated a spread of $\pm 3'.5$ (0.06 degrees) between all readings.

Subsequent similar tests by unfamiliar personnel, after somewhat rough handling of the balance, have given maximum errors up to 4 per mil, the

average error of 28 tests being 1.4 per mil. In all tests, the angular determination has been constant within four minutes of arc. For use by an experienced operator, the *maximum* magnitude error can be taken as 2 per mil with safety, and the maximum direction error as 0.05 degree using the "null" method (see V. B. 2).

IV. C. Determination of Turbulence for Free Tunnel Flow and Behind Wire Screens

One of the effects to be investigated was that of turbulence. Since limitations precluded the application of the hot-wire measuring technique for turbulence measurement, use was made of the "pressure sphere" [27] for turbulence-intensity determination as adequate for the present purpose. The extensive available experimental data [27, 28, 29, 30] upon the *scale* of turbulence downstream from wire screens was used to estimate this parameter with sufficient accuracy in view of its much lesser influence [29]. The *intensity* of turbulence (assumed isotropic) is defined in the usual manner by

$$\text{Turbulence intensity} \equiv \frac{\sqrt{u^2}}{U}$$

where: u = fluctuation velocity in x -direction
 U = mean flow velocity in x -direction.

Turbulence *scale or length* is defined by

$$L \equiv \int_0^\infty R(y) \cdot dy$$

$$\text{where: } R(y) = \frac{\overline{u_1 u_2}}{\sqrt{\overline{u_1^2}} \sqrt{\overline{u_2^2}}}$$

1 and 2 are points distance y apart in plane normal to flow.

The practice of defining the intensity of turbulence by the use of spheres is long standing [31, 32, 33, 34]. The resistance coefficient of a sphere is of the order of 0.5 at low and about 0.1 at high Reynolds No. A sharply-pronounced transition between these values takes place at a value of the Reynolds number which is called the "critical" Reynolds number⁷⁾. Utilization of this fact to define wind tunnel turbulence intensity was first

⁷⁾ The decrease in resistance coefficient is due to delay in separation from the surface. At low Re , the Reynolds number formed from the boundary layer thickness and velocity in the adjacent free stream is sufficiently low to permit maintenance of a laminar boundary layer up to the point where separation occurs, near the cross-stream diameter of the sphere. Increasing the stream Re ultimately increases the boundary layer Re to the point where transition from laminar to turbulent boundary layer occurs ahead of the laminar separation point. Separation is then delayed, occurring appreciably farther back on the sphere, and reducing the area of negative pressure. The greater or lesser intensity of turbulence in the fluid stream manifests itself by an earlier or later transition of the boundary layer from laminar to turbulent.

proposed by *Prandtl* [31] and later substantiated by correlation with hot wire measurements of *Dryden* [32] and others. To obviate the labor and complication of making force measurements required for the determination of resistance coefficient, *Dryden* [27, 33, 34] and *Hoerner* [35] independently developed the use of a pressure sphere to produce an easily measurable pressure relationship similar in trend to the drag coefficient curve. The value of this coefficient, later defined, is about 1.4 at low Re , and decreases suddenly to about 0.9 at some critical point as the Reynolds number is increased. Adopting the definition of "critical" Reynolds number as that value of Re for which the sphere drag coefficient is equal to 0.3, it was found [36] that the corresponding value of the pressure coefficient as defined by *Dryden* was approximately 1.22. This pressure coefficient is defined as the difference between impact (total) pressure at the nose of the sphere and the static pressure on the sphere at an azimuth of $157\frac{1}{2}^\circ$ from the nose, divided by the free-stream velocity pressure (see Figure 24).

$$K_P = \frac{P_g - P_{s(h)}}{\rho V^2 / 2}$$

$$(K_P)_{crit} \equiv 1.22 = \left[\frac{P_g - P_{s(h)}}{\rho V^2 / 2} \right]_{crit}; \quad Re_{crit} = \frac{D \cdot V_{crit}}{\nu}$$

Having established the "critical" Reynolds number experimentally, the experimental data of *Dryden* may be utilized for the estimation of the absolute magnitude of turbulence scale and intensity.

Systematic variation of turbulence at the plane of the cascade is obtained by mounting any one of three geometrically similar wire screens, each of different mesh length, at any one of three stations upstream of the cascade (Figure 24). A pressure sphere of 118.8 mm diameter was mounted in the position normally occupied by the cascade, and flow restriction minimized by removing both side and the upper tunnel walls. Curves of pressure coefficient K_p versus Re were measured (Figure 24) for each screen in each position, and the corresponding "critical" Re established by noting the value corresponding to $K_p = 1.22$.

Turbulence intensity behind screens was determined from *Dryden's* curves of intensity as a function of critical Reynolds number, with screen mesh lengths as a parameter, for a 127 mm sphere [27]. Turbulence scale was taken from *Dryden's* curves of scale as a function of distance, in mesh lengths, behind screens geometrically similar to those employed here, with mesh length as a parameter. For the tunnel without screens, since turbulence length was wholly unknown, the approximate value of turbulence intensity was taken from *Dryden's* earlier data [32] giving intensity directly as a function of critical Reynolds number, and the corresponding length then

derived from the more recent data correlating Re_{crit} with $\left(\frac{\sqrt{u^2}}{U}\right) \cdot \left(\frac{D}{L}\right)^{1/5}$. Results are shown in Table II. The validity of this procedure is indicated by the fact that Re_{crit} is a function of $\frac{\sqrt{u^2}}{U} \left(\frac{D}{L}\right)^{1/5}$, (where D = sphere diameter; L = scale of turbulence); i. e., a percentage change in $\frac{\sqrt{u^2}}{U}$ is equivalent to

a percentage change in $\left(\frac{D}{L}\right)$ five times as great. The validity was further substantiated by satisfactory comparison of the results with *Dryden's* curve of $\frac{\sqrt{u^2}}{U} \left(\frac{D}{L}\right)^{1/3}$ as a function of Re_{crit} .

Table II. Turbulence Parameters as Determined With Pressure Sphere

Screen No. (See Fig. 24)	Screen Location (See Fig. 24)					
	1		2		3	
	$\frac{\sqrt{u^2}}{U}$	L; mm	$\frac{\sqrt{u^2}}{U}$	L; mm	$\frac{\sqrt{u^2}}{U}$	L; mm
1	0.020	5.9	0.026	5.1	0.034	4.4
2	0.014	4.9	0.019	3.9	0.026	3.0
3	0.011	4.6	0.014	3.4	0.020	2.1
None	0.01	≈ 7.2				

IV. D. Flow Uniformity in the Tunnel Test Section

To insure that the pressure field in the cascade test section was not influenced by upstream pressure irregularities arising from the contracting nozzle (see Figure 19), the static and total pressure distributions were measured immediately at the nozzle outlet (1160 and 1200 mm ahead of cascade),

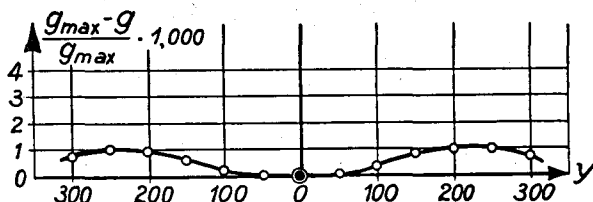


Figure 25: Total Pressure Variation Across Contraction Nozzle Throat
 $x = 1200$ mm; $z' = 200$ mm; $(P_{g_1})_{max} = 71.1$ mm H₂O

and the static pressure again at 660 mm ahead of the cascade. Figure 25 indicates a maximum variation of 0.1 % in total pressure in the nozzle throat. This variation decreased to still lower values over most of the channel width in the subsequent parallel sections [see Figures 30; 31 (A)]. Figure 26 indicates the disturbed static pressure field at the nozzle outlet, while Figure 27 shows the rapid smoothing-out of this field after the flow has progressed through 45 % of the parallel approach section. From these measurements, it was concluded that the cascade would be influenced by no appreciable upstream disturbances.

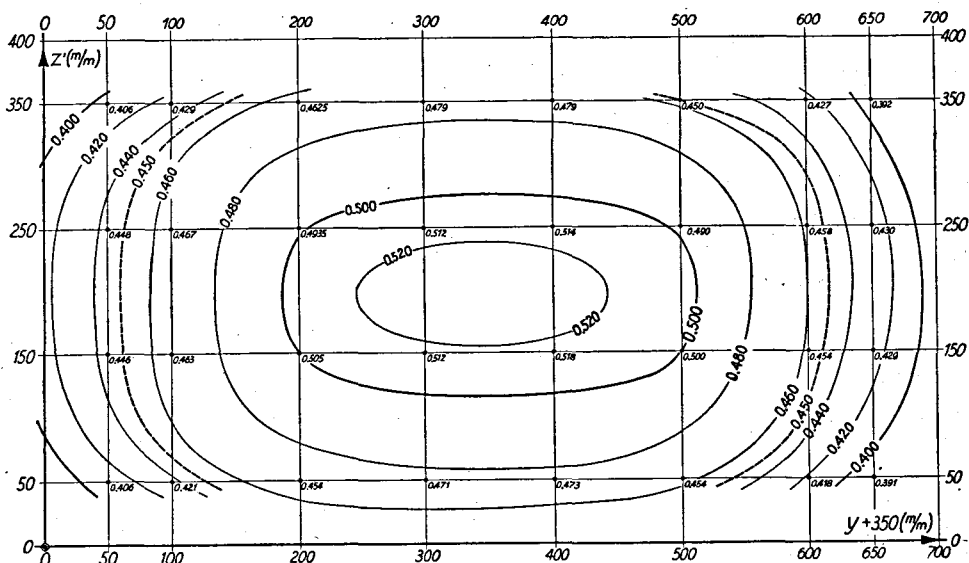


Figure 26: Static Pressure Distribution in Approach Section at $X=1160$ mm (Contraction Nozzle Throat)

Contours of Constant $\frac{P_s}{q_1}$ Are Given; $q_1 = 48$ mm H₂O. Small Figures Give Values Measured at Points (•)

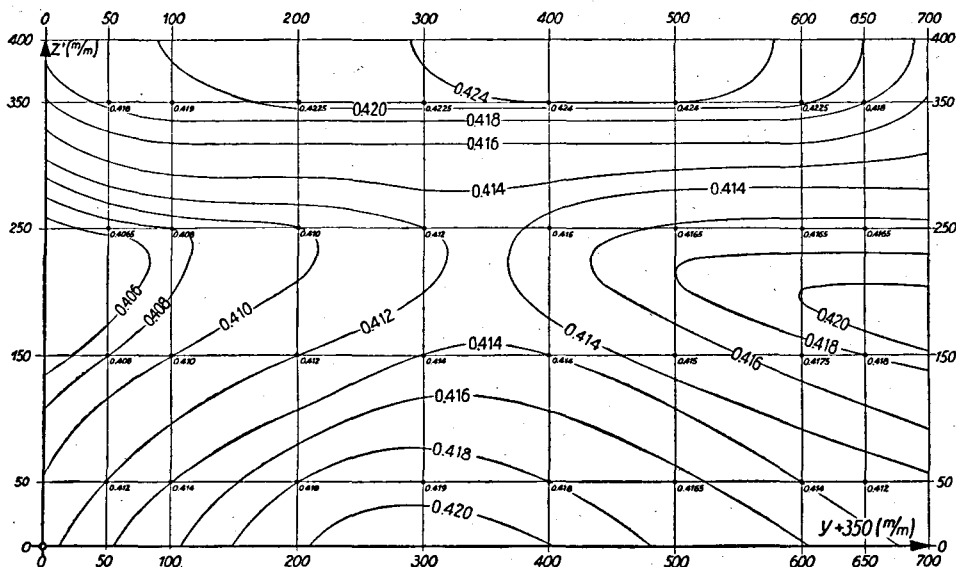


Figure 27: Static Pressure Distribution in Approach Section at $X=660$ mm

Contours of Constant $\frac{P_s}{q_1}$ Are Given; $q_1 = 48$ mm H₂O. Small Figures Give Values Measured at Points (•)

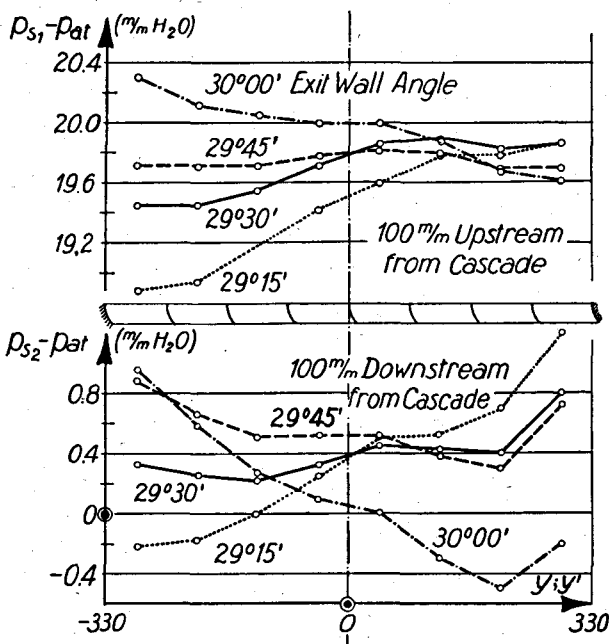


Figure 28: Static Pressure Across Tunnel for Various Angles of Parallel Exit Walls
 $x(x') = 100 \text{ mm}$; $q_1 = 49.5 \text{ mm H}_2\text{O}$

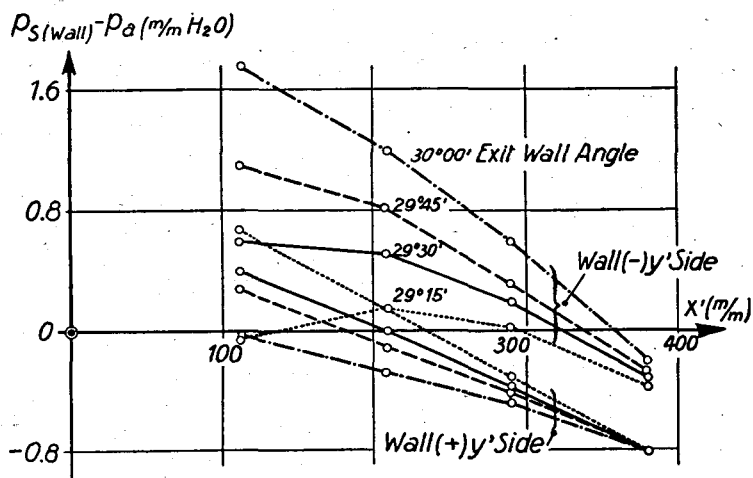


Figure 29: Static Pressure Distribution on Exit Walls for Various Angles of Parallel Exit Walls
 $z = 180 \text{ mm}$; $q_1 = 49.5 \text{ mm H}_2\text{O}$

The pressure field prevailing in the cascade test section itself was then subject to disturbances from: a) the boundary-layer take-off slots; b) the mixing zone at outlet where the tunnel flow was discharged into still air, and; c) the position of the exit walls. It was possible to attain parallel flow past the take-off slots, as indicated by wall static-pressure taps located just ahead of and behind the slot edges, by throttling the slot discharge outlets. (Any disturbance arising from improper slot adjustment was found to be very local in nature, reflected mainly in unwanted boundary-layer growth.) The effect of the outlet mixing zone was minimized by making the outlet walls more than three blade chords in length.

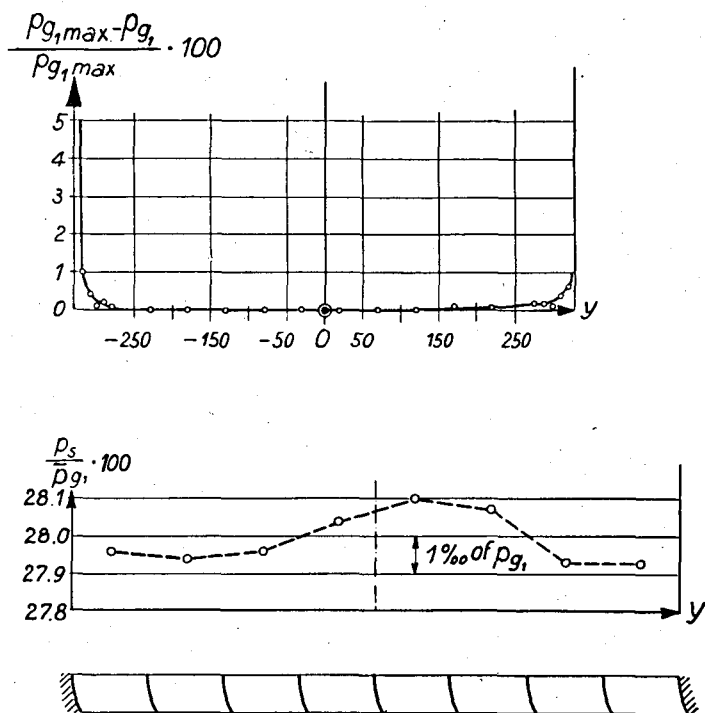


Figure 30: Total and Static Pressure Distributions Across Tunnel Upstream from Cascade; Final (Test) Condition

$$x = 100 \text{ mm}; z = 180 \text{ mm}; P_{g1,max} = \bar{P}_{g1} = 70.53 \text{ mm H}_2\text{O}$$

The possible disturbance of the cascade pressure field by the exit walls was eliminated by making the achievement of a uniform pressure field the requirement for their proper positioning. For the condition of normal tunnel turbulence and $Re = 22.8 \cdot 10^4$, three indications were investigated in connection with the exit-wall position: (1) Uniformity of cascade pressure field; (2) Uniformity of static pressure distribution along the exit walls themselves, and; (3) Correlation between the outlet air angle approximately $1/4$ chord-length behind the cascade with exit wall angle. Figure 28, plotted to large scale, shows the variation of pressure ahead of and behind the cascade for

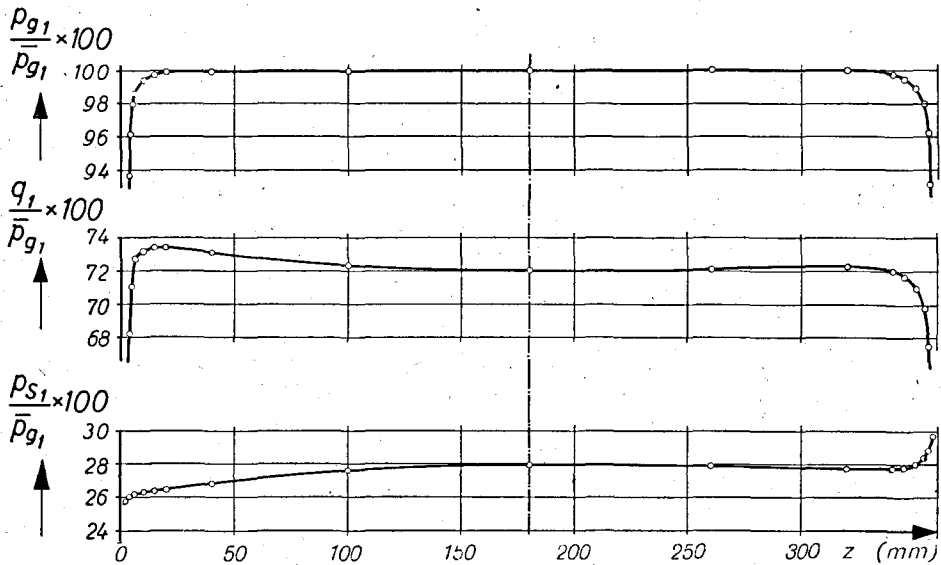


Figure 31 A): Total, Static, and Dynamic Pressure Distributions Over Tunnel Height Upstream from Cascade

$$x = 100 \text{ mm}; y = \pm t/2; \bar{P}_{g1} = 74.09 \text{ mm H}_2\text{O}$$

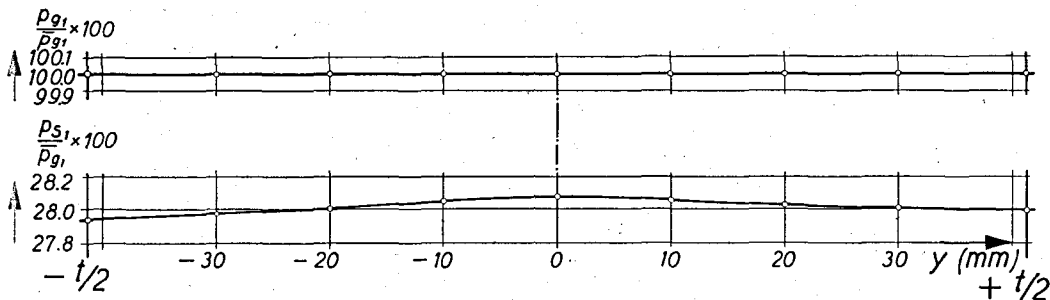


Figure 31 B): Total and Static Pressure Distributions Across Center Blade Upstream from Cascade

$$x = 100 \text{ mm}; z = 180 \text{ mm}; \bar{P}_{g1} = 74.09 \text{ mm H}_2\text{O}$$

various angles of exit walls. Figure 29 shows the variation of static pressure on the exit walls themselves for various exit wall angles. Walls were parallel at all times. Table III (page 47) shows the correlation of reference outlet air angle β' (measured at a point with coordinates $x' = 40$; $y' = 27$; $z = 180$) with exit wall angle. Air and exit wall angles are specified in relation to the axis of the the parallel-walled approach section. Coordinate systems are defined in Figure 19.

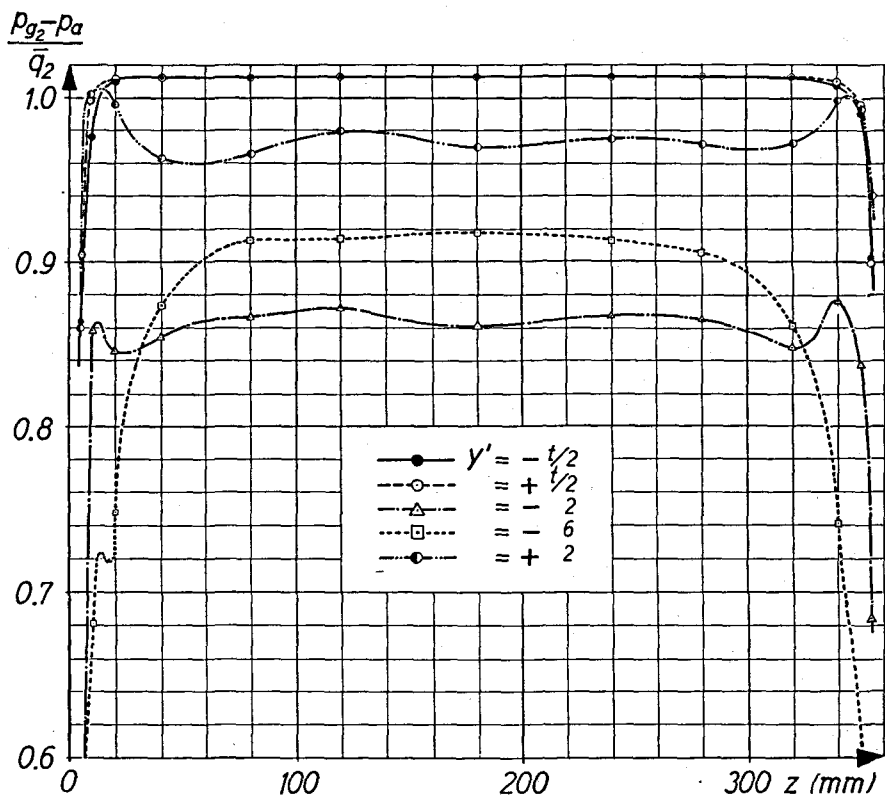


Fig. 32 A

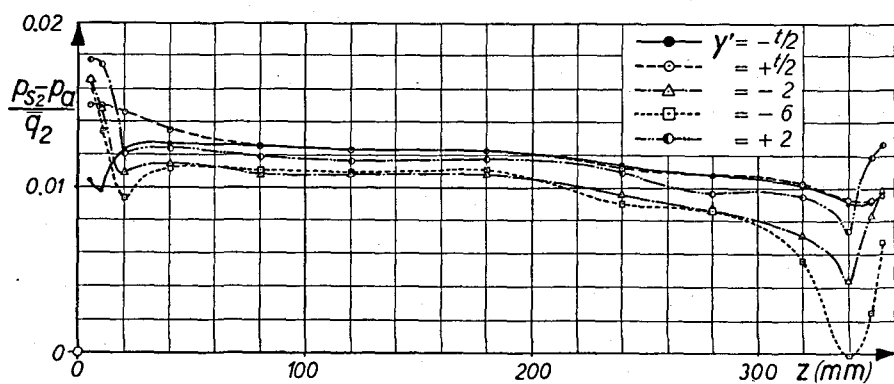


Fig. 32 B

Figure 32: (A) Total, and (B) Static Pressure Distributions Over Tunnel Height Downstream from Center Blade

$x' = 100 \text{ mm}$; $\bar{q}_2 = 73.1 \text{ mm H}_2\text{O}$

Table III. Variation of Reference Outlet Air Angle With Exit Wall Angle

($Re = 22.8 \times 10^4$)

Wall Angle:	28°50'	29°15'	29°20'	29°50'	30°20'
Air Angle, β' :	29°21'	29°24'	29°27'	29°27'	29°33'

For all subsequent investigations, except as noted below, the exit walls were fixed at an angle of $29^\circ 35'$ with the tunnel axis. The pressure fields resulting are shown in Figures 30, 31, and 32. It is seen that total pressure is constant within the limits of measurement accuracy (± 0.01 mm H_2O) over the greater part of inlet area, while static pressure at inlet across the tunnel is constant within the same limit. Dynamic pressure is constant within ± 0.5 mm H_2O (0.7 % of P_{g1}) over the tunnel height at inlet ahead of the center blade, a satisfactory yet lesser degree of constancy which was accepted since it did not materially affect the two-dimensional flow in horizontal planes. Pressures behind the cascade naturally reflect the strong effects of wake and "end" losses.

The blade dynamic forces as determined by balance measurements were found to be especially sensitive to exit wall position. For these measurements, the criterion for correct exit wall position was the maintenance of a uniform cascade pressure field, which is the first of the three criteria discussed in a preceding paragraph. Procedures followed are outlined in Section V. C. 2, "Balance Measurements".

IV. E. Force on Sealing Plate and Blade Base Exterior to Tunnel

The center blade of the cascade was mounted as a vertical cantilever beneath the test section, passing through the lower tunnel wall without contact, and terminating just beneath the upper tunnel wall. Preliminary tests showed a much lesser disturbance of the pressure distribution about the blade when the small clearance space between blade and lower tunnel wall, necessary for weighing, was placed at a distance from the blade itself by means of a roughly circular flat plate fastened to the blade perpendicular to its axis. The upper side of the plate lay flush with the inner bottom wall of the test section. For evaluation of the later balance measurements, it was nec-

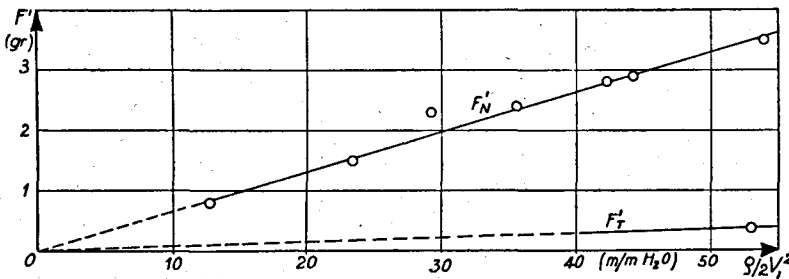


Figure 33: Dynamic Force Components Upon Center Blade Sealing Plate and Blade Mounting

F'_N = Normal to Cascade Axis. F'_T = Parallel With Cascade Axis

essary to know what part of the measured force was attributable to friction drag of the plate and to leakage flow about the blade base, etc. The plate was accordingly mounted alone in its proper position, supported by the balance and a dummy blade base. To achieve the approximate same flow conditions over the plate as in normal operation, a spare cascade blade was mounted in the position of the center blade, directly over the plate but with a very small clearance space between blade and plate to permit weighing of the drag on the latter. The components of force parallel and perpendicular to the upstream tunnel axis (F_N' and F_T') are shown in Figure 33 as functions of the dynamic pressure q_1 upstream of cascade.

V. Scope of Experimental Data; Procedure

A. General Plan

For clarity and comparison, the subject matter of the investigation is separated into two general categories, namely; two- and three-dimensional phenomena. Two-dimensional phenomena are in general associated with the plane of flow at mid-height of cascade. The flow variables upon which interest was focussed were Reynolds number and stream turbulence. To permit use of a convenient parameter for specifying relative Reynolds number a reference value Re^* was defined equal to one-quarter of the maximum Reynolds number used;

$$Re^* \equiv 5.70 \times 10^4 = \frac{\text{Blade chord} \times V_1^*}{\nu}$$

Reynolds numbers prevailing at test are generally expressed by the ratio $\frac{Re}{Re^*}$.

Stream turbulence is defined as previously stated by the ratio $\frac{\sqrt{u^2}}{U}$, the numerical values being derived from pressure-sphere measurements (IV. C.). In general, three conditions of turbulence intensity are compared; (1) Normal tunnel turbulence, without screens in the approach section; (2) The maximum turbulence attainable by the screens chosen, and; (3) A condition of high *local* turbulence in the critical region of the blade convex side, produced by a "spoiler" or "turbulence band" affixed to the blade, with main stream turbulence as in (1). Approximate turbulence scale or length, when given, is specified in terms of a dimensional length, L , defined in (IV. C.).

Reference pressures used were measured by Prandtl tubes at points ahead of and behind the cascade having the coordinates ($x = 86$; $y = 280$; $z = 75$) and ($x' = 165$; $y' = 290$; $z = 50$) respectively, unless otherwise specified. Coordinate systems are defined in Figure 19. Air and exit-wall angles are specified in relation to the axis of the parallel-walled approach section, while directions of blade dynamic forces are related to the cascade axis.

The center blade of the cascade was the reference blade for all measurements.

The previously-mentioned "spoilers" or "turbulence bands" used to create a local turbulent zone on the convex (suction) sides of the blades consisted of strips of adhesive tape 0.6 mm thick and 2.0 mm wide extending vertically over the entire blade heights with upstream edges 70 mm forward of the blade trailing edges (see Fig. 34). The vertical edges which projected uniformly into the flow were sharp and thus quite effective in the production of turbulence. Although wires are also effective in this regard, they have the practical disadvantage of lying at slightly varying distance from the blade along their lengths due to their original local curvature, even when under tension.

V. B. Two-Dimensional Phenomena

1. Static Pressure Distribution on the Blade at Mid-height

A series of nine 0.5 mm diameter static pressure holes on the convex side of the center blade, and five on the concave side, indicated blade static pressure distribution for correlation with theory. Holes were slightly staggered vertically to avoid wakes of upstream holes. Intermediate points were measured where necessary by use of a small sonde placed parallel to and against the surface, repeated comparisons being made with the pressure indications of the taps to insure accuracy. Static pressure distribution was

determined for $\frac{Re}{Re^*} = 1, 2, 3$ and 4 with $\frac{\sqrt{u^2}}{U} = 1\%$; $\frac{Re}{Re^*} = 1, 4$ with $\frac{\sqrt{u^2}}{U} = 3.4\%$; and $Re/Re^* = 1, 2, 3$ and 4 with $\frac{\sqrt{u^2}}{U} = 1\%$ — local turbulence bands

on all blades. All readings were accurately reproducible. Concurrently, the location of the point of transition of boundary layer from laminar to turbulent was determined by stethoscope and small total-pressure tube [37]. The stethoscope indications yielded a zone (rather than "point") of transition, at the upstream boundary of which the first *intermittent* rumbling sounds characteristic of turbulence were heard, while at the downstream boundary the rumbling was continuous. The point taken as the "point of transition" was the upstream boundary of this zone.

2. Change in Reference Cascade Pressure Drop and Turning Angle with Reynolds Number and Turbulence

For clarification of blade performance under varying conditions of Reynolds number and turbulence intensity, an indication of the change in pressure drop through the cascade and of change in turning angle (turning angle $= \beta_2$ since $\beta_1 = 0$) was determined for plane $z = 180$ by taking a reference difference in static pressures, ΔP_s^* , measured by two fixed sondes located at $(x = 100; y = -2.5t; z = 180)$ and $(x' = 60; y' = -t/2; z = 180)$ and measuring a reference outlet angle β_2^* by directional head at $(x' = 60; y' = -t/2; z = 180)$. In the *relative* sense, these simple measurements may be considered to closely approximate the corresponding quantities derived by integration of detailed measurements across the blade spacing, t .

3. Total-Pressure Wake Traverses at Blade Mid-height

Since the presence of a highly-turbulent, low-velocity zone, or "wake", behind a cascade blade is indicative of a departure from ideal, loss-free flow, the extent of this wake is a measure of blade loss, analagous to the "profile drag" of single airfoils. Accordingly, total-pressure measurements were carried out at a short distance (20 mm) behind the center blade in the plane $z=180$ for the complete range of Reynolds number and turbulence conditions encompassed in this investigation. The measured points extended over one complete blade spacing, from $y=-t/2$ to $+t/2$, intervals being 1 mm or less within the wake as required for its proper definition.

4. Flow at Blade Surface

The occurrence of transition of the boundary layer from laminar to turbulent, or its separation from the blade surface, may be made visible by a well known device. The convex (suction) sides of two of the central blades were coated, in the critical region for transition or separation, with a mixture of kerosene, lubricating oil and lampblack, after which the air velocity was maintained constant at the desired value until the surface flow pattern had established itself visibly in the coating. Since the blades were vertically positioned, drainage took place downward along the blade axis, and chord-wise displacement of the lampblack particles was due to air flow alone. Not only did drainage prevent the local accumulation of a too-thick coating, but combined with the effect of air viscosity, it produced in certain low-velocity regions slanted lines which indicated by their upstream or downstream slope the *direction* of the flow at the blade surface. The flow patterns were recorded photographically, with a millimeter scale affixed for reference after patterns had formed.

V. C. Three-Dimensional Phenomena

1. Wall Static Pressure Field

As mentioned in Section IV. B., weighing of forces on the reference blade required a small clearance space between the upper end of this blade and the upper tunnel wall. The numerous static pressure taps in this region of the tunnel wall permitted determination of the static pressure field. To obtain some indication of the extent to which the tip clearance distorted the flow during the weighing process, the static pressure field was measured first with the normal tip clearance of 0.15 mm and then with the clearance space closed (blade extended to wall). Comparison of pressure distribution about the blade end (without clearance space) with that measured about the blade mid-height also indicates the effect of the wall boundary layer.

2. Balance Measurements

Accurate force measurements constitute by all means the simplest, and in some respects the most accurate, means of evaluating cascade performance. The ease with which cascade efficiency may be defined in terms of force

components is indicated in Section VI. B. 2. One of the chief obstacles in way of general employment of a force balance is the requirement of very high accuracy in determining forces of greatly different relative magnitudes. The balance especially constructed for this investigation satisfies this requirement. Tip and end losses are included in efficiency determinations from force measurements.

The actual weighing process consisted of first determining the direction of the resultant force on the blade and sealing structure within five one-hundredths of a degree by finding that direction in which the force component was equal to zero. The resultant of blade and sealing-structure forces was then measured 90° from this "null" direction. Since the force exerted upon the sealing structure was approximately two one-thousandths of the blade force (see IV. E.), and acted in a direction very nearly perpendicular to the blade force, no correction to the *magnitude* of the actual net blade force was required [$\cos(\sin^{-1} 0.002) = 1.00000$]. The correction to the *direction* of the resultant force on blade alone amounted to approximately one-tenth degree ($\sin^{-1} 0.002 = 0^\circ.10$). Reliable measurements were carried out with tunnel dynamic pressures, q_1 , as low as one millimeter of water column.

Since static-force calibration tests upon the balance had shown an accuracy of approximately $1/10$ percent, while the pressure in the settling chamber of the tunnel varied as much as $1/2$ percent, utilization of the full capabilities of the balance required the focussing of attention upon the latter. A weight was placed upon the pan of the balance and the compressor speed then adjusted by a supplementary slide-wire rheostat (IV. A.) to bring the balance into equilibrium. With full attention of the operator given to the micromanometer upon which reference inlet dynamic pressure to the cascade was indicated, simultaneously controlling the rheostat, it was possible to obtain the proper inlet dynamic pressure reading to the same degree of accuracy as that inherent in the balance. Repeated determinations were made and showed excellent reproducibility.

As noted in IV. D, the requirement of extreme accuracy in the balance measurements required exactly correct positioning of the exit walls as defined by a uniform pressure field in the cascade. It was noted that after so positioning the exit walls at a particular value of Reynolds number and turbulence, exact duplication of the pressure field might not be attained at other conditions of flow due to a slight variation in turning angle with Reynolds number and turbulence, as previously mentioned in V. B. 2. These variations were slight and were considered only in connection with balance measurements. To obviate the necessity for repeated changes in exit wall position during subsequent runs, use was made of a procedure developed and experimentally verified at the Institute independently of this investigation. This involved fixing of the walls at an angle correct for one (high) Reynolds number, and then making measurements over the *entire range* of Re with walls in that position and correcting the measured results for the slight imposed restraint. It was merely necessary to make a series of force measurements at constant Re and turbulence, but with wall angle varied slightly on either side of the correct position, to determine the change in blade force components resulting from a known small error in exit wall angle (restraint of flow). The momentum law yielded directly the change in force

component which resulted from an equal small change in turning angle without flow restraint by the walls. Comparison of the two showed what proportion of force component variation was due to each factor (change in turning angle; or error in exit wall angle) when Reynolds number was varied from that value for which the walls were correctly positioned in a test series. For the present investigation, the "real" part of the change in tangential force coefficient $\left(\frac{F_T}{A_b \cdot q_1}\right)$ was found to amount to about 53 % of the measured change, the change being with reference to the value of the coefficient at the operating condition for which the exit walls were correctly positioned.

It was also found that the wall interference created a variation in normal force component equal to about 3 % of the required tangential force component correction. Exact corrections were made to measured tangential-, normal-, and total-force coefficients and to the corresponding measured values of θ (direction of resultant force).

3. Momentum Traverses Over Blade Height

A three-dimensional evaluation of the momentum equations for the air stream associated with the reference blade was carried out in order to check the force balance indications and to gain a detailed knowledge of flow conditions, especially with regard to wall influences.

For cascade inlet angle $(\beta_1) = 0$, the momentum equations may be written;

$$F_N = 2 \int_0^z \int_{-t/2}^{t/2} (q_1 - q_2 \cos^2 \beta_2) dy dz + \int_0^z \int_{-t/2}^{t/2} (P_{s1} - P_{s2}) dy dz \quad (1)$$

$$F_T = \int_0^z \int_{-t/2}^{t/2} q_2 \sin(2\beta_2) dy dz \quad (2)$$

The continuity equation, which may be used to check the accuracy of measurement of quantities P_{s1} , P_{s2} , P_{g1} , P_{g2} , and β_2 , may be written, for assumed incompressible flow:

$$\int_0^z \int_{-t/2}^{t/2} \sqrt{q_1} dy dz = \int_0^z \int_{-t/2}^{t/2} \sqrt{q_2} \cos \beta_2 dy dz \quad (3)$$

The reference planes corresponding to subscripts (1) and (2) were $x = 100$ and $x' = 100$ respectively. The aforementioned measured quantities were determined between y (y') $= -t/2$ and $+t/2$ for the 13 planes $z = 5, 10, 20, 40, 80, 120, 180, 240, 280, 320, 340, 350$, and 355 . Measurements were taken at 2 mm intervals in the wakes, and at greater intervals where variations were slight. Traverses were made at constant z by usual-type sondes, and then correlated with vertical traverses at constant y made with the special sonde having the property of equal flow obstruction all heights (III. D.) in order to correct the former for minor inaccuracies arising from their insertion to different distances into the stream.

The continuity equation was tested, and measurement accuracy confirmed, by a procedure similar to the momentum-equation evaluation. For the 13 z -planes, curves were plotted of $(\sqrt{q_2} \cdot \cos \beta_2 - \sqrt{q_1})$, integrated over y and z , and multiplied by $\sqrt{\frac{2}{\rho}}$ to give the error, ΔQ . The quantity $\frac{\Delta Q}{Q_1}$ was found equal to $+0.004$, or an error of 0.4 percent.

The measurements for evaluation of the momentum equations were carried out with normal tip clearance existing at the blade upper end in order to permit valid comparison with balance measurements (VI. B. 2). No turbulence screens were placed in the cascade approach section ($\frac{\sqrt{u'^2}}{U} = 1\%$)

VI. Discussion of Data: Comparison with Theory

A. Two-Dimensional

1. Static Pressure Distribution About Blade at Mid-height

Blade static pressure distributions as determined by the continuum-cascade theory and by experiment are shown in Figure 34. (The local inflections in the suction-side pressure curves of part (C) of this figure at $\eta_H = 0.45$ are due to the presence of the turbulence band located just downstream of the pressure tap at that point.)

Comparing first the theoretical and experimental pressure-distribution curves, remarkably close agreement is noted on the critical (suction) side of the blade and fair agreement on the pressure side. It will be recalled that the theoretical pressures were computed from velocities obtained by adding to (for the suction side) or subtracting from (for the pressure side) the computed camber-line velocity a component attributed to the circulation for the particular blade element (II. A.). This simple distribution of the circulation velocities is known to be inexact, and is particularly questionable where the blade has appreciable thickness. (It will be noted that toward the trailing edge, where the blade is thinnest, the agreement is best.) Further study will be required to determine how the circulation-velocity components may be more correctly proportioned between suction and pressure sides of the blade. Since the experimental curves derive from a real fluid, while the theoretical curve derives from assumption of a non-viscous, loss-free fluid, it is proper that the area within the experimental pressure-distribution curve should be less than within the theoretical curve. The discrepancy in pressures may be thought of as due only *in part* to the lesser circulation of the actual blade. (Experience with single airfoils has shown that a slight increase in experimental angle of attack serves to equalize the circulations and give improved correlation with theory.)

Despite the difference in "pressure-side" pressure distribution, the theoretically-designed blade produced a mean turning angle of 29.5° as com-

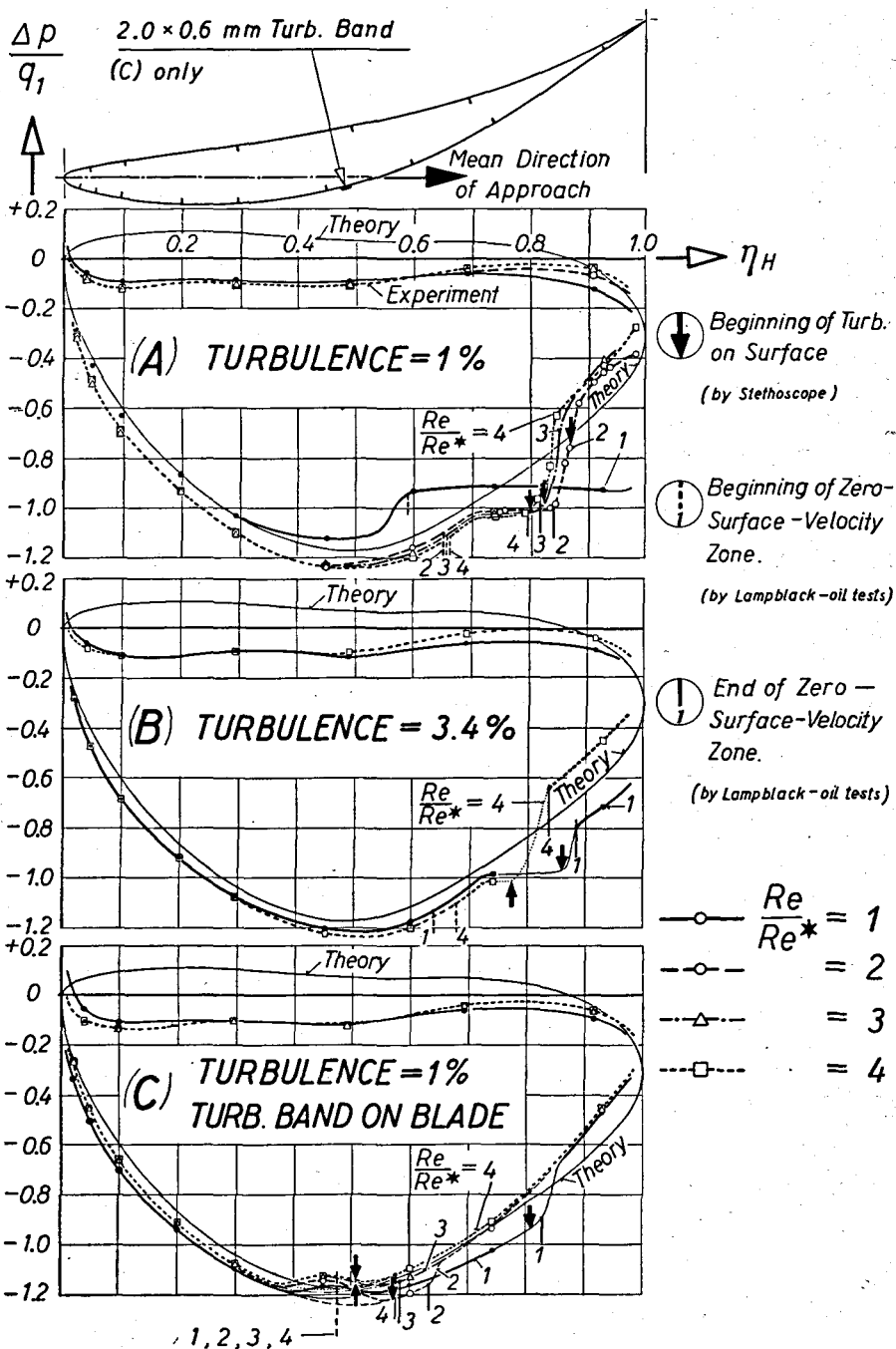


Figure 34: Theoretical and Experimental Pressure Distributions at Blade Mid-height
 $\Delta p = P_s - P_{s1}$; $Re^* = 5.7 \times 10^4$

pared with the desired 30° — a difference of only 1.7 %. Table IV compares the force components derived theoretically (for 30° turning angle) and experimentally for the condition $Re/Re^* = 4$; $\frac{\sqrt{u^2}}{U} = 1\%$. It is noted that the

force components measured for the actual blade agree very well with those theoretically required for a 30° outlet angle. The conclusion which may be drawn is that the continuum theory yields a blade form which produces to a very good approximation the force components and hence turning angle required of it, and yields a good, but somewhat less accurate, overall approximation of pressure distribution, the diminished accuracy in the latter respect being largely attributable to the over-simplification in the last stage of the pressure-determination process.

The experimental curves for the suction side reflect in an interesting manner the separate influences of turbulence and of Reynolds number. For the condition $\frac{Re}{Re^*} = 1$; $\frac{\sqrt{u^2}}{U} = 1\%$ [Figure 34 (A)], permanent separation of

the flow from the blade is indicated, while in all other cases shown, separation, if it occurs at all, is temporary. The effectiveness of increased Reynolds number and of increased turbulence in eliminating this permanent separation are evident from (A) and from (B) and (C) respectively.

The zone of temporary separation which is evidenced by flat pressure distribution in the neighborhood of $\eta_H = 0.8$ will be treated in more detail in connection with the direct visual evidence of the surface flow in Section VI. A. 3. Suffice it to note at this point that the *local* turbulence of Figure 34 (C) is clearly more effective in suppressing this local separation than the *general* flow turbulence of (B). Subsequent sections (VI. A. 3 and VI. B. 2) will indicate the relative blade losses associated with each type of turbulence and permit a valid comparison of their relative merits.

Table IV. Comparison of Theoretical and Experimental Blade Forces

	$\frac{F_N}{e/2 \cdot C_1^2 \cdot a_b}$	$\frac{F_T}{e/2 \cdot C_1^2 \cdot a_b}$	$\frac{R}{e/2 \cdot C_1^2 \cdot a_b}$
From Velocity Triangle			
Desired (Euler Equation)	0.229	0.794	0.826
Momentum-equation			
Transverse at $z = 180$	0.223	0.796	0.818
Integrated Experimental			
Pressure Distribution	0.222	0.797	0.827
Integrated Theoretical			
Pressure Distribution	0.256	0.897	0.933
Momentum-equation Transverse			
over Entire Blade Height	0.236	0.779	0.814
Balance Measurements	0.236	0.782	0.816

$F; R$ = Force per meter blade length

a_b = Projected blade area (upon chord) per meter blade length

N = Normal to cascade axis

T = In direction of cascade axis

R = Resultant blade force.

2. Blade Losses from Wake Traverses

A simple and rational method of comparing the losses of the mid-stream portion of a blade under varying conditions of flow follows from the total-pressure measurements in the wake. Figure 35 gives the results of measurements carried out as described in (V.B.3). (A), (B) and (C) of this figure taken individually serve to indicate the effect of Reynolds number, and when compared with one another, indicate turbulence effect. (D) shows turbulence effect at the lowest value of Reynolds number, where the danger of separation is critical as indicated by Figure 34. In addition to showing turbulence *intensity* effects, (D) includes a family of three curves for which the value of turbulence *intensity* is virtually *constant*, while the turbulence *scale* (L) varies from 2.1 to 5.9 mm.

Although in general the blade loss varies with the area under the wake curve for wakes of similar shape, the dissimilarity of wake shapes shown in (A) and (D) required a more exact means of comparison.

Consider the system shown in Figure 36. Fluid is assumed incompressible. We define as "loss" of the real cascade that energy which, between (0) and (3), has been expended to raise the temperature of the fluid, and is thus unavailable for performance of mechanical work. Since both cascades are considered stationary, no work is delivered by the fluid within the control surface, $ABDC$. The energy loss per second of the system is then,

$$E_L \equiv \int g_0 \cdot W_0 \cdot \cos \Phi \cdot dy - \int g_3 \cdot W_3 \cdot \cos \Phi \cdot dy$$

$$E_L = W_3 \cdot \cos \Phi \int (g_0 - g_3) dy.$$

Since $g = P + \rho W^2/2$; and also $W_0 = W_3$:

$$E_L = W_3 \cdot \cos \Phi \int (P_0 - P_3) dy \quad (1)$$

Momentum equation between planes (0) and (1):

$$\frac{F'_x}{\cos \Phi} = \int P_0 dy - \int P_1 dy + \rho \int W_0^2 dy - \rho \int W_1^2 dy \quad (2)$$

Momentum equation between (1) and (2):

$$\frac{F_x}{\cos \Phi} = \int P_1 \cdot dy - \int P_2 \cdot dy + \rho \int W_1^2 dy - \rho \int W_2^2 dy \quad (3)$$

Adding equations (2) and (3):

$$\frac{F'_x + F_x}{\cos \Phi} = \int P_0 dy - \int P_2 dy + \rho \int W_0^2 dy - \rho \int W_2^2 dy$$

$$= \int (P_0 - P_2) dy + \rho \int (W_0^2 - W_2^2) dy$$

$$\frac{F'_x + F_x}{\cos \Phi} = \int (g_0 - g_2) dy - \rho/2 \int (W_2^2 - W_0^2) dy \quad (4)$$

Momentum equation between (1) and (3):

$$\frac{F_x}{\cos \Phi} = \int P_1 dy - \int P_3 dy + \rho \int W_1^2 dy - \rho \int W_3^2 \cdot dy \quad (5)$$

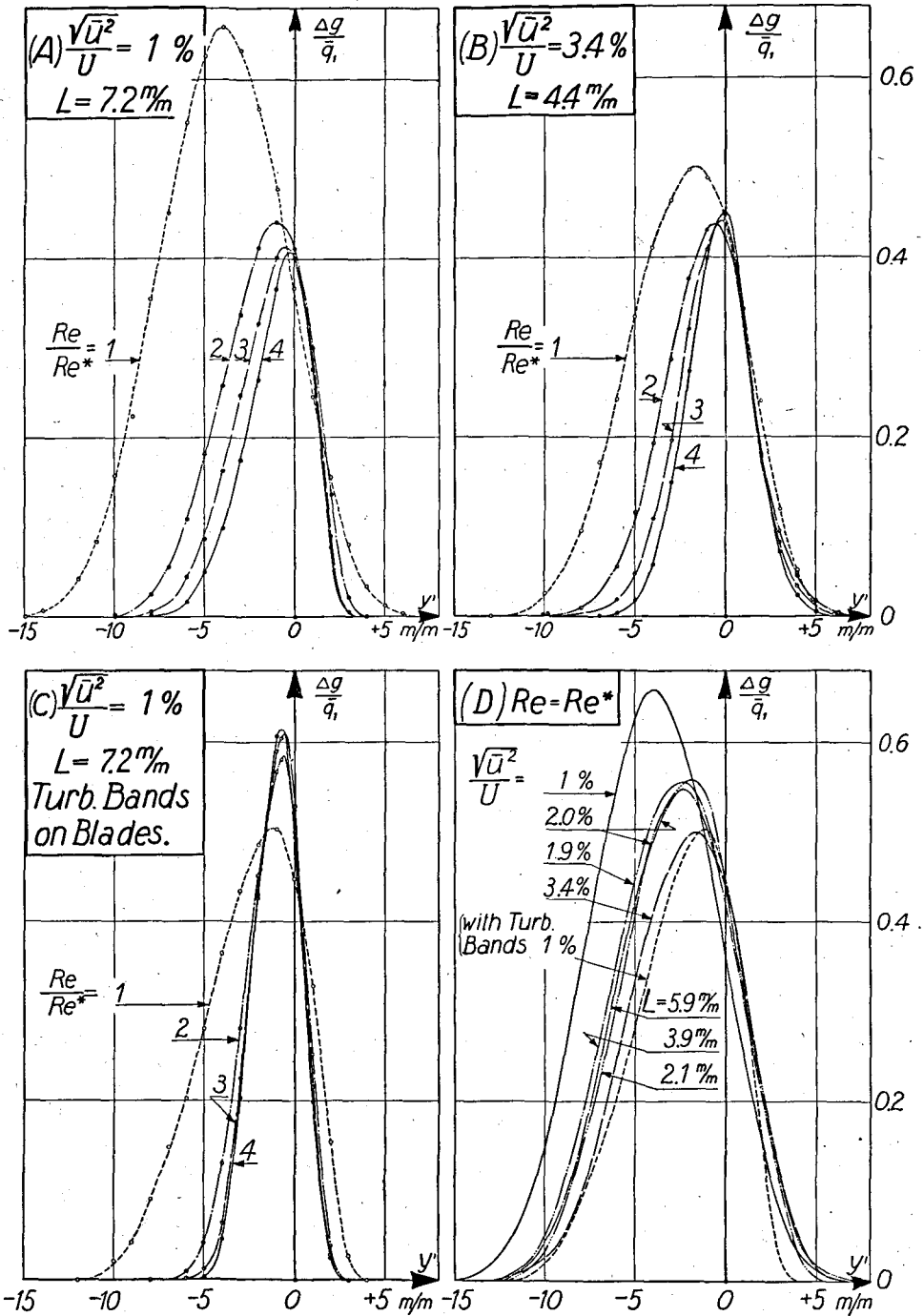


Figure 35: Blade Total Pressure Wakes
 $x' = 20 \text{ mm}$; $z = 180 \text{ mm}$; $Re^* = 5.7 \times 10^4$

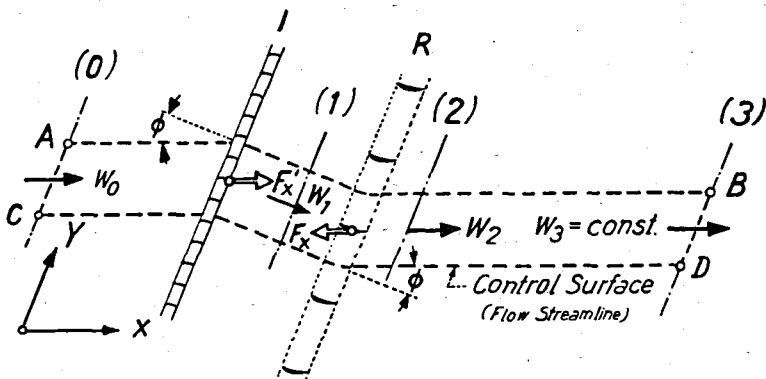


Figure 36: System For Derivation of Blade Loss in a Stationary Cascade
 I = Ideal, Loss-free Cascade. R = Real Cascade. Control Surface $ABDC$ Consists of Two Stream Lines and Two Planes Parallel to Cascade Axis

Adding equations (2) and (5):

$$\frac{F'_x + F_x}{\cos \Phi} = \int P_0 dy - \int P_3 dy + \rho \int W_0^2 dy - \rho \int W_3^2 dy$$

and, since $W_0 = W_3 = \text{constant}$;

$$\frac{F'_x + F_x}{\cos \Phi} = \int (P_0 - P_3) dy \quad (6)$$

From (4) and (6):

$$\int (P_0 - P_3) dy = \int (g_0 - g_2) dy - \rho/2 \int (W_2^2 - W_0^2) dy \quad (7)$$

Substituting (7) in (1):

$$E_L = W_3 \cdot \cos \Phi \left[\int (g_0 - g_2) dy - \rho/2 \int (W_2^2 - W_0^2) dy \right] \quad (8)$$

From the continuity equation;

$$W_1 = W_3 \cdot \cos \Phi = W_0 \cdot \cos \Phi \quad (9)$$

From (8) and (9):

$$E_L = W_1 \left[\int (g_0 - g_2) dy - \rho/2 \int (W_2^2 - W_0^2) dy \right] \equiv W_1 \cdot D' \quad (10)$$

We remember that for our system, cascade I was defined as loss-free. Hence equation (10) expresses the losses of the *real cascade alone*. We see that a real cascade suffers an energy loss (i. e., energy no longer available for performance of mechanical work) which is proportional to D' for W_1 constant. We further note that the expression for D' in (10) is identical to the equation for the drag of the cascade without circulation, (i. e., zero turning angle), for which case *Keller* [20] has indicated a simple method for evaluating D' from wake measurements alone. Since $W_0 = \frac{W_1}{\cos \Theta}$, and $g_0 = g_1$, we may evaluate D' under various flow conditions with W_1

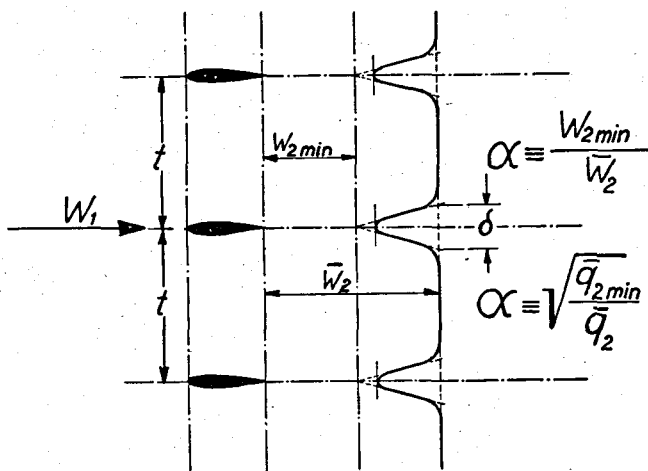
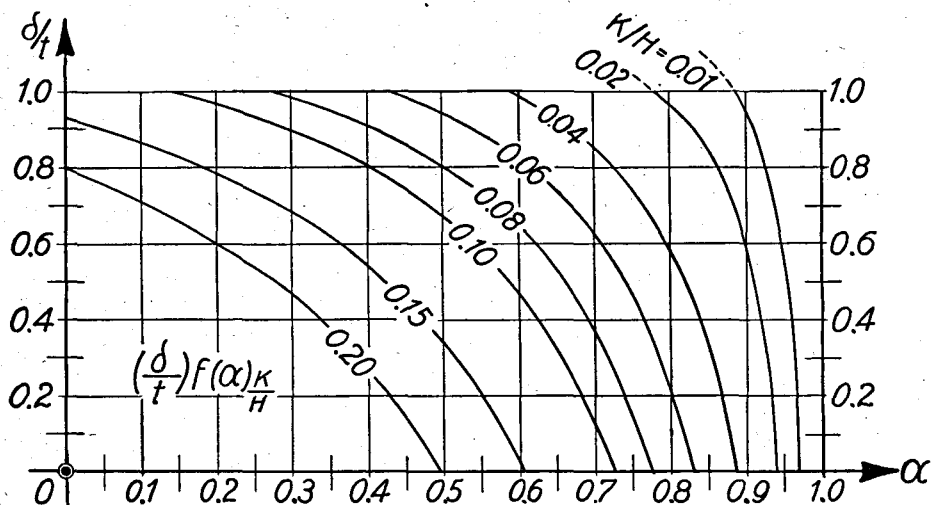


Figure 37: Chart for Determination of K/H From α and $\frac{\delta}{t}$, for Use in Equation

$$D = \int \Delta g \, dy - \rho/2 \int (W_2^2 - W_1^2) \, dy \equiv H - K,$$

Assuming Triangular Distribution of Wake Velocity

constant and thus very simply obtain a direct measure of relative blade losses.

Analogous to the profile drag of an aircraft wing, the drag experienced by a blade of a cascade so positioned as to give zero lift (Figure 37) is given by,

$$D = \int \Delta g \cdot dy - \rho/2 \int (W_2^2 - W_1^2) \, dy \equiv H - K,$$

wherein the first integral is proportional to the area under the wake curve defined by total-pressure measurements, and the second integral is usually less than ten percent of the first. If the downstream static pressure is negligibly small in comparison with the total pressure (about one percent for the present case), the total-pressure traverse serves to define the downstream velocity distribution, and is the *only traverse required*.

Keller [20] has shown that assumptions of simple geometric forms for the velocity wakes lead to easy and satisfactorily accurate evaluation of the ratio K/H for solution of the foregoing drag equation, and hence for the solution of equation (10) which is of identical form. Using one of the velocity-wake shapes treated by Keller — namely, that of a triangle — the curves given in Figure 37 were plotted for use in evaluation of D' . From D' , a_b (projected blade area for unit height), and q_1 (the actual inlet dynamic pressure), a dimensionless "loss factor" was defined:

$$\text{Loss Factor} = \frac{D'}{a_b \cdot q_1}.$$

Table V indicates the evaluation of the loss factor. The single case of flow separation already noted from the static pressure distribution curves (Figure 34) is immediately noticeable by its high relative loss factor. The decrease of loss factor with increase in Reynolds number is apparent throughout.

The clearly-evident beneficial effect of increased turbulence at low Reynolds number only is due to the effectiveness of turbulence in the suppression of flow separation, both temporary and permanent.

Conversely, it is noted that the effect of high turbulence intensity (both local and general) at the *maximum* Reynolds number is detrimental, as substantiated by later blade-efficiency determinations from balance measurements (VI. B. 2). The most general explanation of the superior performance of the blade for the condition of least turbulence lies in the *later* transition of its boundary layer to turbulence, thus subjecting a *lesser* part of the blade surface to the higher frictional drag of a turbulent boundary layer than in the cases of increased turbulence.

Due to the small differences between relative loss factors, a full appreciation of their significance requires mention of the fact that the wakes were plotted from total-pressure measurements which were *not* corrected for turbulence.

The relative loss factors for the three cases of approximately equal turbulence intensity all fall within a zone commensurate with the degree of uncertainty in the determination of the individual intensities, so that the only conclusion which may safely be drawn regarding turbulence scale effect is that scale is of relatively minor importance in relation to intensity. This latter fact is well known from the work of Dryden (Section IV: C.) and others.

The relative indifference of the pressure side of the blade to the complete range of flow variations is indicated by the very small relative changes in the right-hand sides of the wake curves of Figure 35.

Table V. Blade Loss From Wake Total-Pressure Traverse

Turbulence of Incident Flow		Blade Reynolds Number		Wake Area	(From Figure 3)			Loss Factor	
$\frac{\sqrt{u'^2}}{U}$; %	L; (mm)	$Re \cdot 10^{-4}$	$\frac{Re}{Re^*}$		α	$\left(\frac{\delta}{t}\right)$	$1 - \left(\frac{K}{H}\right)$	$\left(\frac{D'}{a_b \cdot q_1}\right) 100$	Relative
1	≈ 7.2	5.7	1	288.0	0.645	0.178	0.882	4.236	3.14
		11.4	2	134.8	0.777	0.122	0.927	2.082	1.54
		17.1	3	103.3	0.804	0.103	0.936	1.611	1.19
		22.8	4	86.4	0.810	0.088	0.937	1.349	1.00
3.4	4.4	5.7	1	199.4	0.734	0.157	0.915	3.041	2.25
		11.4	2	129.8	0.778	0.112	0.927	2.005	1.49
		17.1	3	110.2	0.784	0.095	0.928	1.705	1.26
		22.8	4	100.0	0.778	0.087	0.926	1.543	1.14
2.0	5.9	5.7	1	223.5	0.712	0.164	0.907	3.379	2.51
1.9	3.9			233.1	0.709	0.170	0.907	3.523	2.61
2.0	2.1			226.5	0.723	0.165	0.910	3.435	2.55
With Turbulence Bands Affixed to Blades									
1	≈ 7.2	5.7	1	177.0	0.734	0.139	0.913	2.693	2.00
		11.4	2	114.1	0.711	0.081	0.900	1.711	1.27
		17.1	3	104.9	0.700	0.071	0.895	1.565	1.16
		22.8	4	100.5	0.695	0.068	0.893	1.496	1.11

3. Flow at the Blade Surface

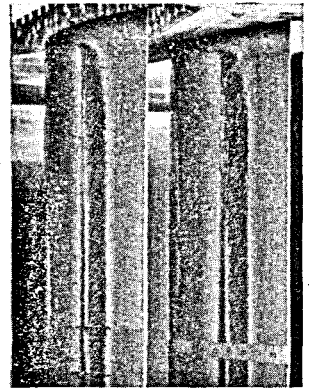
A procedure for making visible the flow at the blade surface was described in (V. B. 4). A representative series of photographic records of the lampblack patterns obtained is shown in Figure 38. Read horizontally, the photograph rows show the effect of Reynolds number; vertically, turbulence effect. For the purposes of this section, treating two-dimensional aspects of the flow, we shall consider only the strip of blade surface immediately above the millimeter reference scale located at blade mid-height. The solid black zone, especially evident in the upper left-hand photograph, represents the uniform appearance, *before* air flow was started, of the mixture applied to practically the entire blade surface. Vertical lines within the dark band are due to drainage.

The Reynolds numbers for this series of photographs ($\frac{Re}{Re^*} = 0.94; 2.24; 3.87$) were chosen not only to indicate flow conditions at low, medium and high Re , but also, in the case of the lowest Re , to corroborate the indications of the measured-force curves in regard to flow separation. Referring to Figure 43, it is seen that at $Re = 5.35 \times 10^4$: (1) The blade-force curve for 1% turbulence is falling sharply with decreasing Re , indicating flow separation; (2) The curve for 3.4% turbulence is at its peak, indicating a transition condition between flow separation and flow adherence to the blade; (3) The "turbulence-band" curve shows a stable condition of flow adherence,

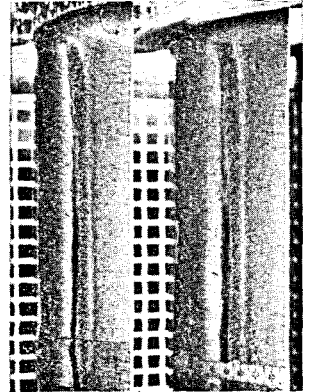
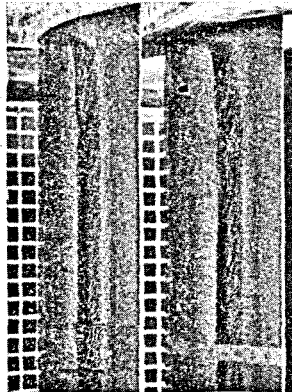
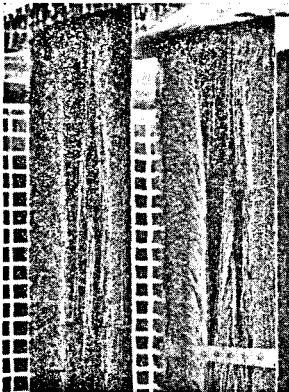
$Re \times 10^{-4} = 5.4$

12.8

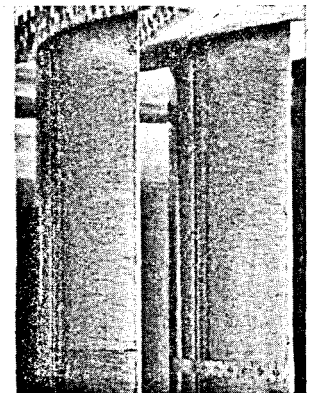
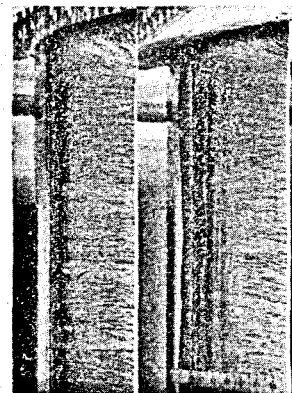
22.0



1 % Turbulence



3.4 % Turbulence



1 % Turbulence: 0.6 mm Spoilers 70 mm Forward of Blade T.E.

Figure 38: *Effect of Reynolds Number and Turbulence Upon Flow at Blade Surface*
Indication by Lampblack-oil Coating. Direction of Flow Left to Right.
Millimeter Reference Scale Located at Blade Mid-height

the peak-marking separation occurring at slightly lower Re . These conditions are all corroborated in the lefthand column of Figure 38. The slope of the lines at trailing edge in the uppermost photograph show strong reverse flow; the mottled area near the trailing edge of the center photograph shows very low-velocity flow of indifferent direction; while the lower photograph clearly shows adherent surface flow in the direction of the main stream near the trailing edge.

As conclusively demonstrated by *Schubauer* [38], the transition of the boundary layer of a convex surface from laminar to turbulent is a gradual rather than an instantaneous phenomenon. *Schubauer* observed, by the use of a similar surface coating, the same regions of virtually-zero surface velocity⁸⁾ as represented by the black areas of Figure 38, and determined the detailed flow conditions in these regions by hot-wire measurements. The upstream edge of the black zone marked the point of separation from the surface not of a purely laminar boundary layer, but of a transition-type layer with transition so incomplete that the layer continued to exhibit most of the properties of a laminar layer. Complete transition then occurred in the detached layer, which subsequently reattached itself to the surface further downstream as the turbulence developed. This explanation seems entirely valid for the present case.

Some further points deserve mention in clarifying the rather considerable breadth of the black "stagnation" or "zero-surface-velocity" zone. The theory of *Schlichting* [39], recently corroborated experimentally [40], points out that a definite time interval is required for the amplification of the proper frequencies of a disturbance (created in this case by the "laminar" separation) before completely developed turbulence is achieved. Further, both *Schubauer* and *Dryden* [41] have established experimentally that the region of maximum turbulence intensity associated with the phenomenon under discussion lies not at the blade surface but at an appreciable distance from it. Assuming general turbulence of boundary layer to begin at this point of maximum intensity, an interval will be required for turbulence to spread out to the blade surface. Experimental evidence of the latter fact was gained from stethoscope indications taken normal to the blade surface with a small total pressure tube at varying distances behind the turbulence band which was affixed to the blade for the bottom row of photographs. Immediately behind the band, a zone of high turbulence was heard at a distance from the blade corresponding to the band thickness. Further downstream, this zone had broadened but had not yet reached the surface of the blade. Finally, at the point corresponding to the downstream boundary of the black region, the turbulent zone extended all the way to the blade surface. *Jacobs* and *Dönhoff* [42] have shown that such a phenomenon takes place in the case of temporary laminar separation, the separated boundary layer proceeding in this case in the direction of the tangent to the blade surface at separation point until transition takes place at a distance from the blade surface, and then spreading out fanwise in a turbulent wedge to return to the blade surface.

⁸⁾ Although incorrect in the strict sense, "zero-surface-velocity" zone is a convenient and graphic term. It will here be defined as that zone wherein $\left(\frac{\partial V}{\partial n}\right)_{n=0} \leq 0$.

Flow on the pressure side of the blade was found to be adherent to the blade in all cases. At the highest Reynolds number ($Re/Re^* = 4$) and highest stream turbulence ($\frac{\sqrt{u^2}}{U} = 3.4\%$) tested, stethoscope observations indicated transition of the boundary layer to turbulence at a distance of about 10 mm forward of the trailing edge.

According to other authors, [42, 43], the Reynolds number based upon the breadth of the zero-velocity zone and the velocity just outside the boundary layer at the zone center has a value between 40,000 and 70,000 when the effect of stream turbulence is negligible. Evaluation of this special Reynolds number for the case of 1% turbulence gave values ranging from 45,000 to 52,000.

Zone Width (mm)	V (m/sec)	Re
21	42.0	52,300
22	34.5	47,300
30	24.2	45,300

4. Relative Variation of Cascade Pressure Drop and Turning Angle

Figure 39 shows the relative variations of reference cascade-pressure-drop, $\Delta P^*_{\text{cascade}}$, and outlet flow angle, β_2^* , as defined in Section V.B.2. That these single-point determinations may not be interpreted in the *absolute* sense as representative of conditions for the whole reference plane is apparent. They do serve, however, as a rough indication of the *relative* performance of the reference blade mid-section. Referring to Figure 44 for confirmation, it is seen that for low Re , the pressure drops for the three different turbulence conditions follow the trend of the normal components of the blade forces.

Correlation of the turning-angle (β_2^*) curves with the tangential blade-force curves of Figure 44 is conclusive. Peaks of the β_2^* curves coincide very closely with those of the corresponding blade-force curves. Since flow separation from the blade begins near the blade ends and spreads inward to the center with decreasing Re , it is to be expected that the β_2^* peaks occur at slightly lower Re than the peaks of the corresponding resultant-force curves for the entire blades, as is clearly apparent for the 1%-turbulence condition. The lesser spread between the same two peaks for the condition "with turbulence bands on blades" is to be expected in view of the predominant stabilizing effect of the high local turbulence prevailing behind the turbulence bands over the whole blade height.

The peaks in the turning-angle curves of Figure 39 give the limiting minimum Reynolds number at which the breakaway from the middle of the blade occurs under the given conditions of turbulence. Thus the blade, *when provided with turbulence band*, continues to perform well (in terms of turning the air flow) down to a minimum Reynolds number of 35,000, while the minimum permissible Re for the 1%-turbulence condition is 75,000, or more than double that for the first instance.

Even before reaching the aforementioned minimum Reynolds number the drag increases rapidly, as shown in Table V, which was computed from

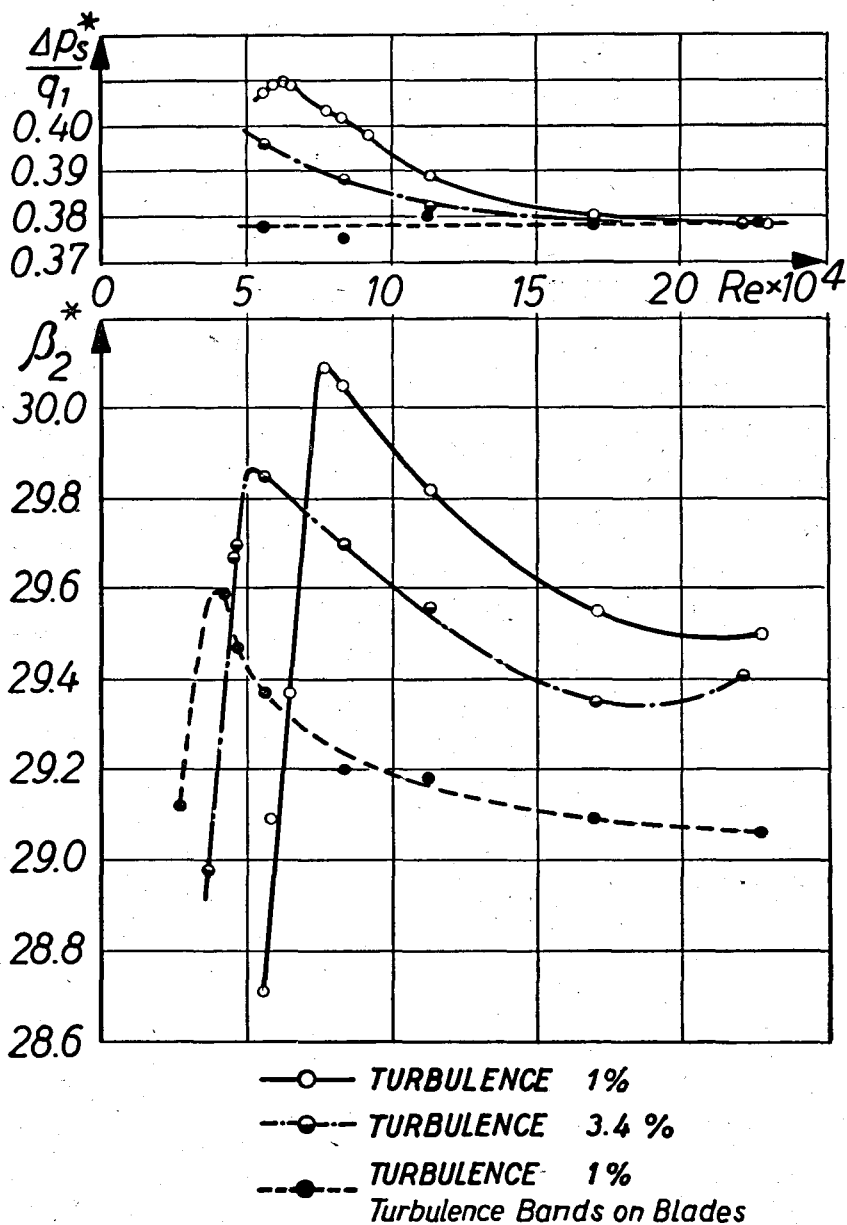


Figure 39: Reference Cascade Pressure Drop and Outlet Flow Angle as Functions of Reynolds Number and Turbulence

$\Delta P^* = P_{s_1}^* - P_{s_2}^*$. $P_{s_1}^*$ Measured at ($x = 100$ mm; $y = -2.5 t$; $z = 180$ mm)

$P_{s_2}^*$ and β_2^* Measured at ($x' = 60$ mm; $y = -t/2$; $z = 180$ mm)

total-pressure traverses at blade mid-height (Section VI. A. 2). Therefore the blade performs satisfactorily, with respect to the losses, over a still smaller range of Re -values, the lower limit of which is less clearly marked than that defined by the turning angle.

When performance of the entire blade length was subsequently determined by direct balance measurements, similar Reynolds number ranges and limiting minima resulted, as shown in Figures 43—45.

VI. B. Three-Dimensional

1. Distribution of Losses Over Blade Height; Tip Clearance Effect

Due to the viscosity of a real fluid, the cascade blade elements situated near the tunnel walls show losses of greater magnitude than those associated with blade elements in the central part of the blade height. The "end" losses were permitted to develop to their full extent in the present investigation by omitting fillets or fairing pieces at the junction of blade and tunnel wall. A comprehensive discussion of factors contributing to blade-end losses was given by *Meldahl* [44], who recognized the similar, yet distinctly independent, nature of "end" and "tip-clearance" losses in cascades. More recently *Weske* [45] has given a qualitative discussion of end effect in terms of boundary-layer shifts for flow through both stationary and rotating cascades.

From the three-dimensional momentum-equation traverses carried out as described in (V. C. 3), the distribution of losses over the blade height, as indicated by the quantity $\left(\frac{P_{g1} - P_{g2}}{P_{g1}}\right)$, was plotted as shown in Figure 40.

(Compare with the much higher end losses of a *retarding* cascade in the excellent presentation by *Howell*, reference 46.) Figure 40 indicates that normal flow conditions prevailed over a preponderant part of the blade length. Notice slightly greater losses of the upper end relative to the lower end due to tip clearance required for weighing forces on the reference blade (III. B, C.).

The provision of a small (0.15 mm) clearance at the upper end of the reference blade superimposed a tip-clearance loss upon the normal "end" loss, and constituted a departure from absolute geometrical uniformity of all blades and from vertical symmetry of the reference blade. To gain a more direct indication of the effect of this departure than shown in Figure 40, the static pressure field about the blade tip was mapped, from measurements described in (V. C. 1), for clearance space open and closed. Figure 41 compares the two fields. Comparison of Figure 41 with Figure 34 indicates that the disturbance of the static pressure field due to tip clearance alone is small relative to the difference between static pressure distributions at center and end of blade, or "end effect".

Several further interesting evidences of end losses were obtained. The measured angle of turn of the air was 2—3° *greater* in the zone within 5 mm of the blade ends than over the rest of the blade height, thus partially confirming *Meldahl's* hypothesis. The blade-surface-flow conditions pictured

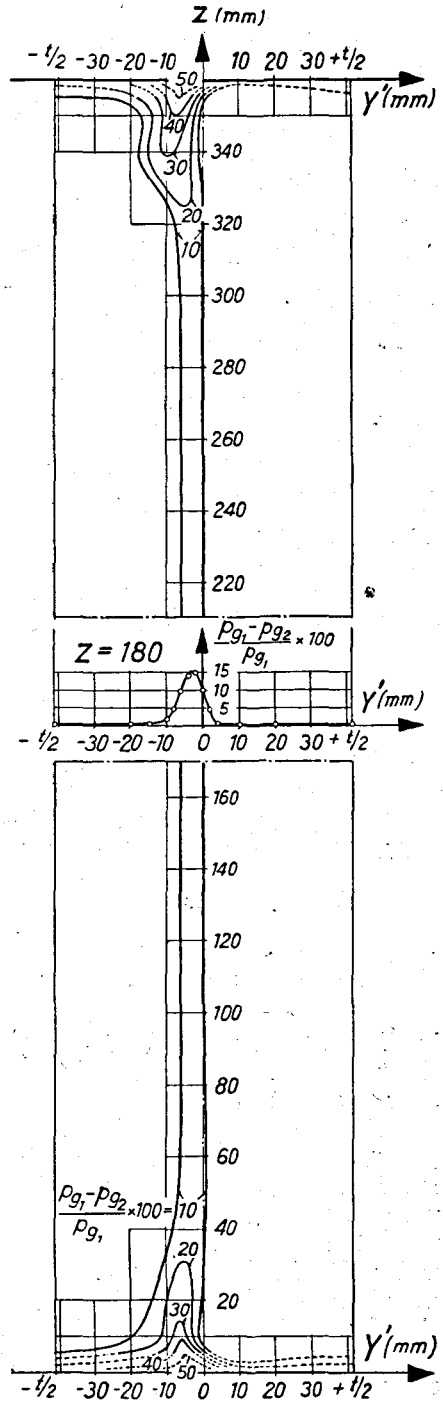


Figure 40: Distribution of Blade Losses over Blade Length. Planes (1) and (2) are $x(x') = 100$ mm

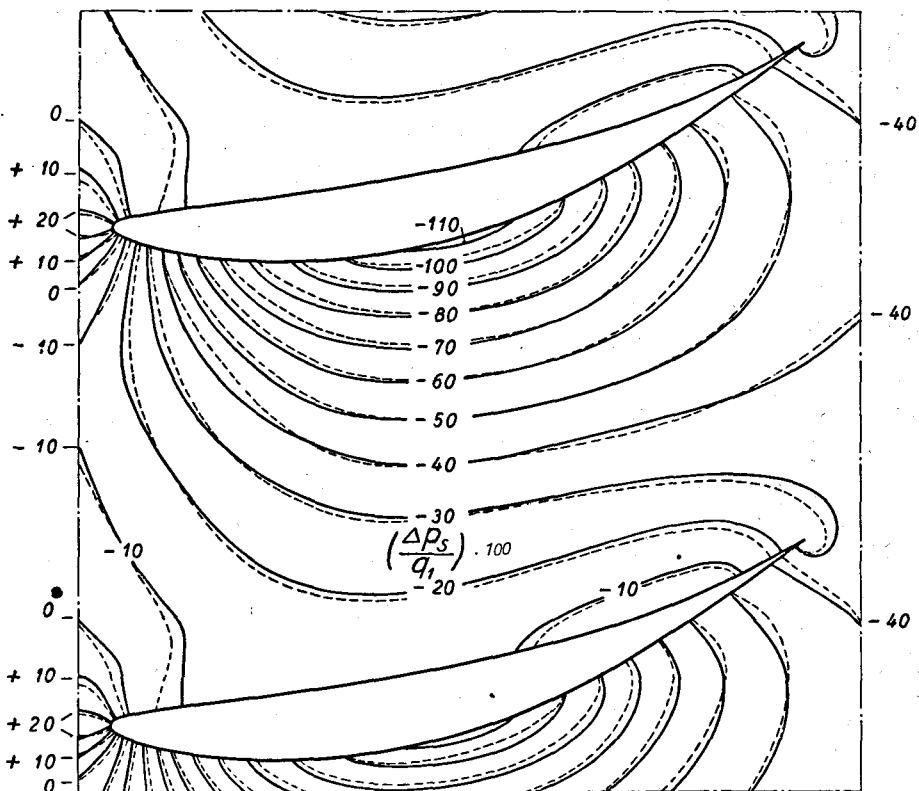


Figure 41:
Disturbance of Static Pressure Field at Blade Upper End Due to Tip Clearance

Curves are Contours of Constant $\left(\frac{P_s - P_{s1}}{q_1}\right) \cdot 100$.

— Zero Tip Clearance
 ---- 0.15 mm Tip Clearance

$q_1 = 40.4 \text{ mm H}_2\text{O}; \frac{\sqrt{u^2}}{u} = 1 \%$.

in Figure 38 clearly show the growth of wall boundary layer thickness through the cascade and the formation of a vortex leaving the trailing edge near its point of junction with the upper wall. Of the two blades shown in this figure, the right-hand one has no tip clearance, while the left-hand (reference) blade has a small clearance as a result of which both boundary-layer growth and evidence of vortex formation are more pronounced. The vertical static-pressure traverses taken downstream from the cascade give further evidence of the detached vortex formed at junction between blade and wall. Most conclusive evidence of the relatively higher blade losses near the tunnel walls was obtained during the evaluation of the three-dimensional momentum-equation measurements (V. C. 3). The plotted curve of tangential force per unit length as a function of z (not given) was practically constant over the central part of the blade height, but began to fall sharply toward zero at a distance of approximately 20 mm from the blade

ends. The plotted curve of normal force per unit length was also constant over the central section, but increased to about double the central-zone value at a distance of approximately 10 mm from the blade ends. The higher blade-element losses at the blade ends are thereby apparent.

2. Blade Efficiency from Force Measurements

a) Definition and Derivation of Blade Efficiency Using Blade Forces

The definition and evaluation of a true "blade efficiency" from the results of cascade tests requires the introduction of an imaginary translatory motion. The introduction of such a motion of the cascade parallel to its axis, with the added requirement that the entrance velocity relative to the

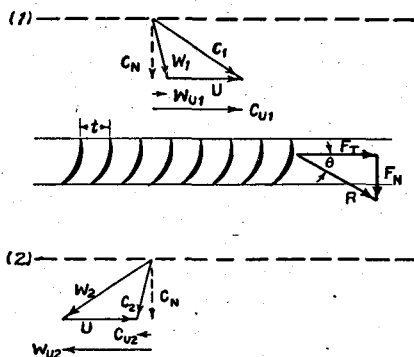


Figure 42: Diagram for Definition of Cascade Velocity and Force Components
Plane (2) is Plane of Uniform Flow Far Downstream. Positive Direction For Tangential Velocities and F_T Is That Opposite to W_{u2} . F_N Is Positive In Direction of C_N

cascade shall remain the same as the actual entrance velocity used in testing, leads to a fictitious absolute entrance velocity C_1 having the same axial component as the entrance velocity at test (see Figure 42). Considering first an accelerated-flow cascade, we may then define the blade efficiency as:

$$\eta = \frac{\text{Power Output}}{\text{Rate of Energy Input}} = \frac{F_T \cdot U}{\iint_{(A)} C_{n1} (P_1 - P_2) dA + \iint_{(A)} C_{n1} \cdot \frac{\rho}{2} \cdot C_{u1}^2 \cdot dA} \quad (1)$$

where: $A = Z \cdot t$

Z = Tunnel height; t = Blade spacing

U = Velocity of the cascade in direction of its axis.

The following assumptions are made:

1. The tangential component of the absolute velocity at plane (2) is considered as a loss.

2. The available potential (pressure) energy given up by the fluid between planes (1) and (2) may be computed on the assumption of incompressibility.

3. The excess of axial memomentum present immediately behind the cascade due to the local non-uniformity of flow has disappeared at plane (2), and the total axial momentum at plane (2) is equal to that at plane (1).

4. The top and bottom walls of the tunnel are parallel and exert no shearing force upon the fluid between planes (1) and (2).

The first integral of equation (1) may be written as the product of two integrals, assuming small variations of C_{n1} over A ;

$$\iint C_{n1}(P_1 - P_2) dA \approx \iint C_{n1} \cdot dA \times \frac{1}{A} \iint (P_1 - P_2) \cdot dA \quad (2)$$

where: $\iint C_{n1} \cdot dA = Q =$ volume rate of flow and, under assumptions (3) and (4);

$$\frac{1}{A} \iint (P_1 - P_2) dA = \frac{F_N}{A} = \frac{\text{Normal component of blade force}}{\text{unit flow area}}.$$

The second integral in (1) may be resolved in terms of its components; since

$$C_{u1}^2 = W_{u1}^2 + 2 W_{u1} \cdot U + U^2,$$

$$\iint C_{n1} \cdot \varrho/2 \cdot C_{u1}^2 \cdot dA = \iint C_{n1} \cdot \varrho/2 \cdot W_{u1}^2 \cdot dA + \iint C_{n1} \cdot \varrho W_{u1} \cdot U \cdot dA + \iint C_{n1} \cdot \varrho/2 \cdot U^2 \cdot dA \quad (3)$$

Equation (1) may now be written:

$$\eta = \frac{F_T \cdot U}{Q \cdot \frac{F_N}{A} + \iint C_{n1} \cdot \varrho/2 \cdot W_{u1}^2 \cdot dA + \iint C_{n1} \cdot \varrho \cdot W_{u1} \cdot U \cdot dA + \iint C_{n1} \cdot \varrho/2 \cdot U^2 \cdot dA} \quad (4)$$

We now define U by the requirement of maximum efficiency:

$$\left(\frac{\partial \eta}{\partial U} \right)_{U=U_{optimum}} = 0 \quad (5)$$

For $W_{u1} = \text{constant}$, $U_{optimum}$ is then found, by partial differentiation of (4), to be

$$U_{op} = \sqrt{\frac{F_N}{\varrho/2 \cdot A} + W_{u1}^2}. \quad (6)$$

With $\varrho Q = M$ (mass rate of flow), the maximum efficiency becomes:

$$\eta_{max} = \frac{F_T/M}{U_{op} + W_{u1}}. \quad (7)$$

We note that, for an *ideal* cascade,

$$P_1 + \varrho/2 \cdot W_{u1}^2 = P_2 + \varrho/2 \cdot W_{u2}^2;$$

$$W_{u2} = \sqrt{\frac{P_1 - P_2}{\varrho/2} + W_u^2}$$

and since $(P_1 - P_2) = \frac{F_N}{A}$, we may write

$$W_{u2_{ideal}} = \sqrt{\frac{F_N}{\rho/2 \cdot A} + W_{u1}^2}.$$

This leads to the very interesting conclusion that

$$\underline{U_{op} = -W_{u2_{ideal}}}. \quad (8)$$

(The negative sign follows from original convention, Figure 42.)

Defining

$$W_{u1} - W_{u2_{id.}} \equiv (\Delta W_u)_{id.},$$

and further noting that

$$\Delta W_u = \frac{F_T}{M},$$

the definition of maximum efficiency may be written in its most general form for uniform flow at (1):

$$\underline{\eta_{max} = \frac{\Delta W_u}{(\Delta W_u)_{id.}}} \quad \dots\dots \text{Turbine} \quad (9)$$

For all cases in which (9) fails [i. e.; $(\Delta W_u)_{id.} < \Delta W_u$], the operating condition is, in accordance with the definition of positive U in Figure 42, that of compressor operation, for which the maximum efficiency may analogously be shown to be;

$$\underline{\eta_{max} = \frac{(\Delta W_u)_{id.}}{\Delta W_u}} \quad \dots \text{Compressor} \quad (10)$$

Evaluation of (9) or (10) requires only the quantities readily measurable in cascade tests, namely F_T and F_N (or R and Θ); the distribution of vector velocity of approach, W_1 ; and the density ρ since;

$$\Delta W_u = \frac{F_T}{M}$$

$$M = \rho \iint_{(A)} C_{n1} \cdot dA \equiv \rho \cdot \bar{C}_{n1} \cdot A \cdot \frac{Z - \delta^*}{Z}$$

$\bar{C}_{n1} = \bar{W}_{n1}$ = axial component of uniform incident flow outside the tunnel wall boundary layers;

Z = Tunnel height

t = Blade spacing

$A = Z \cdot t$

δ^* = total contraction thickness $= 2 \int_0^{\delta} \left(1 - \frac{C_{n1}}{\bar{C}_{n1}}\right) dz$

$$(\Delta W_u)_{id.} \equiv W_{u1} - W_{u2_{id.}} = W_{u1} + \sqrt{\frac{F_N}{\rho/2 \cdot A} + W_{u1}^2}.$$

For the cascade tested in this investigation, $W_{u1} = 0$, and the equation for maximum efficiency (7) simplifies to:

$$\eta_{max} = \frac{F_T}{M} \sqrt{\frac{q/2 \cdot A}{F_N}} = \frac{1}{2} \sqrt{\cos \Theta \cdot \cotan \Theta \cdot \frac{R}{q_1 \cdot A} \cdot \frac{Z}{Z - \delta^*}} \quad (11)$$

It should be specifically noted that, under the assumptions from which this definition of maximum efficiency was derived, the absolute velocity behind the cascade is not in general axial; a tangential component remains which is reckoned as lost. The efficiency resulting from the assumption ($C_{u2} = 0$) is very nearly equal to the maximum efficiency, the differences being as shown below:

$\eta_{max} :$	100	95	90	80
$\eta_{(C_{u2}=0)} :$	100	94.9	89.5	77.8

b) Evaluation of the Blade Efficiency from Current Tests

The method used in carrying out balance measurements was given in (V. C. 2). For various conditions of turbulence, the resultant blade force, R , and its angle relative to the cascade axis, Θ , are given in Figure 43. Figure 44 gives the respective force components in the direction of the cascade axis, F_T , and normal to the cascade axis, F_N . The quantity A_b in the dimensionless expression for forces and force components is the blade projected area ($= 0.0432 \text{ m}^2$), while q_1 is the mean inlet dynamic pressure. By means of measurements over the reference inlet plane, ($x = 100$), the relation between the mean inlet dynamic pressure q_1 , and the *reference* inlet dynamic pressure q'_1 , which was used during the weighing (V. C. 2), was determined for the full range of Re and for each of the three main turbulence conditions. In the case of 3.4 % turbulence, q_1 contains a turbulence correction amounting to $-0.005 \cdot q'_1$. The results of the evaluation of the three-dimensional momentum-equation measurements (V. C. 3) are given in Figure 43 for comparison with the measured 1 %-turbulence curve.

Overall blade efficiencies are given in Figure 45. Efficiencies were calculated from foregoing equation (11) and data of Figure 43; the total contraction thickness was given by $\frac{\delta^*}{Z} = 0.005$. Values shown in Figure 45 may be interpreted as accurate within $\frac{2}{10} \%$.

The efficiency curves serve as the ultimate bases for appreciation of Reynolds number and turbulence effects in practical cases. At *high Reynolds numbers*, the blade performs *less* efficiently for the conditions of *increased turbulence* (either general or local, produced by upstream turbulence screens or local bands, respectively) than for the condition of normal (low) turbulence. This is due to the transition of the boundary layer to turbulence at a point closer to the leading edge for the former cases (VI. A. 2). At *low Reynolds numbers*, however, the blade performs *more* efficiently when the turbulence is increased, especially by bands (case of local high turbulence).

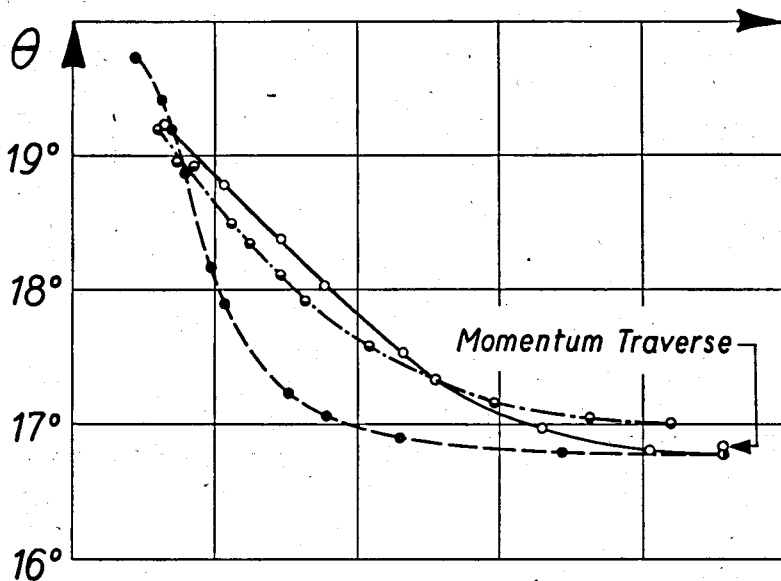
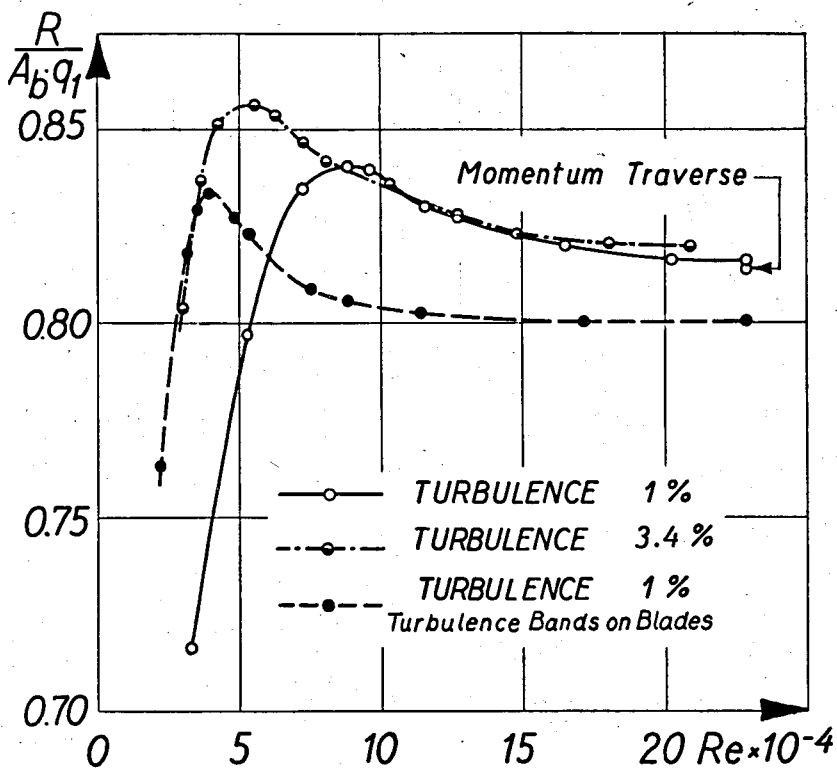


Figure 43: Magnitude and Direction of Resultant Blade Force
 R ; θ Defined in Fig. 42. A_b = Blade Projected Area (Upon Chord). q_1 = Mean Inlet Dynamic Pressure

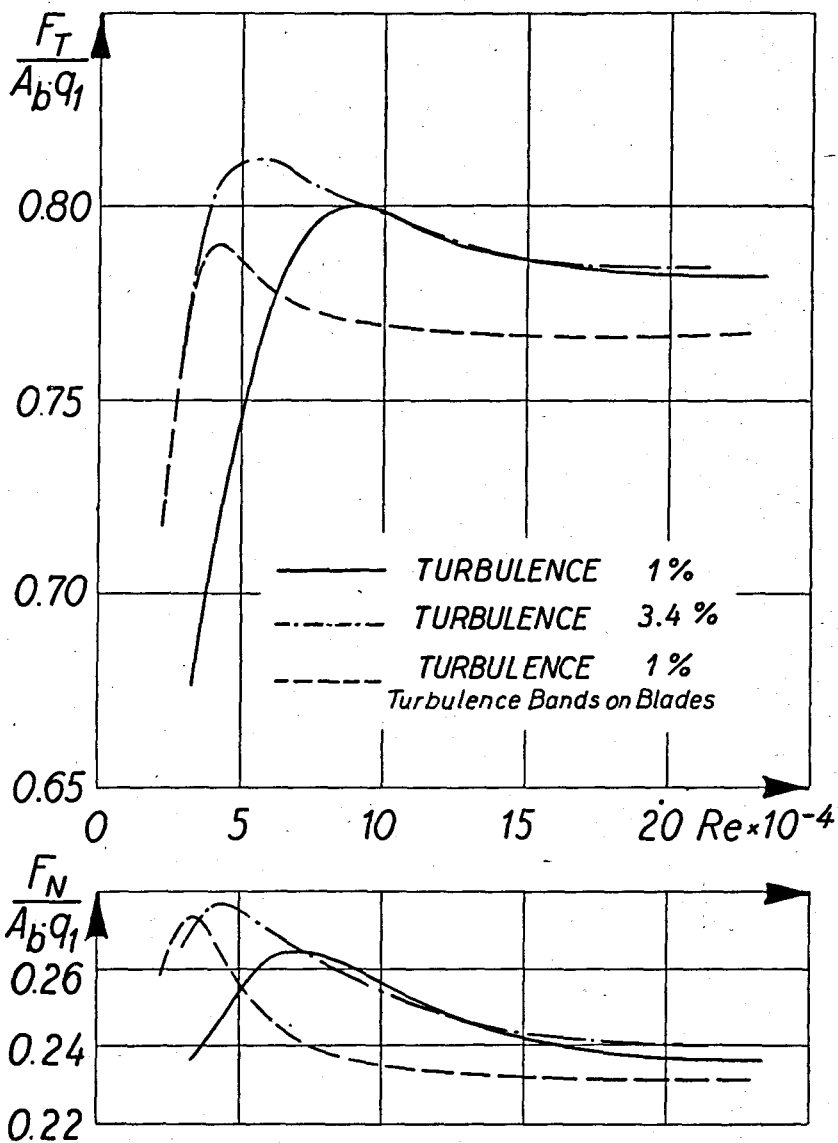


Figure 44: Blade Force Components

F_T ; F_N Defined in Fig. 42. A_b = Blade Projected Area (Upon Chord). q_1 = Mean Inlet Dynamic Pressure

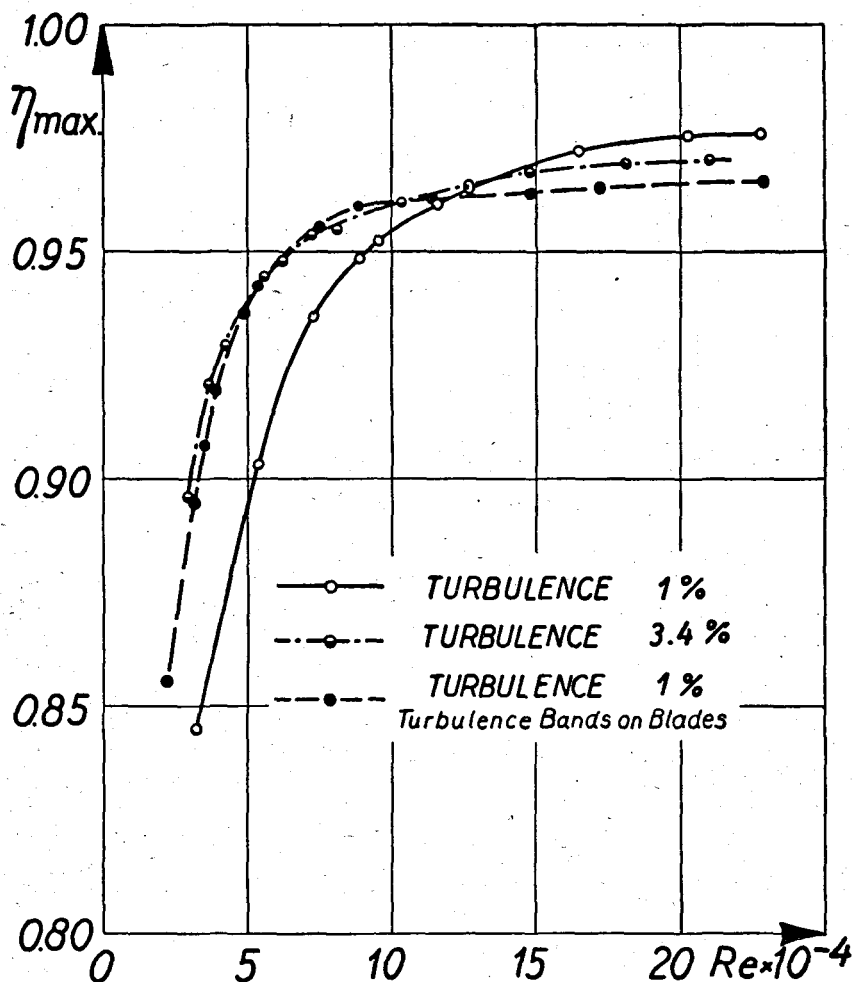


Figure 45: Computed Maximum Blade Efficiencies (Cascade) from Force Measurements

In this case, separation is the governing factor. It may be concluded generally that the blade profile tested performs most efficiently, for *high* Reynolds numbers, under conditions of minimum stream turbulence; while for *low* Reynolds numbers, increased stream turbulence leads to better efficiencies. The general increase in efficiency with increasing Reynolds number is apparent for all conditions of turbulence, being most pronounced for the least turbulent condition.

VII. Summary and Conclusions

A. Cascade Testing in General

The practicability of direct measurement of cascade blade forces by use of a suitably accurate balance was demonstrated. A valid and practical "blade efficiency" for a cascade in terms of force components was defined and used to reflect the practical influences of flow variables. Various means of observation of boundary layer separation and transition were discussed and their indications shown to be consistent among one another. Accuracy of measurement of flow conditions was substantiated by means of the continuity equation applied to three-dimensional observations.

B. Turbulence and Reynolds-Number Effects Upon Blade Performance

The existence of a minimum Reynolds number, below which the cascade may not be satisfactorily operated, has been recognized. This limit is more pronounced when it is identified with the lift breakdown. It is less distinct and occurs at somewhat higher Reynolds numbers, if defined in terms of losses. This critical minimum Reynolds number decreases with increase in turbulence intensity of the incident flow. Creation of high local turbulence intensity on the blade suction side by physical surface irregularities serves to decrease the critical Reynolds number in the same manner as increasing general stream turbulence. Within certain limits, the separate influences of turbulence *intensity* and of turbulence *scale* were investigated, yielding the conclusion that the effect of intensity far outweighed that of scale. In fact, for the restricted limits between which it was possible to vary the scale of turbulence, no definite influence of this parameter could be established, due probably to the "laminar" nature of the blade profile.

C. Continuum Theory of Cascades

The *Ackeret* theory for the prediction of flow through a two-dimensional cascade of closely-spaced airfoils of finite thickness has been shown to yield a satisfactory approximation to the experimental conditions for a single cascade arrangement tested. The theory produced a blade form which, in cascade, yielded a tangential force (work) component within 1.5 % of the theoretical (*Euler* equation) component, and a pressure drop within 3 % of the theoretical. Also of practical interest to the designing engineer, the cascade constructed according to the theory produced, with better than 97 % maximum efficiency, an actual mean angle of turn of the air flow within 1.7 % of the turning angle desired (desired turning angle = 30° ; actual mean turning angle = $29^\circ.5$). Using supplementary curves presented herein, a complete solution by the theory, giving the resultant blade profile and associated pressure distribution, may be obtained in approximately 40 hours.

References

1. *Ackeret, J.*, "Zum Entwurf dichtstehender Schaufelgitter"; Schweiz. Bauzeitung, Bd. 120, Nr. 9, August 1942.
2. *Lorenz, H.*, "Neue Theorie und Berechnung der Kreiselräder". München, 1906.
3. *Bogdonoff, S. M.*, "N.A.C.A. Cascade Data for the Blade Design of High-Performance Axial-Flow Compressors"; Jour. of Aero. Sciences, V. 15, No. 2, Feb. 1948, pg. 89.
4. *Betz, A.*, "Diagramme zur Berechnung von Flügelreihen"; Ingenieur-Archiv, II. Band, 1931, S. 359.
5. *Schilhansl, M.*, "Näherungsweise Berechnung von Auftrieb und Druckverteilung in Flügelgittern"; Jahrbuch der Wissenschaftl. Gesellschaft für Luftfahrt, 1927, S. 151.
6. *Weinel, E.*, "Beiträge zur rationalen Hydrodynamik der Gitterströmung"; Ingenieur-Archiv, V. Band, 1934, S. 91.
7. *Weinig, F.*, "Die Strömung um die Schaufeln von Turbomaschinen"; Leipzig, 1935.
8. *König, E.*, "Potentialströmung durch Gitter"; Z. A. M. M. 2. 1922, S. 422.
9. *Busemann, A.*, "Das Förderverhältnis radialer Kreiselpumpen mit logarithmisch-spiraligen Schaufeln"; Z. A. M. M. 8, 1928, S. 372.
10. *Howell, R. A.*, "Note on the Theory of Arbitrary Airfoils in Cascade"; R.A.E. Note No. E 3859, March 1941.
11. *Traupel, W.*, "Die Berechnung der Potentialströmung durch Schaufelgitter"; Schweizer Archiv, Heft 12, 10. Jahrgang, 1944.
12. *Vazsonyi, A.*, "On the Aerodynamic Design of Axial-Flow Compressors and Turbines"; Jour. of Appl. Mechanics, March 1948, pg. 53.
13. *Legendre R.*, "Tracé des Ailettes pour Fluides à Densité Légèrement Variables"; Lecture presented to l'Association Technique Maritime et Aéronautique, Paris, 1947.
14. *Weinig, F.*, Widerstands- und Tragflügelprofile mit vorgeschriebener Geschwindigkeitsverteilung an der Oberfläche"; Z. angew. Math. Mech., Bd. 9, 1929, S. 507.
15. *Schmieden, C.*, "Die Berechnung kaviationsssicherer Tragflügelprofile"; Z. angew. Math. Mesch., Bd. 12, 1932, S. 288.
16. *Betz, A.*, "Änderung der Profilform zur Erzielung einer gegebenen Änderung der Druckverteilung"; Luftfahrtforschung, Bd. 11, 1934, S. 1.
17. *Peebles, G. H.*, "A method for Calculating Airfoil Sections from Specifications on the Pressure Distributions"; Jour. Aero. Sciences, Vol. 14, No. 8, August 1947, pg. 451.
18. *Mangler, E.*, "Die Berechnung eines Tragflügelprofiles mit vorgeschriebener Druckverteilung"; Jahrbuch d. deutschen Luftfahrtforschung, 1938, S. 1—46.
19. *Meyer, R.*, "Beitrag zur Theorie feststehender Schaufelgitter"; Mitt. Nr. 11; Inst. für Aero., E. T. H. Zürich, 1946.
20. *Keller, C.*, "Axialgebläse vom Standpunkt der Tragflügeltheorie"; Mitt. Nr. 2; Inst. für Aero., E. T. H., Zürich 1934.
21. *Wislicenus, G. F.*, "Fluid Mechanics of Turbo-Machinery"; New York (McGraw-Hill), 1947.
22. *Pierce, B. O.*, "A Short Table of Integrals"; Boston (Ginn and Co.), 3rd Edition, 1929.
23. *Mühlemann, E.*, "Experimentelle Untersuchung an einer axialen Gebläsestufe"; Mitt. Nr. 12; Inst. für Aero., E. T. H., Zürich, 1946, S. 15.
24. *Ackeret, J.*, "Das Institut für Aerodynamik an der E. T. H."; Mitt. Nr. 8; Inst. für Aero., E. T. H., Zürich, 1943, S. 18.

25. Klein, G., "Untersuchung und Kritik von Hochdruckmessern"; Zeitschrift d. V. d. Ing., 1909.
26. Michels, A., "Einfluss der Rotation auf die Empfindlichkeit einer absoluten Druckwaage"; Annalen der Physik (4), Leipzig 1923, S. 285.
27. Dryden, H. L., Schubauer, G. B., Mock, W. C., and Skramstad, H. K., "Measurements of Intensity and Scale of Wind Tunnel Turbulence and Their Relation to the Critical Reynolds Number of Spheres"; N. A. C. A. Report No. 581, 1937.
28. Dryden, H. L., "A Review of the Statistical Theory of Turbulence"; Quarterly of Applied Mathematics, Vol. 1, No. 1, April 1943.
29. Taylor, G. I., "Statistical Theory of Turbulence"; Proc. Royal Society of London (A), Vol. 151, 1935.
30. — "Statistical Theory of Turbulence; Part V"; Proc. Royal Society of London (A), Vol. 156, No. 888, pg. 307, August 1936.
31. Prandtl, L., "Der Luftwiderstand der Kugeln"; Nachr. d. K. Ges. d. Wissensch., Göttingen; Math. Phys. Kl., 1914, S. 177.
32. Dryden, H. L. and Kueth, A. M., "Effect of Turbulence in Wind Tunnel Measurements", N. A. C. A. No. 342, 1930.
33. N. A. C. A. 20th Annual Report, 1934, pg. 16 and 23.
34. Dryden, H. L., "Frontiers of Aerodynamics"; Jour. Wash. Acad. Sci., Vol. 25, March 1935; pg. 101.
35. Hoerner, S., "Tests of Spheres with Reference to Reynolds No., Turbulence, and Surface Roughness"; T. M. No. 777, N. A. C. A., 1935.
36. Platt, R. C., "Turbulence Factors of N. A. C. A. Wind Tunnels as Determined by Sphere Tests"; N. A. C. A. Report No. 558, 1936.
37. Pfenniger, W., "Vergleich der Impulsmethode mit der Wägung bei Profilwiderstandsmessungen"; Mitt. Nr. 8; Inst. für Aero., E. T. H. Zürich, 1943, S. 66.
38. Schubauer, G. B., "Air Flow in the Boundary Layer of an Elliptic Cylinder"; N. A. C. A. Report No. 652, 1939.
39. Schlichting, H., "Zur Entstehung der Turbulenz bei Plattenströmung"; Nach. Gesell. d. Wiss. Z. Göttingen, M. P. K., 1933.
40. Schubauer, G. B. and Skramstad, H. K., "Laminar Boundary-Layer Oscillations and Stability of Laminar Flow"; Jour. of Aero. Sciences, Vol. 14, No. 2, February 1947.
41. Dryden, H. L., "Air Flow in the Boundary Layer Near a Plate"; N. A. C. A. Report No. 562, 1936.
42. Jacobs and Dönhoff, "Transition As It Occurs Associated With and Following Laminar Separation"; Proc. 5th Int. Congress for Appl. Mech., Cambridge, Mass., 1938.
43. Pfenniger, W., "Untersuchungen über Reibungsverminderungen an Tragflügeln"; Mitt. No. 13, Inst. für Aero., E. T. H. Zürich, 1946.
44. Meldahl, A., "Über die Endverluste der Turbinenschaufeln"; Brown Boveri Mitteilung, Nov. 1941, S. 356.
45. Weske, J. R., "Fluid Dynamic Aspects of Axial-flow Compressors and Turbines"; Jour. Aero. Sci., Vol. 14, No. 11, Nov. 1947; pg. 651.
46. Howell, A. R., "Fluid Dynamics of Axial Compressors"; Proc. Inst. of Mech. Engineers, London, Vol. 153, 1945, pg. 448.

Autobiographical Outline

I am a citizen of the United States of America, and was born in Nantucket, Mass., U.S.A. on April 13, 1918. I completed eight grades of primary school education in Gardner, Mass. in 1930, followed by four years of high school in the same city. One year of college preparatory study was completed at Severn School, Severna Park, Maryland, in 1935, in which year I entered the United States Naval Academy at Annapolis. Upon completion of the Naval Academy curriculum in 1939, I was commissioned an officer in the United States Navy. After three years of service at sea, I entered the Massachusetts Institute of Technology, Cambridge, Mass., and received the graduate degree of Master of Science in Naval Architecture and Marine Engineering in late 1944. Following one and one-half years of practical work in the repair of vessels at a naval shipyard, I was accepted as a co-worker in the Institute for Aerodynamics, Swiss Federal Institute of Technology, in April, 1946. In this capacity I carried out independent research upon a stationary cascade terminating with the submission of a dissertation on July 16, 1948.